UNIVERSIDAD CARLOS III DE MADRID
Escuela Politécnica Superior
Departamento de Ingeniería Térmica y de Fluidos

"PARTICLE-FLUID DYNAMICS AND SOLID EJECTION IN FLUIDIZED BEDS"

Tesis Doctoral

Autor:
José Antonio Almendros Ibáñez
Ingeniero Industrial

Director de Tesis:
Domingo Santana Santana
Licenciado en Matemáticas
Doctor en Ingeniería Industrial

Leganés (Madrid), a 25 de Abril de 2008

Tesis Doctoral

"PARTICLE-FLUID DYNAMICS AND SOLID EJECTION IN FLUIDIZED BEDS"

Autor: José Antonio Almendros Ibáñez
Director de Tesis: Domingo Santana Santana

El tribunal, nombrado por el Magfco. y Excmo. Sr. Rector de la Universidad Carlos III de Madrid,

Presidente D. Bo Leckner, Chalmers University of Technology

Vocal D. Andrés Cabanillas Cabanillas, CIEMAT

Vocal D. Francisco Vicente Tinaut Fluixá, Universidad de Valladolid

Vocal D. Magín Lapuerta Amigo, Universidad de Castilla La Mancha

Secretario D. Alberto Gómez Barea, Universidad de Sevilla

Suplente D. Javier Rodríguez Rodríguez, Universidad Carlos III de Madrid

Suplente D. Ulpiano Ruiz-Rivas Hernando, Universidad Carlos III de Madrid

acuerda la calificación de: _____

El presidente El secretario

Los vocales

En Leganés (Madrid), a 25 de Abril de 2008

The arrival time of a space probe travelling to Saturn can be predicted more accurately than the behaviour of a fluidized bed chemical reactor!.

D. Geldart (1986)

Always start by trying the simplest model and then only add complexity to the extent needed.

O. Levenspiel (2002)

Rasgo dominante en los investigadores eminentes es la altiva independencia de criterio. Ante la obra de sus predecesores y maestros no permanecen suspensos y anonadados, sino recelosos y escudriñadores. Copérnico, Kepler, Newton y Huyghens echaron abajo la astronomía de los antiguos, fueron sin duda preclaros entendimientos pero, ante todo, poseyeron individualidad mental ambiciosa y descontentadiza y osadía crítica extraordinaria. [...]
La admiración excesiva achica la personalidad y ofusca el entendimiento, que llega a tomar las hipótesis por demostraciones, las sombras por claridades.

S. Ramón y Cajal (1902)

Contents

List of Figures

List of Tables

Agradecimientos

En primer lugar quiero agradecer a mi familia: mis padres y mi hermana su apoyo en todos los caminos que he tomado desde mi época de estudiante hasta hoy. También quiero agradecer a Rocío su cariño, paciencia y compañía durante todos estos años juntos. Sin ellos todo habría sido más difícil.

Gracias a mi director de tesis, Domingo Santana por su sinceridad desde el primer día y ayuda constante durante todos estos años. También quiero agradecer al resto de doctores del grupo ISE: Mercedes, Ulpiano, Antonio Acosta y Nestor su compañerismo y ayuda siempre que la he necesitado.

También quisiera dar las gracias a todos los becarios y ayudantes, que durante estos años han pasado por el Departamento de Ingeniería Térmica y de Fluidos por todos los cafés, comidas y buenos ratos que hemos pasado juntos. En especial a los integrantes del grupo ISE: Sergio y Antonio Soria, con los que he trabajado más estrechamente y Celia, también compañera de despacho y de viajes. No quiero olvidarme de mi otro compañero de despacho, Rafa. Ha sido un placer compartir despacho con ellos estos cuatro años.

También quisiera dar las gracias a Alberto, amigo y compañero de piso durante muchos años y a Gabriel, amigo, compañero de piso y de carrera y con el que di mis primeros pasos en el mundo de la investigación.

Gracias al grupo de Mecánica de Fluidos, por haber compartido amable y desinteresadamente su cámara de alta velocidad siempre que la he necesitado, sin la cual esta tesis no habría sido posible.

Por último, quisiera dar las gracias al Prof. Filip Johnsson y a David Pallarès, de la Universidad de Chalmers (Göteborg, Suecia), con los que realize una estancia de tres meses durante el verano de 2006. Muchas de las ideas de esta tesis nacieron durante dicha estancia. Sus comentarios y ayuda durante años posteriores han ayudado a mejorar notablemente los resultados finales de esta tesis.

Resumen

Los flujos multifásicos son, en general, difíciles de modelar. En concreto, los lechos fluidizados burbujeantes son incluso más complejos debido a la presencia de burbujas (aparte de las partículas y de la corriente principal del gas) que aparecen cuando las perturbaciones no son atenuadas por el sistema. Esta tesis doctoral intenta aclarar algunos aspectos relacionados con la dinámica fluido-partícula y con la proyección de sólidos en lechos fluidizados mediante resultados experimentales y simulaciones numéricas. Los experimentos fueron llevados a cabo en un lecho fluidizado bidimensional usando PIV (Velocimetría por Imágenes de Partículas) y técnicas de análisis de imágenes digitales. Algunos de los resultados experimentales fueron usados como datos de entrada en el análisis numérico mediante FEM (Método de los Elementos Finitos).

Este documento contiene una introducción general (capítulo 1), un capítulo de conclusiones (capítulo 7) y cinco capítulos diferentes e independientes (del capítulo 2 al 6). Cada uno de ellos tiene su propio resumen, introducción, notación y bibliografía. Cada capítulo puede ser leído independientemente ya que han sido escritos como artículos independientes.

El capítulo 2 presenta un novedoso método numérico-experimental que combina PIV y FEM para caracterizar la dinámica de los lechos fluidizados. En un lecho burbujeante, la geometría de las burbujas fue capturada con una cámara de alta velocidad, y el campo de velocidades de las partículas (velocidad del gránulo) se obtuvo aplicando PIV a la fase densa. La geometría de las burbujas se exportó a un programa de elementos finitos, donde aplicando las ecuaciones propuestas por Davidson (Davidson J.F., 1961. Symposium on fluidisation-Discussion. *Transactions of the Institution of Chemical Engineers*, vol. 29, pp. 230-232) el campo de velocidades del gas y el campo de presiones se calcularon con un bajo coste computacional. Diferentes tipos de burbujas fueron estudiadas: lentas, rápidas, rompiendo la superficie libre y coalesciendo. Además, se ha analizado el efecto de la no verticalidad de las burbuja rápidas, mostrando como estas burbujas pueden intercambiar gas con la corriente principal.

En el capítulo 3, el método explicado en el capítulo 2 se ha extendido para tener en cuenta los efectos inerciales. La ley de Darcy propuesta por el modelo de Davidson

se reemplazó por la ecuación de Ergun, que tiene en cuenta ambos efectos: viscosos e inerciales. Los mismos casos estudiados en el capítulo 3 fueron analizados incluyendo los efectos inerciales. Los resultados obtenidos muestran como estos efectos son más importantes cuando la velocidad local del gas, y en consecuencia el número de Reynolds, aumentan. En cualquier caso, estas diferencias locales no afectan apreciablemente las líneas de corriente del gas para las condiciones experimentales de este trabajo.

El capítulo 4 presenta una nueva metodología para obtener la distribución de la porosidad alrededor de las burbujas. La instalación experimental utilizada consiste en un cámara de alta velocidad, un lecho fluidizado bidimensional y una fuente de luz difusa situada en la parte trasera del lecho. De los resultados experimentales obtenidos, se ha propuesto una nueva correlación para la distribución de la porosidad alrededor de las burbujas. Esta correlación difiere de las existentes en la literatura en dos aspectos. Primero, ha sido obtenida en una región adyacente al contorno de la burbuja ($r/R_b \lesssim 1.2$), donde la baja resolución espacial de otros estudios impidió obtener resultados. En segundo lugar, no se ha supuesto simetría radial, la porosidad depende de las posiciones radial y angular $\epsilon = \epsilon(\theta, r)$. Además, se ha estudiado el efecto de la distribución de porosidad en el flujo de aire que atraviesa la burbuja, obteniendo un aumento del 20% para la geometría media de las más de 100 burbujas analizadas.

El capítulo 5 presenta los resultados de un estudio experimental sobre la velocidad de proyección de sólidos en lechos fluidizados con gas. Los mecanismos observados previamente por Levy et al. (Levy E.K., Caram H.S., Dille J.C. and Edelstein S., 1983. Mechanims for solid ejection from gas-fluidized beds, *AIChE Journal*, vol. 29, pp. 383-388) han sido estudiados. Los resultados muestran como un grupo de partículas cayendo en forma de estalactitas dentro de la burbuja reduce notablemente la velocidad de la cúpula en burbujas aisladas. Las velocidades más grandes aparecen cuando hay coalescencia, especialmente en el mecanismo de proyección desde la estela. En el mecanismo de proyección en forma de canal o de chorro, los choques entre partículas reducen notablemente la velocidad de proyección.

El capítulo 6 presenta un nuevo modelo para obtener el perfil de velocidad de las partículas proyectadas en burbujas que rompen aisladas. Este sencillo modelo es también válido para burbujas que no ascienden verticalmente. El modelo supone que la velocidad de proyección depende de la velocidad de la burbuja y de su velocidad de crecimiento. Los resultados experimentales muestran que, excepto en algunos casos aislados, el modelo predice correctamente la magnitud y dirección de la velocidad máxima y el perfil de velocidades

Abstract

Multiphase flows are often difficult to model. In particular, freely bubbling fluidized beds are even more complex due to the presence of gas pockets or bubbles, together with particles and the gas main stream. Their appearance is related to perturbations that are not attenuated by the system. This PhD thesis try to shed some light, through experiments and numerical simulations, on the particle-fluid dynamics in fluidized beds and on the phenomenon of solid ejection. The experiments were carried out in a cold 2-D fluidized bed using PIV (Particle Image Velocimetry) and digital image analysis techniques. Some of the experimental results were used as input data in the FEM (Finite Element Method) numerical analyses.

This document contains a general introduction (chapter 1), a chapter of conclusions (chapter 7) and five different and independent chapters (from chapter 2 to 6). These five chapters has its own abstract, introduction, notation and bibliography. Each can be red independently of the others because they have been written as independent articles.

Chapter 2 presents a novel experimental-numerical method that combines PIV and FEM to characterize the dynamics of fluidized beds. On a freely bubbling fluidized bed, the bubbles geometry was captured using a high speed video-camera, and the particle velocity field (granular velocity) was obtained applying PIV to the emulsion phase. Then, the bubbles geometry was exported to a finite element program and applying the equations proposed by Davidson (Davidson J.F., 1961. Symposium on fluidisation-Discussion. *Transactions of the Institution of Chemical Engineers*, vol. 39, pp. 230-232) the gas velocity field and the pressure field were computed with a low computational cost. Different kinds of bubbles were analysed: slow and fast, but also erupting and interacting bubbles. Moreover, the effect on the gas flow of the non-zero horizontal velocity component in fast bubbles has been analysed and the gas interchange between such bubbles and the main gas stream is studied.

In Chapter 3, the novel method explained in chapter 2 was extended to take into account non-Darcy effects. The Darcy's law proposed by Davidson's model was replaced by Ergun's equation, which takes into account both inertial and viscous effects. The

same cases analysed in chapter 2 were studied including non-Darcy effects, showing that these effects become important when the local gas velocity, and consequently the local Reynolds number, increase. These local differences do not affect appreciably the gas streamlines around bubbles for the experimental conditions of this work.

Chapter 4 presents a new methodology to obtain the voidage distribution around bubbles. The experimental set-up consists of a high speed video-camera, a 2-D fluidized bed and a source of diffuse light placed at the rear of the bed, opposite to the camera. As a result, a new correlation for voidage distribution around bubbles is proposed, which differs from previous correlations appearing in literature in two facts. First, it was obtained for a region adjacent to the bubble contour ($r/R_b \lesssim 1.2$), where a poorer spatial resolution precluded to do so in previous studies. Second, a radial symmetry was not assumed, and the voidage depends on the radial position and on the polar angle $\epsilon = \epsilon(\theta, r)$. The effect of the voidage distribution on the throughflow crossing the bubbles was also analysed. A 20% increase was obtained for the average bubble geometry of the more than 100 bubbles analysed.

Chapter 5 presents an experimental study of the solid ejection velocity in gas-solid fluidized beds. The mechanisms previously observed by Levy et al. (Levy E.K., Caram H.S., Dille J.C. and Edelstein S., 1983. Mechanims for solid ejection from gas-fluidized beds, *AIChE Journal*, vol. 29, pp. 383-388) are studied. The results show that, in isolated erupting bubbles, a group of particles raining in the form of stalactites within the bubble notably reduces the dome velocity. The highest particle ejection velocities were obtained when bubble coalescence occurs, specially if the wake spike mechanism is involved. In the jet spike mechanism, the collisions between particles notably reduces the ejection velocity. Although the isolated bubble eruption mechanism is the most frequent, the TDH must be calculated taking the maximum initial ejection velocity for a proper design of a fluidized bed.

Chapter 6 presents a new model to obtain the velocity profile of the particles ejected from the bubble dome in isolated erupting bubbles. This simple model is valid not only for vertical-ascent circular bubbles. It assumes that the ejection velocity depends on both bubble velocity and bubble growth velocity. The experimental results show that, except in some isolated cases, the model properly predicts the magnitude and direction of the maximum velocity and the velocity profile.

Chapter 1

Introduction

The process of fluidization can be defined as the *operation through a group of solid particles transform to liquid-like behaviour by the contact with a stream of a gas or a liquid*. In this way, a typical fluidized bed consists of a vessel filled with particles up to a determined fixed bed height, which lie on a gas distributor located at the bottom of the vessel. The fluidizing fluid, which can be a gas or a liquid, is introduced through the distributor. When the fluid velocity is able to support the weight of the particles, the bed is at minimum fluidization conditions.

This chapter presents a brief introduction to fluidized beds technology. Focus is on the explication of Davidson's model and the evolution of research on dynamics of bubbling fluidized beds from Davidson's model up to CFD. In addition, the most important industrial applications of fluidized beds from the 1920's up to the 21$^{\text{st}}$ century are briefly explained, with special attention to fluidized bed combustors.

1.1 On the liquid-like behaviour of fluidized beds

In a fluidized bed, when the superficial gas velocity exceeds the minimum velocity to support the weight of the particles, the bed adquieres some properties similar to a liquid. Some easy experiments permits to observe this behaviour:

1. An object with a characteristic length higher than the particle size and a density lower than the bulk density of the bed floats on the surface of the bed, in the same way as a "rubber duck" floats in a bath. If the density of the object is higher, it remains at the bottom of the bed.

2. If a hole is opened at the bed wall, a jet of particles is drained with a velocity approximately equal to $\sqrt{2\,g\,H}$, where H is the bed height.

3. The bed surface remains horizontal even if the vessel is inclined.

4. The static pressure at a point within the bed is approximately equal to the weight of particles over that point per cross sectional area of the bed.

In addition, when the fluidizing agent is a gas, bubbles appear at the distributor level and they grow and coalesce along the bed, until they reach the bed surface. These gas bubbles have some similarities with those ascending in a liquid medium. Davidson et al. (1977) made an extensive review on the size, shape, formation, rising velocity and coalescence of bubbles in gas fluidized beds and their similarities with gas bubbles in liquids.

1.2 Particle classification and fluidization regimes

From the beginning of research on fluidization, two different behaviours were clearly observed. When the particles are fluidized with a liquid (water, for example), the bed expands homogenously and no bubbles are observed. This type of fluidization was called "*particulate fluidization*". In contrast, if the solids are fluidized by a gas (typically air), bubbles appear just when the superficial gas velocity exceeds the minimum fluidization velocity. These gas pockets grow and coalescence along the bed height until they reach the bed surface. This fluidization type was called "*aggregative fluidization*".

Geldart (1973) made a classification of the different types of fluidization that has been widely used since then and accepted as a standard by the fluidization community. Geldart divided fluidization types in four different groups (see figure 1.1) depending on the particle size d_p and on the difference between solid and gas densities $\rho_s - \rho_g$. Therefore, for a given fluidizing agent, the fluidization type is defined by the particle characteristics. The four particles types are:

Type A particles: particles of small size and/or low density (around $1500\,kg/m^3$ or lower). A fluidized bed filled with these type of particles expands notably before bubbles appear and collapses slowly when the gas flow is cut off. Gas bubbles rise faster than the gas percolating through the emulsion. FCC particles are a typical example.

Type B particles: this kind of particles contains most of the particles of medium size ($40 \leq d_p \leq 500\,\mu m$) and density ($1500 \leq \rho_p \leq 4000 kg/m^3$). Most of the industrial applications use type B particles, as for example, the inert particles used in biomass and coal combustors to assure a good fluidization quality. Bubbles appear within the bed at, or only slightly above, minimum fluidization velocity. The bed expansion is small and the bed collapses rapidly when the flow is cut off.

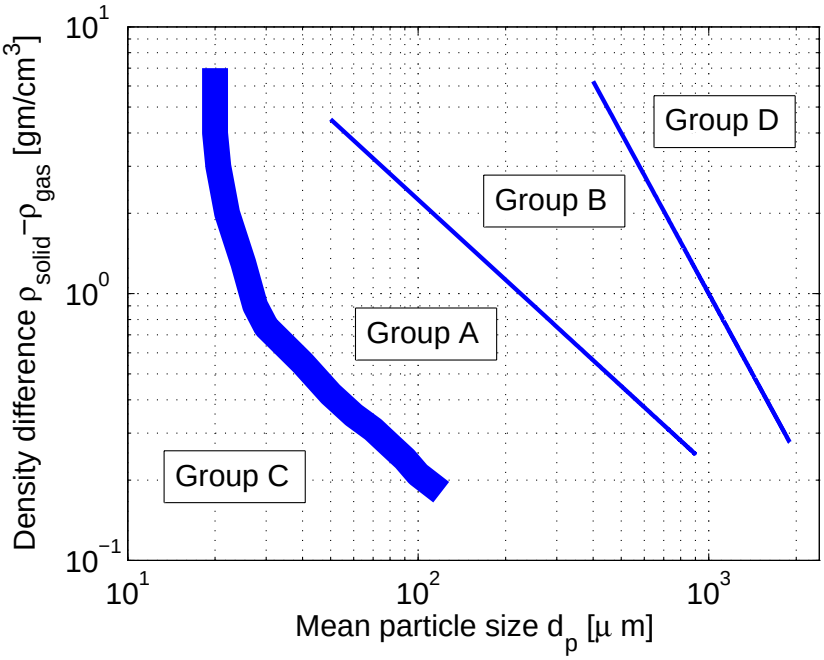

Figure 1.1: Geldart's classification diagram for particles fluidized by atmospheric air (adapted from Geldart (1973)).

Type C particles: particles of very small size (around $d_p = 40\,\mu m$ or bellow). The fluidization process of these particles is dominated by the interparticles forces, thus a good fluidization is difficult to achieve. Usually, channels (also called rate-holes) appear in the bed when it is fluidized. These channels bypass the fluidizing gas, resulting in a poor particle-fluid contact and mixing. An example of type C particles are flour powders.

Type D particles: particles very large or with high density. It is difficult to achieve a good fluidization in deep beds due to the appearance of spouts. Bubbles rise more slowly than the rest of the gas percolating through the emulsion. Roasting coffee beans are an example of these particles.

The four groups of particles defined by Geldart (1973) can be also analysed from the point of view of the different forces that appear in the fluidization process (Molerus, 1982). In type C particles, cohesive interparticle forces are the dominant, while during fluidization of type D particles, gravity forces are the more relevant. In contrast, the gravity and the drag forces have similar importance during the fluidization of type B particles. Finally, for type A particles the three forces, gravity, drag and cohesive, are of the same order.

Geldart's classification was obtained from experimental results of particles fluidized by atmospheric air. Grace (1986) extended Geldart's classification scheme to other gases and for a wide range of temperatures and pressures. Moreover, Grace (1986)

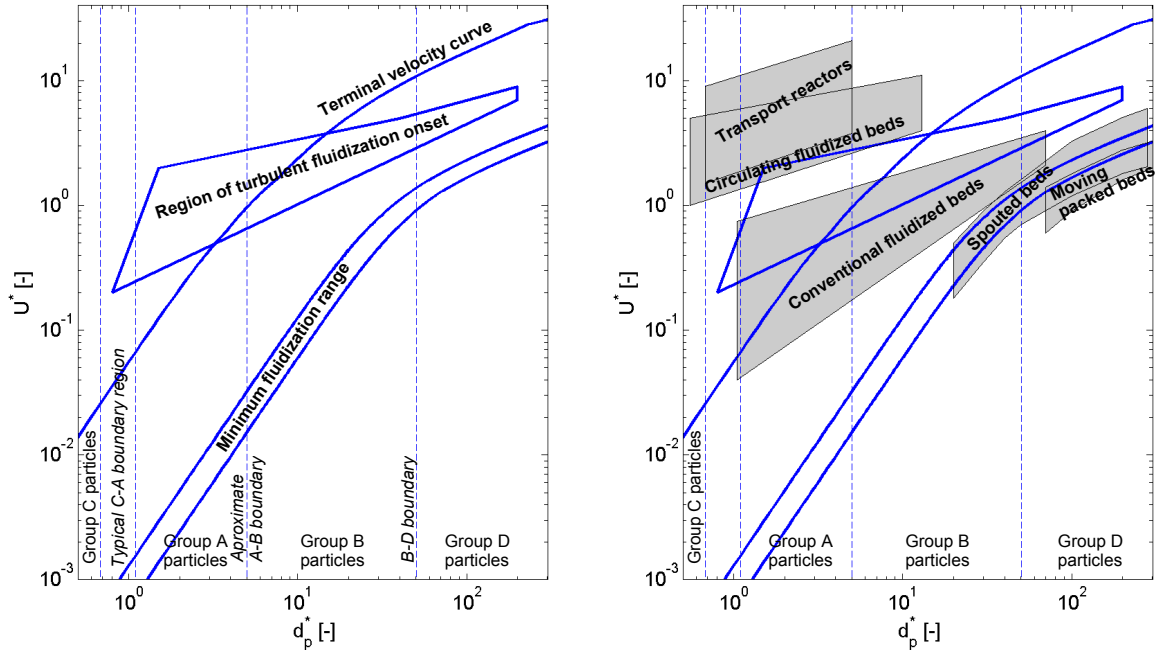

(a) (b)

Figure 1.2: General flow regime diagram for the whole range of gas-solid contacting (adapted from Grace (1986)). The minimum fluidization range reflect the differences in the choice of the mean particle diameter and the experimental scatter for different correlations. The approximate boundary for A-B transition has been calculated for $\rho_{solid} - \rho_{gas} = 1000 - 2000\, kg/m^3$.

presented his diagram using the non-dimensional variables:

$$d_p^* = Ar^{1/3} = d_p \left[\frac{\rho_g\, g\, (\rho_s - \rho_g)}{\rho_g}\right]^{1/3} \quad \text{and} \quad U^* = U \left[\frac{\rho_g^2}{\mu_g\, g\, (\rho_s - \rho_g)}\right]^{1/3} \tag{1.1}$$

Figure 1.2 shows the map of fluidization regimes presented by Grace (1986). Figure 1.2(b) shows different grey colored regions, which represent typical operation conditions for different reactors. The boundaries of these regions are not fixed and some reactors may lay beyond these boundaries, although most of industrial reactors operate within the regions indicated.

1.3 Davidson's model

Davidson's model (Davidson, 1961; Davidson and Harrison, 1963) was the first attempt to model particle-fluid dynamics around bubbles in fluidized beds. In spite of its simplicity, this important breakthrough was *"...the seminal concept that guided research and advanced understanding of dense bubbling fluidized beds..."* (Kunii and Levenspiel, 1991). Moreover, it distinguishes between slow and fast bubbles and properly predicts

the pressure field around bubbles.

Davidson's model assumed both gas and particle phases as incompresible fluids and that the void fraction is constant everywhere outside the bubble and equal to the one at minimum fluidization conditions ϵ_{mf}. In addition, Davidson assumed that the relative velocity between gas and particle streams are proportional to the gas pressure gradient, in agrement with the well known Darcy's law for porous media. With these assumptions, the equations of motion proposed by Davidson are

$$\nabla \cdot \boldsymbol{u} = 0 \tag{1.2}$$

$$\nabla \cdot \boldsymbol{v} = 0 \tag{1.3}$$

$$\boldsymbol{u} - \boldsymbol{v} = -\frac{k}{\mu} \nabla p_f \tag{1.4}$$

where $\boldsymbol{u}$ and $\boldsymbol{v}$ are respectively the interstitial gas velocity and the particle velocity, p_f is the fluid pressure, k is the permeability of the medium and μ is the fluid viscosity.

Combining equations (1.2) to (1.4) the following expression for the pressure field is obtained:

$$\nabla^2 p_f = 0 \tag{1.5}$$

This result indicates that the pressure field is undisturbed by the motion of the particles as the same result is obtained for a fixed bed.

In the 2-D case, Davidson's model provides four equations to obtain five unknowns (u_x, u_y, v_x, v_y and p_f). Therefore, an additional equation is needed. The additional closure equation comes from the assumption of irrotational particle flow. In this way, for an observer moving with the ascending bubble, the velocity potential (ϕ) and the stream function (ψ) for the particle phase are respectively

$$\phi = -U_b \left(r + \frac{R_b^2}{r} \right) \cos(\theta) \tag{1.6}$$

$$\psi = U_b \left(r - \frac{R_b^2}{r} \right) \sin(\theta) \tag{1.7}$$

The particle velocity components, expressed in polar coordinates for convenience, can be obtained as follows

$$v_r = \frac{\partial \phi}{\partial r} = \frac{-1}{r} \frac{\partial \psi}{\partial \theta} = -U_b \left(1 - \frac{R_b^2}{r^2} \right) \cos(\theta) \tag{1.8}$$

$$v_\theta = \frac{1}{r} \frac{\partial \phi}{\partial \theta} = \frac{\partial \psi}{\partial r} = U_b \left(1 + \frac{R_b^2}{r^2} \right) \sin(\theta) \tag{1.9}$$

The pressure distribution around bubbles must fulfil equation (1.5) and two bound-

ary conditions far from the bubble and at the bubble surface. Far from the bubble the pressure gradient must be equal to the pressure gradient without bubbles:

$$J = \bar{\rho}\, g = \left[\rho_g \left(1 - \epsilon_{mf}\right) + \rho_p \epsilon_{mf}\right] g \tag{1.10}$$

At the bubble surface the pressure must be constant. Therefore, the pressure distribution in the emulsion phase is obtained from the following expression

$$p_f = -J \left(r - \frac{R_b^2}{r}\right) \cos\left(\theta\right) \tag{1.11}$$

which satisfies equation (1.5) and the boundary conditions.

Combining equations (1.4), (1.8) and (1.9), and taking into account that far away from the bubble $u_{mf} = k\, J$, the components of the interstitial fluid velocity can be obtained as follows

$$u_r = v_r - k \frac{\partial p_f}{\partial r} = \cos\left(\theta\right) \left[\frac{R_b^2}{r^2} \left(U_b + u_{mf}\right) - \left(U_b - u_{mf}\right)\right] \tag{1.12}$$

$$u_\theta = v_\theta - k \frac{1}{r} \frac{\partial p_f}{\partial \theta} = \sin\left(\theta\right) \left[\frac{R_b^2}{r^2} \left(U_b + u_{mf}\right) + \left(U_b - u_{mf}\right)\right] \tag{1.13}$$

The stream function ψ_f for the gas flow has to fulfil the following equations

$$u_r = \frac{-1}{r} \frac{\partial \psi_f}{\partial \theta} \tag{1.14}$$

$$u_\theta = \frac{\partial \psi_f}{\partial r} \tag{1.15}$$

The two-dimensional stream function consistent with equations (1.12) to (1.15) is

$$\psi_f = \left(U_b - u_{mf}\right) \left(1 - \frac{A^2}{r^2}\right) r\, \sin\left(\theta\right) \tag{1.16}$$

where $\frac{A^2}{R_b^2} = \frac{U_b + u_{mf}}{U_b - u_{mf}}$.

According to equation (1.16), two different bubble types can be observed depending on the ratio between the interstitial gas velocity and the bubble velocity u_{mf}/U_b. When $u_{mf}/U_b > 1$ the bubble is slow. Figure 1.3(a) shows the gas and particle streamlines for a slow ascending bubble with $u_{mf}/U_b = 1.6$. In this case, the bubble acts as a preferential path for the gas flow which traverses from the bubble bottom to its roof. In addition, at both sides of the bubble there are small recirculation regions where the gas is dragged down by the particle motion and re-enters into the bubble without being in contact with the main stream. This kind of bubbles are typical of beds with large

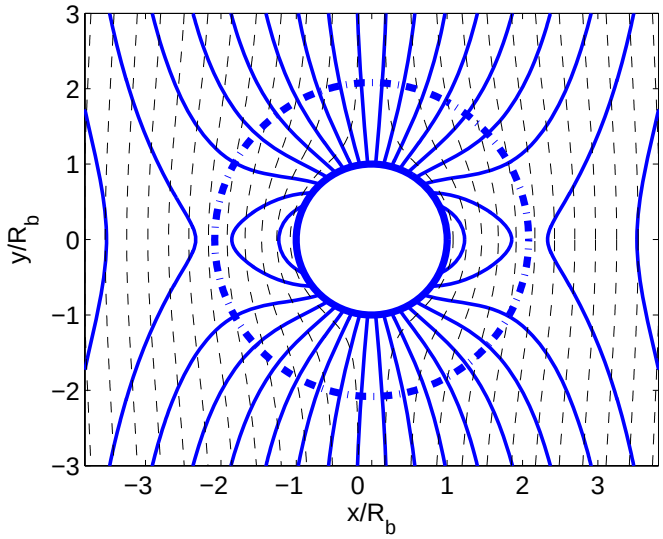

(a) $u_{mf}/U_b = 1.6$

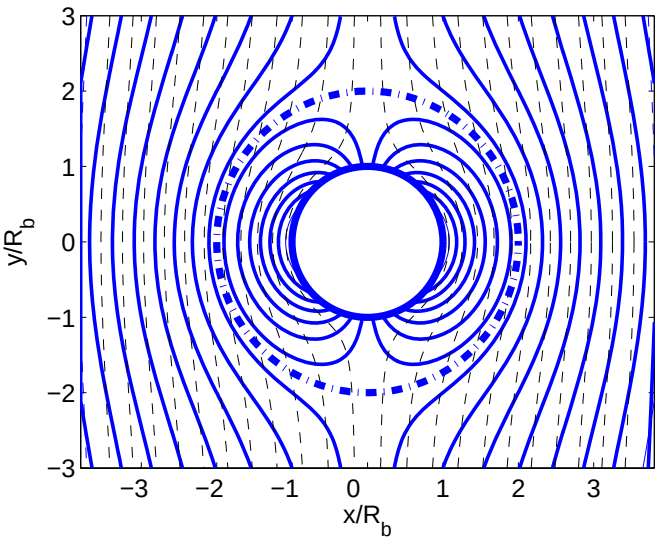

(b) $u_{mf}/U_b = 0.6$

Figure 1.3: Gas and particles streamlines for (a) a slow bubble and (b) a fast bubble. The solid lines indicate the gas streamlines and the dashed lines the particle streamlines for an observer moving with the bubble. The radius $A = R_b\sqrt{\frac{U_b+u_{mf}}{U_b-u_{mf}}}$ is plotted with a dash-dot line.

particles and small bubbles.

In contrast, a different behaviour is observed when $u_{mf}/U_b < 1$. Figure 1.3(b) shows a fast bubble with a ratio $u_{mf}/U_b = 0.6$. This type of bubbles are characterized by the presence of a recirculation cloud around the bubble which travels with the bubble while it is rising through the bed. The gas within the cloud does not enter into contact with the main stream. These bubbles appear when the bubble is big (the bubble velocity being proportional to the square root of its diameter) or when the superficial

gas velocity is low (small particles). In most of the fluidized bed applications fast bubbles are present in the bed.

Concerning the pressure field around bubbles, equation (1.11) is usually written referred to the pressure of the undisturbed bed at the same height:

$$\Delta p = p - p_{mf} = -J\left(r - \frac{R_b^2}{r}\right)\cos\theta - (-J\,r\cos\theta) = J\,\frac{R_b^2}{r}\cos\theta \tag{1.17}$$

where r is the radial distance from the center of the bubble. Introducing $r^2 = E^2 + y^2$ and $\cos\theta = \frac{y}{r}$ into equation (1.17), where E is the eccentricity (distance from the vertical axis of the bubble) and y is the vertical distance from the bubble center (see figure 1.5), the following expression is obtained

$$\Delta p|_{r\geq R_b} = J\,R_b^2\left(\frac{y}{E^2+y^2}\right) \tag{1.18}$$

Equation (1.18) is valid at any point outside the bubble. Within the bubble, the pressure is constant and equal to the weight of the particles measured at the bubble center height. Thus, Δp at any point within the bubble is merely the hydrostatic pressure:

$$\Delta p|_{r<R_b} = J\,r\cos\theta = J\,y \tag{1.19}$$

Figure 1.4(a) shows the non-dimensional pressure distribution around an ascending bubble. The pressure level $p_f = 0$ is located at the bubble height. Without the presence of the bubble the isobars are horizontal lines. In contrast, when a bubble appears, the pressure distribution in the bed is modified. The pressure within the bubble is constant and equal the pressure far away from the bubble at the same height.

Figure 1.4(b) shows the non-dimensional variable $\Delta p^* = \Delta p/\left(J \cdot R_b\right)$, which represents the effect of the presence of the bubble on the pressure value. Δp is maximum at the bubble nose and minimum at the bubble wake. In the region closer to the bubble, the influence of the bubble on Δp is more important, while this effect vanishes far from it.

Consider a pressure probe situated at a height h under the bed surface and at a distance y over the center of the ascending bubble. The height h does not change with time while the distance y varies as the bubble ascends. In addition, there is a certain eccentricity between the pressure probe and the vertical axis of the bubble (see figure 1.5). The measurements of the probe during the bubble ascent will show two major contributions: the hydrostatic weight of the particles located over the position of the probe, $p_{mf,h}$, and the effect of the bubble, Δp. When the probe is outside the bubble,

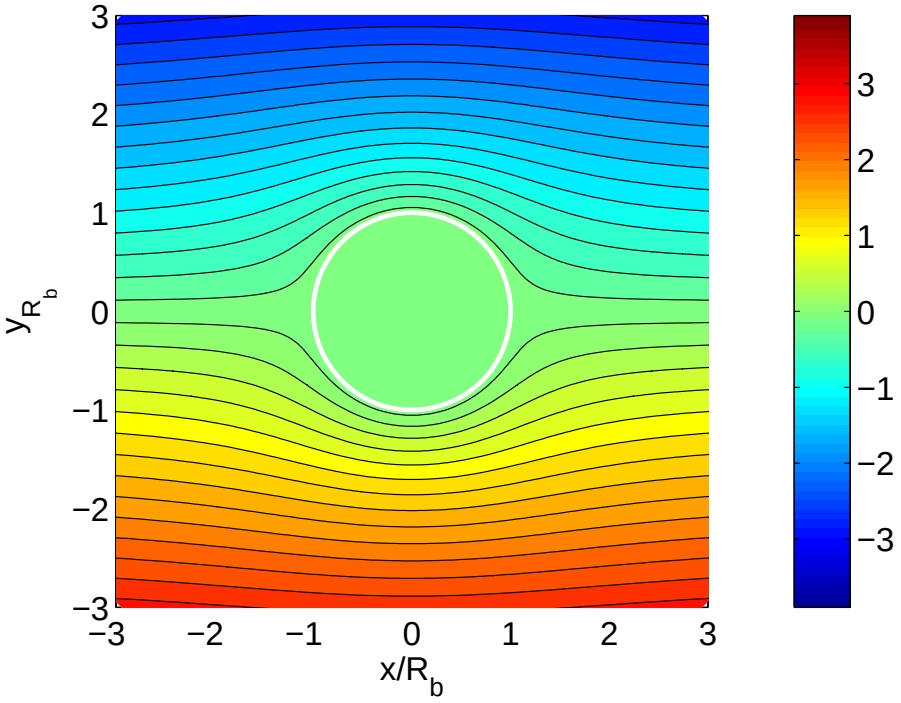

(a) $p_f^* = p_f / (J \cdot R_b)$

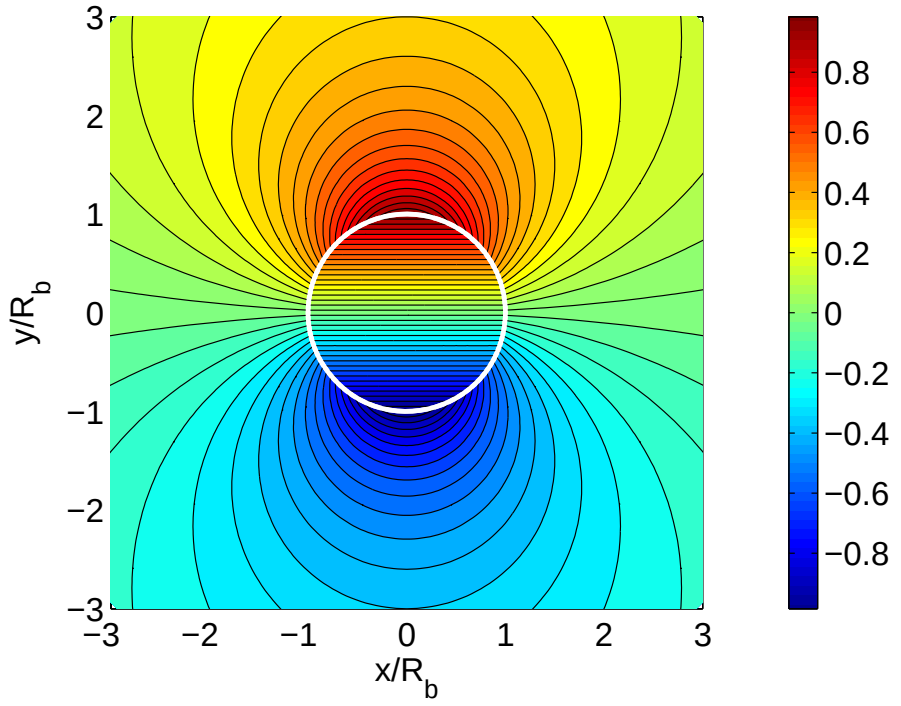

(b) $\Delta p^* = \Delta p / (J \cdot R_b) = (p_f - p_{mf}) / (J \cdot R_b)$

Figure 1.4: (a) Non-dimensional pressure field and (b) non-dimensional pressure difference according to Davidson's model.

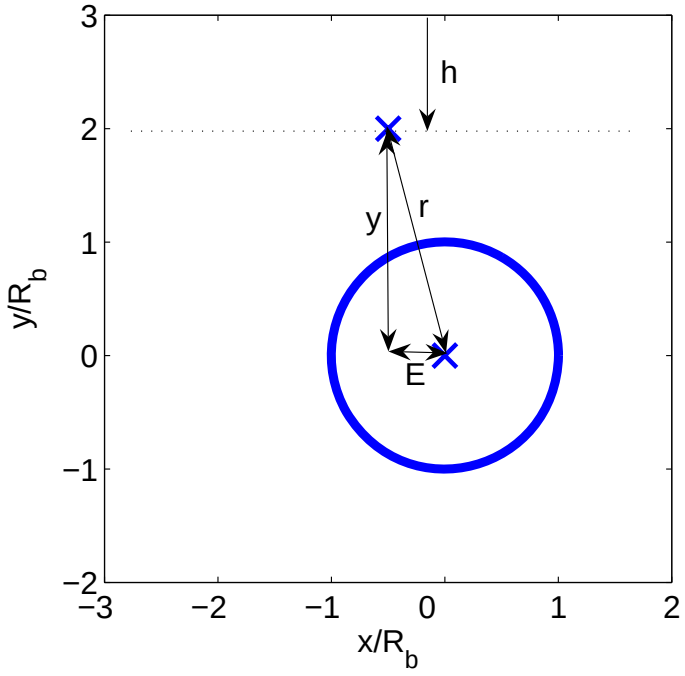

Figure 1.5: Scheme of the position of a pressure probe in the emulsion phase, where h is the depth under the bed surface.

the pressure value is

$$p_f|_{h,E,r\geq R_b} = p_{mf,h} + \Delta p|_{r\geq R_b} = J \cdot h + J\,\frac{R_b^2}{r}\cos\theta \tag{1.20}$$

and when the probe is inside the bubble ($r < R_b$)

$$p_f|_{h,E,r<R_b} = p_{mf,h} + \Delta p|_{r<R_b} = J \cdot h + J\,y \tag{1.21}$$

Figure 1.6 shows the non-dimensional pressure obtained from equations (1.20) and (1.21). The maximum and the minimum pressure are obtained at the bubble contour when $E = 0$, with a value of $p_{f,max}|_{E=0} = J\,(h + R_b)$ and $p_{f,min}|_{E=0} = J\,(h - R_b)$ respectively. As the eccentricity increases, the maximum and minimum values of the curve decrease, but they remains at the bubble contour until the eccentricity reaches a critical value $\widetilde{E}$. The coordinate y for the maximum pressure, assuming that the bubble ascends vertically, can be obtained as:

$$\frac{\partial\left(p_f|_{h,E,r\geq R_b}\right)}{\partial y} = J\,R_b^2\left(\frac{E^2 + y^2 - 2\,y^2}{\left(E^2 + y^2\right)^2}\right) = 0 \quad \Rightarrow \quad y = \pm\,E \tag{1.22}$$

Therefore, the maximum and the minimum values of the pressure curve are at $y = +\,E$ and at $y = -\,E$, respectively. Nevertheless, this result is only valid outside

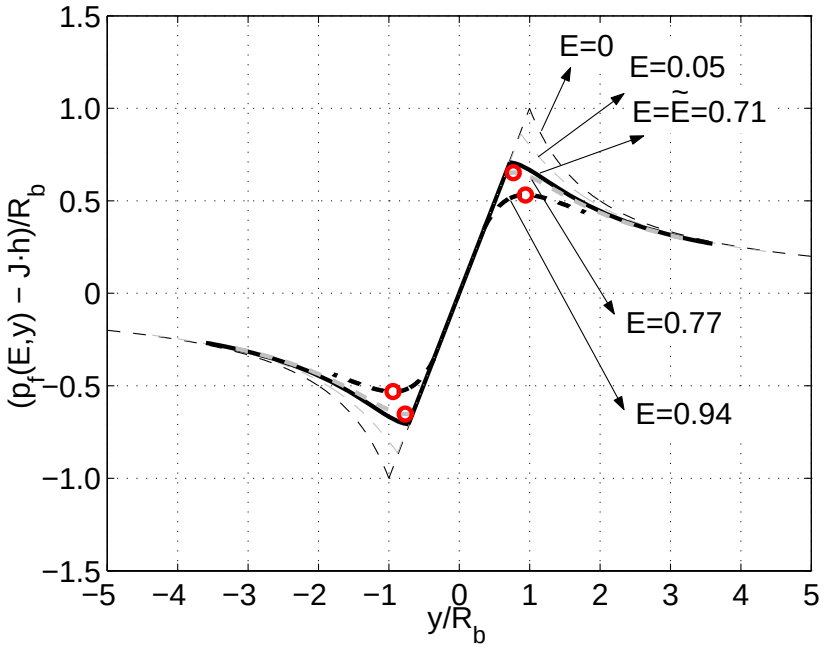

Figure 1.6: Non-dimensional pressure measurement of a theoretical pressure probe according with Davidson's model for different eccentricities. The circles indicate the maxima in the pressure curve when $E > \widetilde{E}$.

the bubble and consequently, the eccentricity has to fulfil the following condition

$$E = y \geq \sqrt{R_b^2 - E^2} \quad \Rightarrow \quad E \geq \frac{R_b}{\sqrt{2}} = \widetilde{E} \tag{1.23}$$

where $\widetilde{E}$ is the critical eccentricity.

Figure 1.6 shows the theoretical pressure measured by a hypothetical pressure probe for different eccentricities. If $E < \widetilde{E}$ the maximum and the minimum values of the pressure curve appear at the bubble contour. In contrast, when $E > \widetilde{E}$ the maximum and the minimum appear respectively before and after the probe touches the bubble contour. Thus, if a pressure probe is used to obtain the bubble size distribution in a fluidized bed (Santana et al., 2006) and the eccentricity of the probe is not taken into account, the mean bubble diameter could be overestimated.

All the equations showed in this section have been obtained for a 2-D circular bubble. Nevertheless, the reasoning is also valid assuming a 3-D sphere and replacing equations (1.6), (1.7), (1.8), (1.9), (1.11), (1.12), (1.13) and (1.16) by

$$\phi = -U_b \left(r + \frac{R_b^3}{2\, r^2} \right) \cos(\theta) \tag{1.24}$$

$$\psi = U_b \left(1 - \frac{R_b^3}{r^3}\right) \frac{r^2 \sin^2(\theta)}{2} \tag{1.25}$$

$$v_r = \frac{\partial \phi}{\partial r} = \frac{-1}{r^2 \sin(\theta)} \frac{\partial \psi}{\partial \theta} = -U_b \left(1 - \frac{R_b^3}{r^3}\right) \cos(\theta) \tag{1.26}$$

$$v_\theta = \frac{1}{r} \frac{\partial \phi}{\partial \theta} = \frac{1}{r \sin(\theta)} \frac{\partial \psi}{\partial r} = U_b \left(1 + \frac{R_b^3}{2\, r^3}\right) \sin(\theta) \tag{1.27}$$

$$p_f = -J \left(r - \frac{R_b^3}{r^2}\right) \cos(\theta) \tag{1.28}$$

$$u_r = \cos(\theta) \left[\frac{R_b^3}{r^3} (U_b + 2\, u_{mf}) - (U_b - u_{mf})\right] \tag{1.29}$$

$$u_\theta = \sin(\theta) \left[\frac{R_b^3}{r^3} \left(\frac{U_b}{2} + u_{mf}\right) + (U_b - u_{mf})\right] \tag{1.30}$$

$$\psi_f = (U_b - u_{mf}) \left(1 - \frac{A^3}{r^3}\right) \frac{r^2 \sin(\theta)}{2} \tag{1.31}$$

respectively, where $\frac{A^3}{R_b^3} = \frac{U_b + 2\, u_{mf}}{U_b - u_{mf}}$.

1.4 From Davidson's model to CFD

In a short time lapse after Davidson's model was published (Davidson, 1961), two new models appeared in the literature. Both of them extended Davidson's equations by including the particle momentum equation.

Jackson (1963a,b) proposed the following equations for modelling particle and fluid flow around bubbles

$$\nabla \cdot (\epsilon\, \boldsymbol{u}) = 0 \tag{1.32}$$

$$\nabla \cdot ((1 - \epsilon)\, \boldsymbol{v}) = 0 \tag{1.33}$$

$$\nabla p_f + \beta(\epsilon)\, (\boldsymbol{u} - \boldsymbol{v}) = 0 \tag{1.34}$$

$$\rho_p\, (1 - \epsilon)\, \boldsymbol{v} \cdot \nabla \boldsymbol{v} - \rho_p\, (1 - \epsilon)\, \boldsymbol{g} - \beta(\epsilon)\, (\boldsymbol{u} - \boldsymbol{v}) = 0 \tag{1.35}$$

Equations (1.32) to (1.34) are the same equations proposed by Davidson, if the voidage ϵ is assumed constant, and equation (1.35) is the particle momentum equation. Jackson (1963b) simplified the set of equations (1.32) to (1.35) assuming that the function $\beta(\epsilon)$ varies rapidly with ϵ. Therefore, a constant voidage value $\epsilon = \epsilon_{mf}$ can be assumed in all the terms, except in $\beta(\epsilon)$. An iterative method is necessary to solve the problem.

Murray (1965a,b) proposed the same system of equations (1.32) to (1.35), but the voidage variation was retained in all terms and the equations were linearized around

the value of the undisturbed variables far from the bubble. An analytical solution is possible.

Both Jackson (1963a,b) and Murray (1965a,b) obtained voidage values higher than ϵ_{mf} around the bubble and fulfilled the boundary condition of constant pressure far from the bubble. In contrast, neither of them obtained a constant pressure value at the bubble contour, because the bubble geometry is another variable to be solved in their models. Only assuming an appropriated bubble velocity, an approximately constant pressure is obtained in a region close to the bubble nose.

Several experimental works have tried to validate these models. As an example, Stewart (1968a) compared the ratio between the radius of the cloud and the radius of the bubble, for isolated injected bubbles. He concluded that both Jackson and Murray models (as they give similar results) predicts it better than Davidson's model, which seems to overestimate the cloud size. Nevertheless, experimental results of other researchers (Hatano and Ishida, 1982; Lignola et al., 1983) show inconclusive results concerning which model predicts the cloud size more properly (Kunii and Levenspiel, 1991). On the other hand, most of the experimental research on the pressure distribution around bubbles (Stewart, 1968a; Littman and Homolka, 1973; Croxford, 2006) agree with the fact that Davidson's model predicts it better than the others. In addition, Croxford (2006) assumed a freely fluidized bed in which the pressure distribution is the sum of the hydrostatic pressure and the sum of the contribution of each bubble in the bed (equation (1.17)). In this way, Croxford (2006) showed that Davidson's model is able to reproduce the pressure field produced by multiple bubble systems such as bubble streams and freely bubbling beds. But Davidson's model does not take into account bubble coalescence, bubble formation or bubble wake. Thus, these effects are only important in altering the position and size of the bubbles themselves, rather than alter the pressure field associated with the bubbles.

Up to this point, all the presented models were developed for circular (or spherical) bubbles. In contrast, experimental observations suggest that bubble geometry is not completely circular, specially in the wake (see for example figure 1 in Rowe and Partridge (1965)). Collins (1965) extended Davidson's model to 2-D kidney shape bubbles using a conformal transformation. For a 2-D circular bubble, the complex potentials for particle and gas flows, consistent with equations described in section 1.3, are given by

$$\omega_p = -U_b \left(z + \frac{R_b^2}{z} \right) \tag{1.36}$$

$$\omega_g = u_{mf} \left((1-\alpha)\, z - (1+\alpha)\, \frac{R_b^2}{z} \right) \tag{1.37}$$

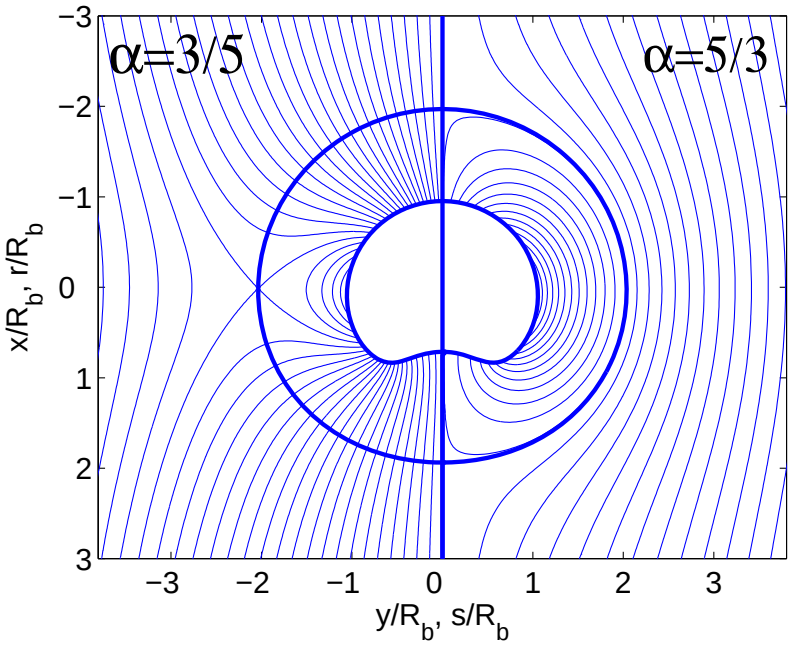

Figure 1.7: Gas streamlines for a kidney shape bubble. The left side shows a slow bubble with $\alpha = 3/5$ and the right side a fast bubble with $\alpha = 5/3$. Adapted from Collins (1965).

respectively, where $\alpha = U_b/u_{mf}$ and $z = x + i \cdot y$ is the complex variable. Collins (1965) suggested a transformation in the complex domain z and represented the bubble geometry in t plane:

$$t = r + i \cdot s = z + d - \frac{c^2}{z + d} \tag{1.38}$$

Choosing the parameters $c = \frac{2}{7}R_b$ and $d = \frac{5}{7}R_b$, a circular bubble of radius R_b centered at the origin is transformed into a kidney shape bubble similar to the ones observed in 2-D beds. Figure 1.7 shows the gas streamlines around a kidney shape bubble for two different ratios $\alpha = U_b/u_{mf}$. The left side shows the streamlines for a slow bubble with $\alpha = 3/5$, while the right side shows the fast bubble case with $\alpha = 5/3$. The results indicate that the streamlines and the cloud size are only slightly affected by the indentation near the indentation itself and its effect is negligible far from the bubble.

Clift et al. (1972) developed the analysis for an elliptical bubble following a similar procedure. They defined the complex plane

$$\zeta = \xi + i \cdot \eta \tag{1.39}$$

where ξ and η are elliptical coordinates, and used the following transformation

$$z = x + i \cdot y = c \cdot \cosh \zeta = c\,(\cosh \xi \cdot \cosh \eta + i \cdot \sinh \xi \cdot \sinh \eta) \tag{1.40}$$

where $c = \sqrt{a^2 - b^2}$ is the focal distance, $a = c \cdot \cosh \xi_0$ and $b = c \cdot \sinh \xi_0$ are the vertical and horizontal semi-axis respectively and ξ_0 is a constant which defines the ellipse contour. Clift et al. (1972) concluded that the clouds for elongated bubbles have lower eccentricity than the bubbles and their area are somewhat larger than the cloud area for the corresponding circular bubbles.

Grace and Harrison (1969) and Gera and Gautam (1994) showed that the throughflow crossing the bubble increases with the bubble aspect ratio $\tau = a/b$. For an elliptical bubble the throughflow in the ecuatorial plane of the bubble is

$$q_b = 2 \cdot U_{mf} \cdot b \cdot (1 + \tau) \tag{1.41}$$

while for a circular bubble $a = b = R_b$ and the throughflow is

$$q_b = 4 \cdot U_{mf} \cdot R_b \tag{1.42}$$

The same result was obtained by Davidson and Harrison (1963) from the original Davidson's model.

Clift et al. (1972) also analysed the case of two interacting bubbles of the same size without relative velocity between them. They extended previous works by including a circulation term Γ in the position of each bubble in order to get a better representation of the problem. The particle and gas stream functions including the circulation term are respectively

$$\begin{aligned} \psi_p &= -U_b \left[y - R_b^2 \left(\frac{y}{x^2 + y^2} + \frac{y - y_2}{(x - x_2)^2 + (y - y_2)^2} \right) + \right. \\ &\qquad \left. \frac{1}{2}\Gamma \left(\ln(x^2 + y^2) - \ln\left((x - x_2)^2 + (y - y_2)^2 \right) \right) \right] \end{aligned} \tag{1.43}$$

$$\begin{aligned} \psi_g &= y + \frac{U_b}{u_{mf}} \psi_p + \frac{1}{2} \left[\frac{x\, y}{(x^2 + y^2)^2} + \frac{(x - x_2)(y - y_2)}{\left((x - x_2)^2 + (y - y_2)^2 \right)^2} + \right] \\ &\quad + \frac{\Gamma}{4} \left[\frac{x}{x^2 + y^2} - \frac{x - x_2}{(x - x_2)^2 + (y - y_2)^2} \right] \end{aligned} \tag{1.44}$$

Figure 1.8 shows the gas (solid lines) and particle (dashed lines) streamlines lines around two interacting bubbles with $U_b/u_{mf} = 1.3$. The distance between bubbles is defined by $x_2 = y_2 = 2.5\, R_b$ and the value of the recirculation is $\Gamma = 0.41251$. The gas cloud of each bubble is not completely circular due to the interaction with the other bubble. For lower values of U_b/u_{mf} or for a shorter distance between bubbles, the gas streamlines crossing the trailing bubble can interact with the leading bubble and a unique cloud can encompass both bubbles.

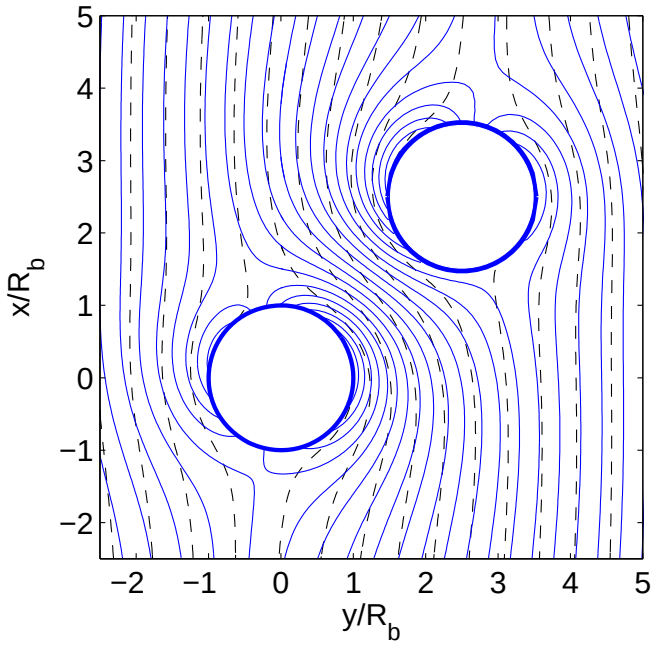

Figure 1.8: Two circular interacting bubbles with $U_b/u_{mf} = 1.3$ and $\Gamma = 0.41251$. The solid lines indicate the gas streamlines and the dashed lines the particle streamlines. No relative velocity between bubbles. Adapted from Clift et al. (1972).

When Geldart (1973) published his particle classification, he suggested an empirical criteria to distinguish between unstable fluidization (particles type B) and stable fluidization (particles type A). Nevertheless, the models of Jackson (1963a) and Murray (1965a) conclude that the fluidization phenomena is intrinsically unstable (Gibilaro, 2001), which suggest that the proposed equations ((1.32)-(1.35)) are not complete. Thus, fluidization research during the next years was focused on determining from first principles a criteria about the stability of the fluidization phenomena. Of special interest are the works of Foscolo and Gibilaro (Foscolo et al., 1983, 1985; Foscolo and Gibilaro, 1984, 1987).

At the same time, the appearance of computers and its continuos increase in computer performance allowed to solve numerically the equations of motion. Two main approaches can be found in the literature: Eulerian and Lagrangian. The Eulerian approach study both gas and particle phases as two interpenetrating fluids and the equations of motion are obtained averaging the equations in a volume higher than the particle size. The models of Davidson (1961), Jackson (1963a,b) and Murray (1965a,b) are clear examples of the Eulerian approach. On the other hand, in the Lagrangian approach, Newton's equations of motion are applied for each individual particle, together with a model of energy interchange for the collisions between particles (granular temperature).

Different works and books can be found in the literature related with CFD and

fluidized beds. Wide information about application of CFD in fluidized beds can be found in the books by Gidaspow (1994); Jackson (2000) and Gibilaro (2001). More recently, van Wachem and Almstedt (2003) made an extensive review about this field. The main drawback of the Eulerian approach is that there are more unknowns than equations and additional empirical correlations are necessary in order to close the problem, such as the interphase momentum transfer and the particle-particle interactions. In contrast, in the Lagrangian approach, the number of particles is limited due to the exponential increase in the computational cost with the amount of particles. Nowadays only a handful of particles can be simulated in a reasonable time.

Therefore, more efforts are necessary to overcame the disadvantages of the different CFD approaches, although this powerful tool seems to be the most promising technique for fluidized bed design in the future. As an example, in the last "Fluidization" conference (Fluidization XII, 2007) in Canada, the lectures were divided in 13 different fields. The CFD section was the one with the largest number of articles, with a total of 15 papers.

1.5 Historical development of fluidized beds

The first large-scale application of a fluidized beds with industrial interest was the gasification of coal, which was carried out in Germany by Fritz Winkler on December, 16, 1921. Winkler observed the mass of particles lifted by the drag of the gas to look like a boiling liquid (Basu, 2006). Nevertheless, the first unit ($13\,m$ high and $12\,m^2$ cross section) was not in smooth operation until 1926. The main drawbacks of this first fluidized bed application were its low efficiency and the loss of coal particles by entrainment. The gasification of coal was progressively replaced by petroleum feedstocks.

During the 40's, the main application of fluidized beds, developed by the Standard Oil Development Company (now ExxonMobil), merged into light: Fluid Catalytic Cracking (FCC). This company was working on the catalytic cracking of kerosene in order to cover the increasing demand of high-octane aviation gasoline in the United States. In those days, the Houdry process, using fixed beds, was not useful for large-scale production due to the necessary stops to regenerate deactivated catalyst. ExxonMobil engineers, in cooperation with Professors Lewis and Gilliland from the Massachusetts Institute of Technology, developed a complete pneumatic circuit of fluidized beds in which the spent catalyst could be withdrawn continuously from the reactor, regenerated in a separated vessel and then returned to the reactor. The first unit produced up to 13000 barrels per day when it went into smooth operation in 1942. Continued efforts are being made to improve the FCC process nowadays (Kunii and

Levenspiel, 1991).

Up to the end of the 60's, fluidized bed technology was widely used in the industry and the fluidization phenomena started to be understood from basic research. Geldart (1967, 1968, 1969) made a complete review of the different fluidized bed processes which were used in the industry up to those days, such as drying of powders, freezing food, petroleum cracking, acrylonitrile production, coal combustion, nuclear material processing, etc.. In 1968 more than 1000 fluidized bed applications were already patented (Geldart, 1968).

Soon after the petroleum crisis in 1972, the combustion of coal was recovered for power generation. In the next few years, pulverized coal combustion was used up to $40\,MW_{th}$ with an aceptable combustion efficiency although with very high emissions of SO_2 and NO_x. The use of fluidized bed combustors allowed to reduce the emissions of NO_x as a consequence of the lower and more homogenous temperature within the bed ($\sim 900°C$) and also the emissions of SO_2 by the addition of limestone ($CaCO_3$) in the bed. In quantities leading to molar ratios of Ca/S up to 5 it was possible to achieve a retention of over 95 % in the bed (Oka, 2004). Moreover, the fluidized beds allowed to use poor quality fuels.

The first generation of fluidized bed combustors (BFBC) works in the bubbling regime (*conventional fluidized bed* region in figure 1.2(b)) and achieves efficiencies up to 98 % with recirculation of unburned particles. In BFBC the heat is usually transferred to an internal heat exchanger with heat transfer coefficients up to $300\,W/m^2$. The main drawbacks of these first generation BFBC are the erosion of the internals by the inert particles and the problems to feed the fuel properly when the desired power is high, due to the large cross sectional area required.

The second generation of fluidized beds combustors, also called circulating fluidized bed combustors (CFBC), works in the fast fluidization regime (*circulating fluidized bed* region in figure 1.2(b)). These combustors have a smaller section, reducing notably the fuel feeding points in comparison with BFBC for the same thermal power. Moreover, the heat exchangers are situated at the bed walls, reducing the erosion problem and also increasing the combustion efficiency up to 99.5%. On the other hand, the main disadvantages of CFBC include their complexity, the more complex preparation of fuel and limestone and the difficulties with the start-up.

Figure 1.9 shows the evolution of the number of boilers of both technologies installed around the world. Nowadays, according to Oka (2004) BFBC are more economical for thermal powers bellow $50\,MW_{th}$ while CFBC are more appropriate for larger capacities.

The energy crisis in the 70's also triggered the development of a new generation of fluidized bed gasifiers. Their advantages against fixed beds (Basu, 2006) were a higher

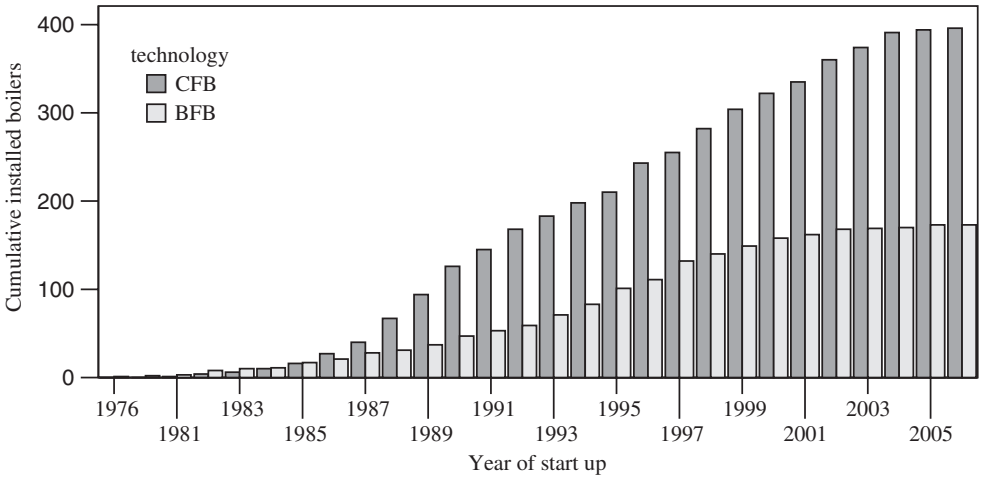

Figure 1.9: Diffusion of fluidized bed combustion for both variants from 1976. Adapted from Koornneef et al. (2007).

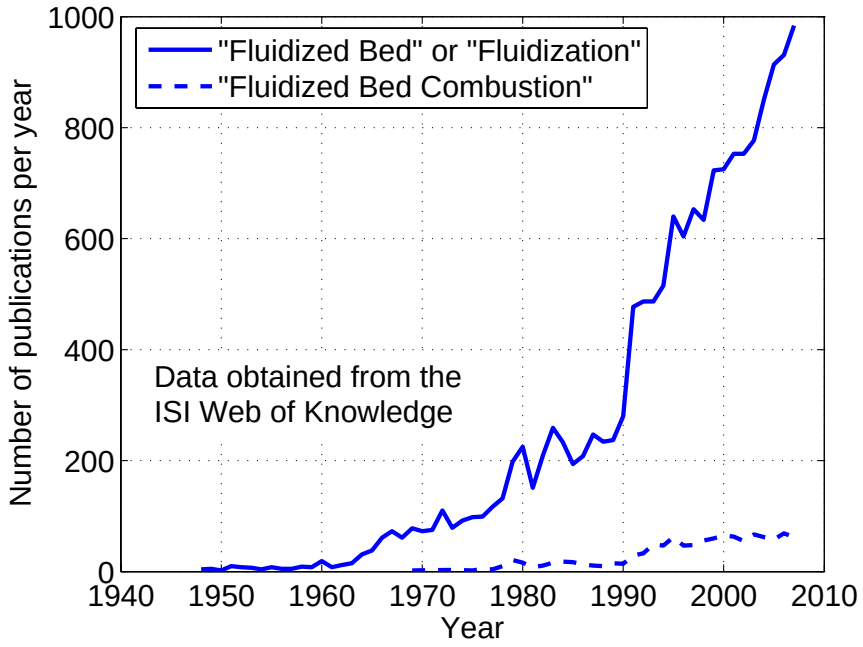

Figure 1.10: Evolution of the number of papers published per year related with "fluidized bed" or "fluidization" (solid line) and with "fluidized bed combustion" (dashed line). Figure adapted from Leckner (2005).

throughput, an improvement of heat and mass transfer from fuel, a high heating value of the gas and a reduction of the unburned char. Fluidized bed gasifiers are being widely used in biomass gasification rather than in carbon gasification due to the relative low bed temperatures (800 to 1000°C) necessary to avoid ash agglomeration.

In the 21^{st} century research and interest in fluidized beds technology and their applications is continuously increasing. Figure 1.10 shows the number of articles pub-

lished related to "fluidization" or "fluidized bed"[1] in all the journals of the ISI Web of Knowledge. From those, the papers related with fluidized bed combustion are also indicated. The number of articles increases progressively: from 1990 up to 2007 the number of publications increased up to a factor of 3 and continues to increase. This behaviour demonstrates that research is still necessary in order to understand properly this technology and its applications.

1.6 Scope of the thesis

This PhD thesis presents a study about gas and particle dynamics and solid ejection in bubbling fluidized beds. The study includes a numerical analysis using Finite Element Method (FEM) and an experimental part using digital image analysis techniques and Particle Image Velocimetry (PIV). Some of the experimental results are used as inputs for the numerical analysis.

All the experiments were carried out in a 2-D freely bubbling fluidized bed filled with Geldart B particles fluidized with atmospheric air. The 2-D geometry permits to observe the bubbles motion and to capture them using a high speed video-camera. The 2-D beds and the image analysis have been widely used in fluidized bed research from the early 60's (Massimilla and Westwater, 1960; Rowe et al., 1964; Rowe and Partridge, 1965; Grace and Harrison, 1969) up to the 21st century (Trisakti et al., 2001; Shen et al., 2004; Santana et al., 2005; Pallarès and Johnsson, 2006). Although the results obtained in 2-D beds are not directly extrapolable to a 3-D geometry, they provide very useful qualitative information to understand the behaviour of real fluidized beds. Different researchers (Ramos Caicedo et al., 2002; Villa Briongos and Guardiola, 2005) have studied how to extrapolate 2-D data to real geometries, although more effort is still necessary in this field.

On the other hand, different techniques have been also used trying to "observe" the interior of 3-D beds such as: X-rays (Rowe and Partridge, 1965; Yates et al., 1994), magnetic resonance imaging (Rees et al., 2006; Müller et al., 2006, 2007a) or capacitance imaging (Halow and Nocoletti, 1992). The main disadvantages of these techniques include a poor spatial and/or temporal resolution and restrictions in the bed dimensions and in the gas flow velocities. Although they provide useful time-average results, none of them are able to obtain instantaneous particles velocities. Moreover, the experimental results obtained in small-scale laboratory experiments, even when the experimental facility is 3-D, are difficult to scale-up to industrial bubbling fluidized beds. The main reason for this handicap is the bubble size, which is the prime factor

[1] Also the words "fluidisation" and "fluidised bed" from British English were used in the search

that control the conversion in a fluidized bed and cannot be reliably estimated from small-scale laboratory units (Levenspiel, 2008).

This PhD thesis has been organized in five different chapters (from chapter 2 to 6). Each chapter has been written as an independent article with its own abstract, introduction, notation and bibliography.

Chapters 2 and 3 present a novel numerical-experimental methodology to obtain particle and fluid dynamics in bubbling beds taking into account non-Darcy effects by combining PIV and FEM. In addition, the non-vertical ascent of fast bubbles has been studied, showing how these bubbles can interchange gas with the main stream.

Chapter 4 presents a new method to infer voidage distribution around endogenous bubbles in a 2-D fluidized bed. From the experimental data, a new correlation for the voidage distribution around bubbles is obtained. This correlation, unlike the previous appearing in literature, predicts voidage distribution in an adjacent region to the dome contour ($r/R_b \lesssim 1.2$) and it does not assume radial symmetry (it depends on both radial and tangential coordinates $\epsilon = \epsilon(r, \theta)$). In addition, the effect of the voidage variation around the bubbles on the throughflow crossing the bubbles has been studied, and an increase of a 20% was determined.

The last two chapters (chapters 5 and 6) are focused on the ejection of particles from the bed surface due to the erupting bubbles, that project solids to the freeboard. Chapter 5 presents an experimental study about the different mechanisms of solid ejection observed in gas-solid fluidized beds. The results show that particle ejection velocity is notably increased by bubble coalescence and the maximum ejection velocities are observed in the wake spike mechanism. Chapter 6 presents a new model for the velocity profile of the particle ejected from the bubble dome in isolated erupting bubbles. The model takes into account the bubble ascending velocity and its growth velocity and has been compared with experimental results.

Finally, in chapter 7 the main conclusions of the thesis are summarized and briefly discussed.

Chapter 2

A novel approach to characterize fluidized bed dynamics combining PIV and FEM

Contents

2.1 Abstract

This work presents a new experimental-numerical method combining PIV (Particle Image Velocimetry) and FEM (Finite Element Method), valid in a wide range of operational conditions, to obtain gas and particle motion around bubbles in a 2-D freely bubbling fluidized bed. The bubbles geometry is captured with a high speed videocamera while the particle velocity is measured using PIV. These experimental data are exported to a finite element software where the pressure and gas velocity fields are obtained at a very low computational cost.

The flow equations proposed by Davidson's model have been chosen to exemplify the application of the method presented in this chapter. Different bubble types have been analysed: slow and fast bubbles, but also erupting and interacting bubbles, all of them showing results in qualitative agreement with the modeled data for the simplest case of a circular bubble. In addition, the effect on the gas flow of bubbles with non-zero horizontal velocity component has been analysed. The results show that such bubbles interchange gas with the main stream. In chapter 3, this model has been extended to take into account non-Darcy effects.

2.2 Introduction

Fluidized bed technology has various applications in different fields of the industry. Some examples are: Fluid Catalytic Cracking (FCC), biomass and coal gasifiers and combustors or dryers. In most of the industrial applications (except FCC), the fluidizing powders used as inert particles to maintain a good fluidization quality are type B according to Geldart's classification (Geldart, 1973). For this type of particles, the minimum fluidization velocity is approximately equal to the minimum bubbling velocity. Therefore, when the bed is fluidized, bubbles appear, grow and coalescence along the bed height until they reach the bed surface, being these bubbles one of the dominant factors in determining the pressure distribution in the whole bed (Croxford, 2006) and the dominant frequencies in a bubbling bed (Johnsson et al., 2000). These bubbles have also an influence on the particle dispersion and therefore on the mixing in the bed (Pallarès and Johnsson, 2006).

The first attempt to model the flow of gas and particles around a bubble in fluidized beds was done by Davidson (1961). Davidson assumed both particle and fluid phases as incompresible fluids and the void fraction in the emulsion constant and equal to the one at minimum fluidization conditions, ϵ_{mf}. This assumption implies that all the excess of gas over minimum fluidization conditions traverses the bed in the form of bubbles (Toomey and Johnstone, 1952). In addition, Davidson's model assumed that the relative velocity between the interstitial gas and the particle is proportional to the gas pressure gradient, according to Darcy's law for porous media. With these simplifications, the governing equations of Davidson's model become

$$\nabla \cdot \boldsymbol{u} = 0 \tag{2.1}$$

$$\nabla \cdot \boldsymbol{v} = 0 \tag{2.2}$$

$$\tilde{\boldsymbol{u}} = \boldsymbol{u} - \boldsymbol{v} = -\frac{k}{\mu}\nabla p_f \tag{2.3}$$

where $\boldsymbol{u}$ and $\boldsymbol{v}$ are respectively the interstitial fluid velocity and the particle velocity, k is the permeability of the medium, μ is the fluid viscosity and p_f is the fluid pressure.

In the 2-D case[1], four equations are available in order to solve for five unknowns (u_x, u_y, v_x, v_y and p_f), so an additional closure equation is needed. Davidson's closure equation comes from the assumption of irrotational particle flow relative to the bubble, i.e., the particle and gas velocity fields can be obtained using the equations of the potential flow theory.

In addition, the set of equations (2.1)-(2.3) can be combined yielding the following expression for the pressure field

$$\nabla^2 p_f = 0 \tag{2.4}$$

This result indicates that the pressure distribution in the emulsion phase is not affected by the particle motion. The same result is obtained for a fixed bed.

Some years after, Jackson (1963a,b) and Murray (1965a,b) extended Davidson's model including the equation of change of momentum for the particles. Jackson's model includes the variation of the void fraction outside of the bubble in the permeability of the medium (k) and an iterative process is necessary in order to solve the problem. In contrast, Murray linearized the equations of motion around the value of the variables undisturbed far away from the bubble , providing an analytical solution. Both models fulfil the condition that the pressure far away from the bubble is equal to the weight of the particles per unit of area, but the resulting pressure field in the contour of circular or spherical bubbles is not constant because of the assumptions made in their models. This indicates that the geometry of the bubble is another unknown of the problem to be taken into account. Only assuming an appropriate bubble velocity, the pressure is approximately uniform in the region close to the nose of the bubble.

Different experimental works have been carried out in order to validate these models. As an example, the ratio between the cloud radius and the bubble radius for isolated injected bubbles was compared by Stewart (1968), concluding that the models of Jackson and Murray (both of them giving similar results) predict it better than the Davidson's model, which seems to overestimate the cloud size. In contrast, the high dispersion in the experimental results obtained by other researchers (Lignola et al., 1983; Hatano and Ishida, 1982) does not allow to conclude which model predicts the cloud size more properly (Kunii and Levenspiel, 1991). On the other hand, most of the experimental results found in the literature agree with the fact that Davidson's model gives better results for the pressure distribution around bubbles (Stewart, 1968; Littman and Homolka, 1973), which seems to be well-fit to a Laplacian field according to equation (2.4). More recently, Croxford (2006) corroborated these results for iso-

[1]Focus is set on the 2-D case, although derivation is also valid for the 3-D case.

lated injected bubbles and Croxford (2006) showed that Davidson's model can predict properly the pressure field in a stream of injected bubbles and in a freely bubbling fluidized bed across a wide range of flow rates.

From the 1980s up to present, there has been a growing interest in the use of CFD simulations in order to model the behavior of a fluidized bed. The development of CFD simulation tool also benefit from the continues increase in computer performance. van Wachem and Almstedt (2003) reviewed the state of the art in this field. Two main approaches can be found in the literature: Eulerian and Lagrangian. The former averages particle and fluid velocities over a volume higher than the particle size and the resulting equations are similar to the equations of two interpenetrating fluids (in fact, Davidson's model is the simplest Eulerian method). In the latter, Newton's equations of motion are applied for each individual particle, together with a model of energy interchange for the collisions between particles. The Eulerian approach needs some empirical correlations in order to close the problem (Jackson, 2000), whereas in the Lagrangian approach, only systems with a limited amount of particles can be computed because of the exponential increase in the computational cost with the number of particles. Thus, further development is necessary to solve this problems, although CFD seems to be the most promising fluidized bed design tool for the future.

In this work, a new experimental-numerical method for analyzing the gas and particle dynamics in a 2-D freely bubbling fluidized bed is presented. The bubble geometry was captured using a high speed video-camera. From the video-frames, the particle velocity field in the dense phase was obtained experimentally using a PIV technique similar to the one used by Müller et al. (2007). Then, the bubble geometry was exported to a finite element software where the gas velocity and pressure fields were computed numerically solving the flow equations. The computational cost of this new experimental-numerical method is very low in comparison with any of the CFD methods cited in the previous paragraph. Moreover, the finite element software easily allows the inclusion of a quadratic term into the momentum equation in order to compute non-Darcy effects, as will be explained in chapter 3

In the following, firstly the experimental set-up and the PIV technique used to measure the particle velocity are briefly described. Thereafter, methodology and expressions used in the finite element computations are analysed together with results obtained for slow and fast non-interacting bubbles and also for erupting and interacting bubbles. Finally the main conclusion and results of the work will be summarized and discussed.

2.3 Experimental set-up and PIV measurements

The experimental facility employed during the experiments was similar to the one described in Almendros-Ibáñez et al. (2006), that is, a 2-D ($110 \times 60 \times 0.5\, cm$) fluidized bed. The bed was illuminated from the front while having a black background in order to get high contrast between particles and bubbles. The size of each frame captured with the high speed video camera was approximately $25 \times 20\, cm^2$, which allows a proper application of PIV technique to obtain the particle velocity field around a bubble with the given camera resolution of 1.3 Megapixels. In all the pictures showed in this work the height level $y = 0$ corresponds to the air distributor and the height at which the bubble was captured is indicated in the vertical axis. The horizontal axis only indicates the scale. The pictures were captured from the central region of the bed with a rate of $250\, fps$ and an exposure time of $1/5000\, s$.

The particles were glass spheres with a mean diameter of $d_p = 350 \mu m$ and a density of $\rho_p = 2500 \frac{kg}{m^3}$ (type B according to Geldart's classification (Geldart, 1973)). The height of the fixed bed was around $30 - 35\, cm$ and the excess gas velocity in all experiments was in the range $U/U_{mf} \approx 1.1 - 1.3$, thereby avoiding particles to be entrained out from the bed.

The particle velocity field around bubbles was measured applying the PIV technique on the emulsion phase. Although, the displacement of the particles located in the first layer at the front wall is captured, the movement of these particles is representative of the movement of all particles within the bed, as Raso et al. (1965) showed experimentally. Note that the cross-correlation is applied to the whole emulsion inside of the PIV window rather than to a group of dispersed particles, as occurs in traditional PIV applications. Thus, the velocity vector obtained for each window represents the mean velocity of the approximately 100 particles contained in the 16×16 pixels window.

Two previous satisfactory studies using this technique in a bubbling bed can be found in the literature. Santana et al. (2005) measured the particle ejection velocity distribution from erupting bubbles in a freely bubbling bed. Later on, Müller et al. (2007) extended the work of Santana et al. (2005) measuring the particle velocity distribution not only in the dome contour of the erupting bubble but also in the emulsion around the bubbles breaking at the bed surface. They concluded that the flow of particles is irrotational except in a small region close to the wake of the bubble. Both of them used a camera with a resolution of $512 \times 480 = 0.25$ Megapixels, while a camera with a higher resolution of $1280 \times 1024 = 1.3$ Megapixels was used in the present study. With this resolution, a particle diameter to pixel size ratio of ~ 2 was obtained in an area of $\sim 25 \times 20\, cm^2$. Müller et al. obtained a similar ratio but with a lower spatial

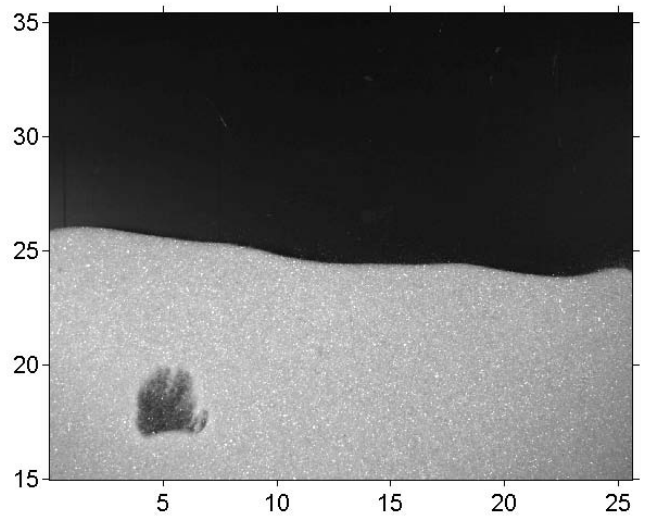

(a)

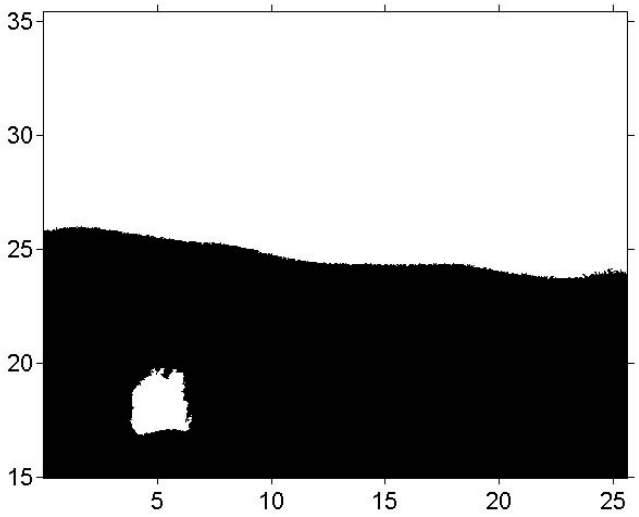

(b)

Figure 2.1: (a) Original picture and (b) black and white picture obtained from a threshold value. The particle velocity is not computed in the white region of picture (b) as it is assumed free of particles. Scale in cm.

resolution ($\sim 15 \times 15\, cm^2$) and higher particle diameters. The pictures were obtained at a frequency of $250\, fps$, and a shutter opening time of $200\, \mu s$ in order to properly capture the bubble geometry and to avoid blurring by the motion of the bubbles.

The PIV software employed in this study is the same used by Müller et al. (2007) in their work, MATPIV 1.6.1 (Sveen, 2004). Also, the same iterative method reducing progressively the size window and the same filters (signal-to-noise, global and local filters) used by them were applied in this work. The few dispersed particles inside

the bubble which rained down from the bubble roof have been neglected. However, these only constitute a small number. Thus, the software has been modified in order to detect automatically the bubbles geometry and the freeboard using a threshold algorithm (Otsu, 1979) and thereby these regions were masked.

Figure 2.1(a) shows the picture of one non-interacting slow bubble approximating the bed surface. By "non-interacting bubble" is meant a bubble in a freely bubbling bed located at least one bubble diameter away and with a recirculation which is not interacting with other bubbles. Thus, the bubble shown in figure 2.1 is not an isolated bubble. More bubbles were present in the bed at the same time, although they were not captured within the $20 \times 25\,cm$ region framed. Figure 2.1(b) shows the result of applying a threshold value to the picture showed in figure 2.1(a). The bubble interior and the freeboard are detected and excluded from PIV analysis since these regions are considered free of particles in the computations.

Müller et al. (2007) mixed white and black particles in order to obtain better contrast results. Nevertheless, the present study provides satisfactory results using only one kind of particles and no extra particles were needed. Figure 2.2(a) shows the PIV result obtained in the vicinity of the bubble shown in figure 2.1(a). The non-symmetry of the result is due to interactions with other bubbles which do not appear in figure 2.1(a). These bubbles approximate the leading bubble from the bottom-right zone of the picture. The gas flow from one bubble to the other drags the particles located between bubbles, leading to higher particle velocity in this region. Also the particles at the top of the bubble tend to move to right, as the bubble does, since the pressure gradient is higher in that region due to a lower level of the free surface of the bed. Figure 2.2(b) shows the magnitude of the particle velocity, where the higher velocity in the region close to the top of the bubble is distinguished clearer.

2.4 Numerical analysis

With the experimental data obtained by means of videorecording and PIV technique, the relative velocity between the gas and the particles, $\tilde{\boldsymbol{u}}$, and the pressure field, p_f, were computed using a finite element software (Comsol Multiphysics). Firstly, the geometry of the bed is exported to this software, where an unstructured mesh is created automatically in the domain. This mesh is finer close to the boundaries (where a change in permeability k occurs) as figures 2.3(a) and 2.3(b) shows. The mesh plotted in figure 2.3(a) has $\sim 5 \cdot 10^4$ triangular elements.

Figure 2.3(a) shows the addition of a rectangle, $15\,cm$ in height, under the geometry captured by the camera, resulting in a computational bed geometry of the same height

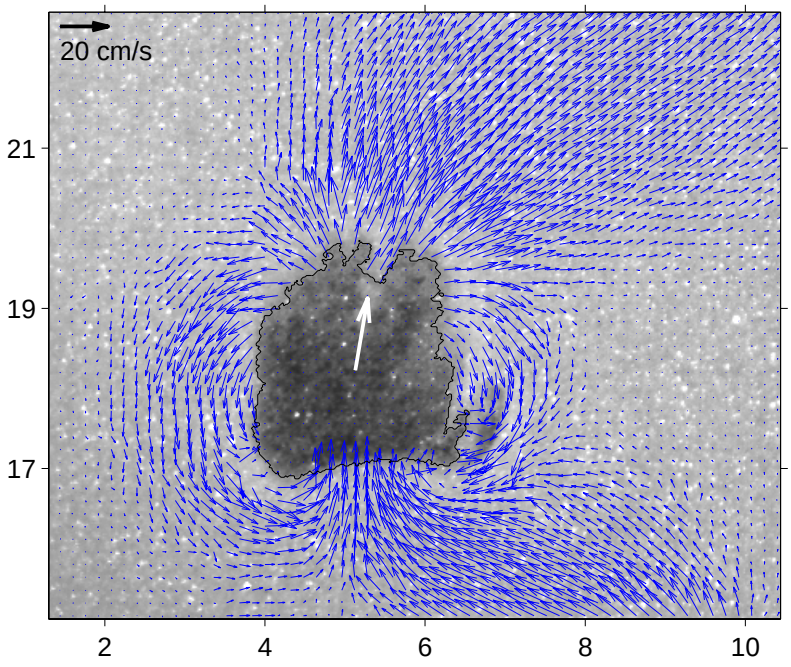

(a)

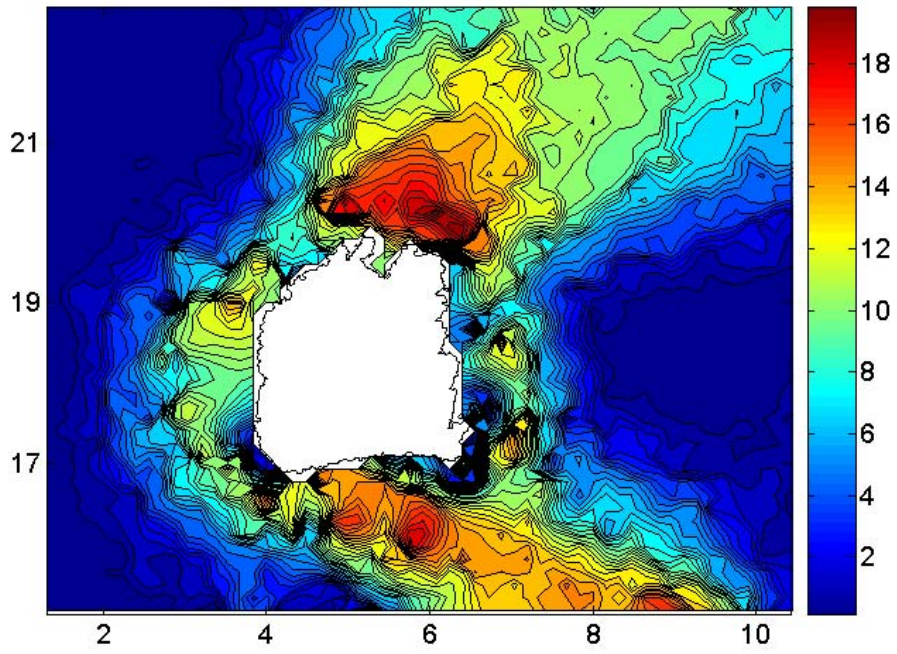

(b)

Figure 2.2: (a) PIV results (blue vectors) and bubble velocity $U_b = 0.31\, m/s$ (white vector) for the bubble showed in figure 2.1(a) and (b) particle velocity magnitude contours. Scale in cm and velocity in cm/s.

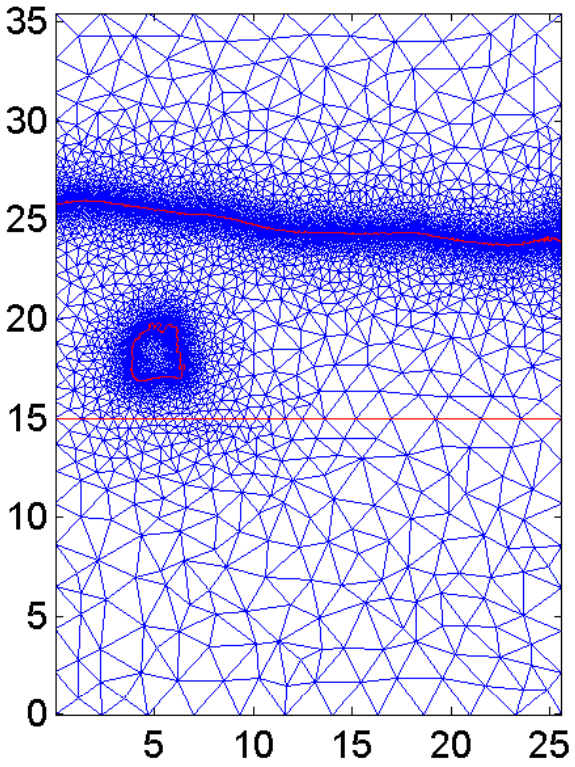

(a)

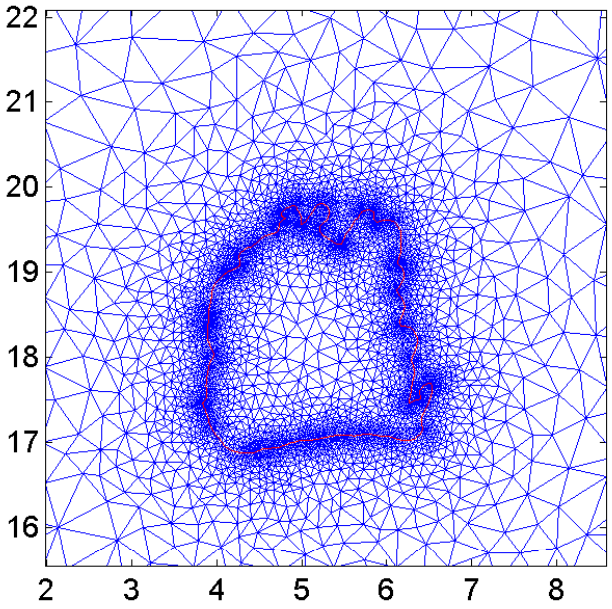

(b)

Figure 2.3: (a) Mesh created for the geometry showed in figure 2.1(a) and (b) detail of the mesh around the bubble. Scale in *cm*.

as the experimental bed geometry. This is done in order to enable proper implementation of the boundary condition at the bottom of the bed, as explained later on. With this rectangle, the effect of other bubbles, which could be present in the bed under the region photographed, is not taken into account. Anyway, this effect is negligible if the other bubbles are not very close to the bottom of the photographed region. In order to assure this, some frames after the selected bubbles where observed in order to corroborate that there is enough space between bubbles and their influence can be neglected. A higher bed area can not be captured because of the spatial resolution limitation for PIV measurements.

In this thesis, Davidson's model is chosen to illustrate the practical application of the method presented. Thus, the flow equations represented by equations (2.1)-(2.3) were implemented in the finite element software. Davidson's original model, which assumed a circular bubble, has analytic solution using the equations of potential flow (for a more detail description see Davidson and Harrison (1963)). Also, analytical solutions are posible for elliptical (Clift et al., 1972) and kidney shape bubbles (Collins, 1965). In contrast, for an actual bubble geometry with a non-well defined geometry as the one showed in figure 2.1(a), a numerical analysis is needed and an analytical solution is precluded.

With respect to the pressure field, different expressions for the permeability through a porous media, k, can be found in the literature. In this work, the linear term of Ergun's equation (Ergun, 1952), also known as the Carman-Kozeny equation:

$$k_e = \frac{\epsilon_{mf}^2 \left(\phi\, d_p\right)^2}{150\ \left(1-\epsilon_{mf}\right)^2} \tag{2.5}$$

has been used. For the experimental conditions of this work, a value of $k_e \sim 10^{-10}\, m^2$ was obtained. The regions of the domain free of particles (bubbles and freeboard) were modeled as regions with a permeability $k_b \gg k_e$. In this way, the gas pressure drop across these regions respect to the emulsion phase can be neglected and the pressure inside the bubbles will be approximately constant.

In order to study the influence of the permeability k_b in the model, the simple case of an isolated circular bubble with varying bubble permeability k_b, and constant emulsion permeability, $k_e = 10^{-10}\, m^2$, was analysed. Figure 2.4(a) shows the nondimensional superficial gas velocity in an equatorial plane parallel to the distributor that divides the bubble into two equal parts, for different values of k_b. As expected, the gas flow crossing the bubble (its center is situated at $x = 0$) is higher than in the emulsion phase due to its higher permeability and increases asymptotically to a maximum value of $U = 2{\cdot}U_0$, where U_0 is the value far away from the bubble. Thus, the gas flow crossing

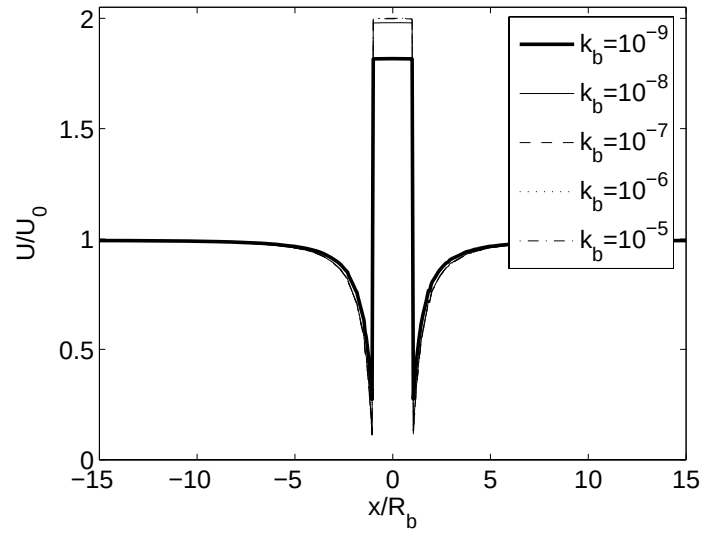

(a)

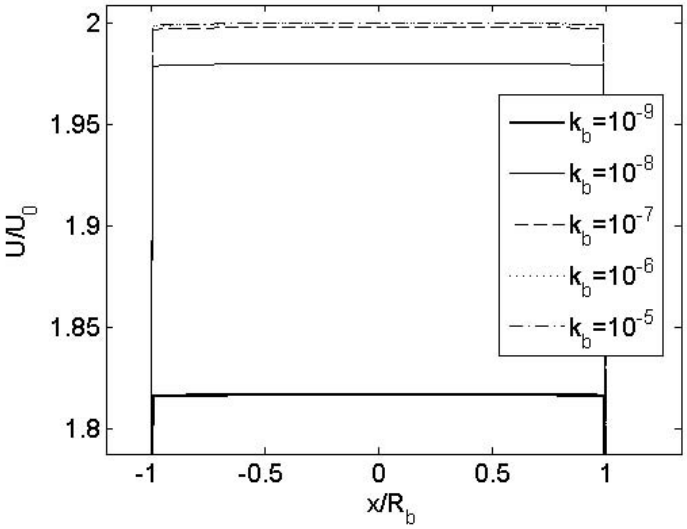

(b)

Figure 2.4: (a) Nondimensional superficial gas velocity crossing one isolated circular bubble in its equatorial plane for several values of k_b and (b) detail of the flow in the interior of the bubble. In all cases $k_e = 10^{-10}\, m^2$ and the units of k_b are m^2.

the bubble is $q = 4 \cdot U_0 \cdot R_b$. This result is equal to the one obtained by Davidson and Harrison (1963) using the potential flow theory for the exchange between the bubble and the emulsion phase. In consequence, the present numerical analysis agrees, in the simplest case of an isolated circular bubble, with the original results of Davidson's model. Figure 2.4(b) shows a zoom of the flow in the region $-R_b \leq x \leq R_b$ and no appreciable differences are observed for values of $k_b > 10^{-5}\, m^2$. Although it is not plotted, for high k_b values the pressure inside the bubble was constant and equal to

the pressure in a point situated at the same height as the center of the bubble and far away from such bubble, in agreement again with Davidson's model.

The boundary conditions chosen were atmospheric pressure in the freeboard and a pressure equal to the weight of particles at the bottom of the bed. The same boundary conditions were assumed by Croxford (2006) in order to solve the Laplace equation (equation (2.4)) to obtain the pressure field in the bed. For the lateral limits, a boundary condition of no-penetration, i.e. the pressure gradient perpendicular to the boundary is equal to zero, was imposed. Nevertheless, Croxford (2006) showed that this lateral boundary condition has little effect on the rest of the flow.

Note that by assuming the pressure at the bottom of the bed equal to the hydrostatic pressure, the effect of the gas discharge in the distributor is neglected, i.e. a perfect gas flow distribution is assumed. The flow at the region close to the bottom of the bed was visually inspected, observing an apparently homogeneous distribution of the flow. If the pressure drop across the distributor was not high enough, a different behavior could be observed in the bed, as the single or exploding bubble regimes observed by Johnsson et al. (2000). In this situations, the assumption of hydrostatic pressure at the bottom of the bed could not be correct.

From the numerical calculations, the relative velocity $\tilde{\boldsymbol{u}}$ is computed and the particle velocity $\boldsymbol{v}$ was obtained from the PIV measurements. Then, the interstitial gas velocity can be calculated as the sum of both of them

$$\boldsymbol{u} = \tilde{\boldsymbol{u}} + \boldsymbol{v} \tag{2.6}$$

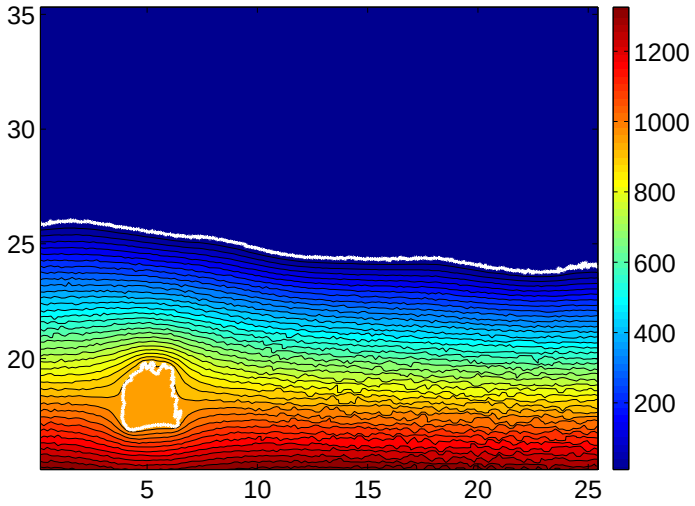

Figure 2.5: Pressure distribution around one bubble according to Darcy's law. Pressure in Pa and scale in cm. The atmospheric pressure is assumed as reference and equal to 0.

2.5 Slow and fast bubbles

The pressure distribution around a slow bubble obtained assuming the Darcy's law is shown if figure 2.5. This figure shows the distortion of the isobars by the presence of the bubble, whereas the pressure in its interior is constant. Also the fact that the bed surface is not horizontal forces the isobars to adapt to it. The pressure drop in the freeboard is negligible respect to the pressure drop across the bed due to the differences

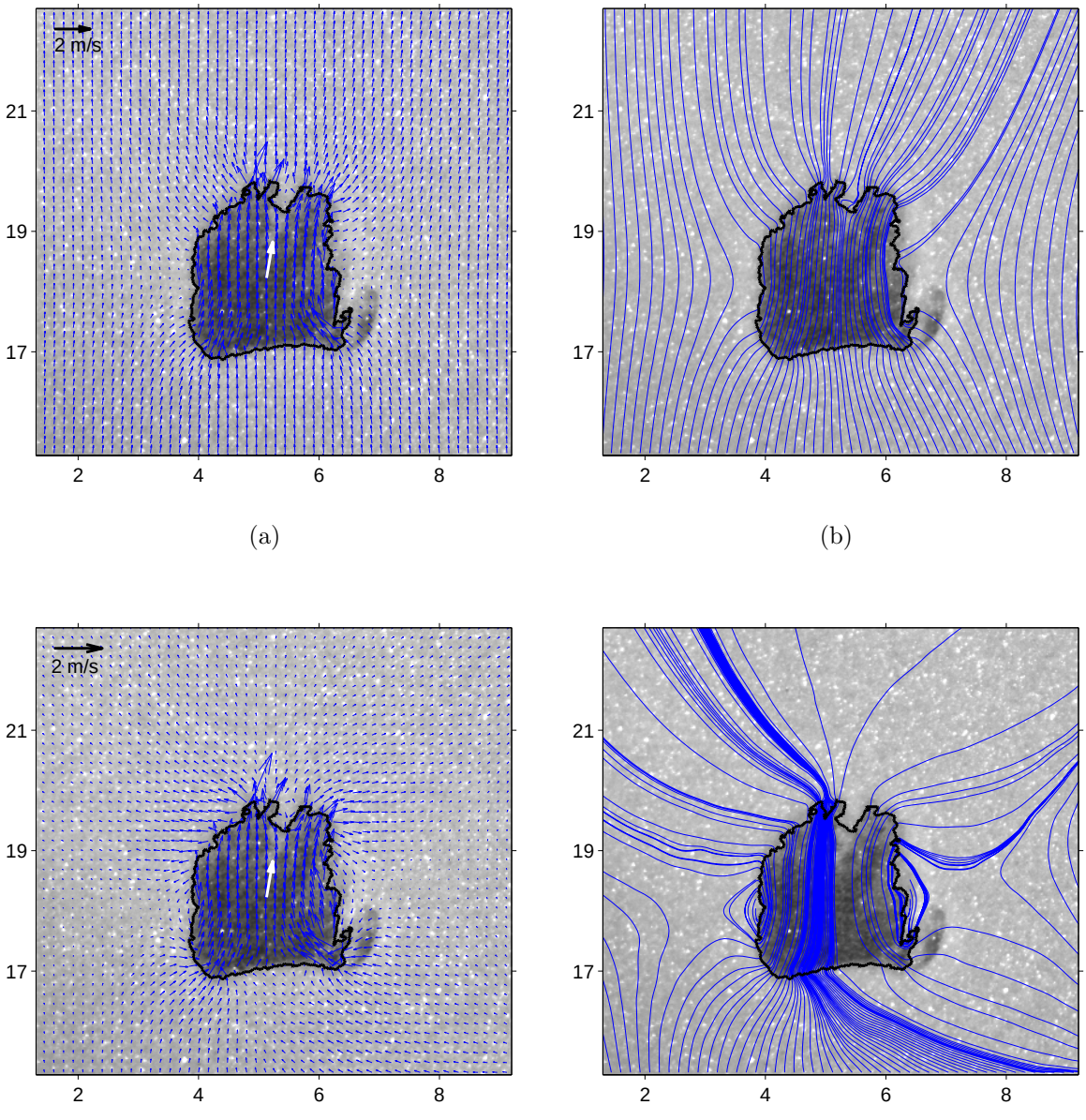

Figure 2.6: (a) Gas velocity vectors $\boldsymbol{u}$ and (b) streamlines as viewed by a stationary observer and (c) and (d) as viewed by an observer moving with the bubble. Slow bubble with $U_b/u_0 = 0.69$. White vector indicates the bubble velocity $U_b = 0.31\, m/s$. Scale in cm.

in the permeabilities of both mediums.

The interstitial gas velocity vectors and their streamlines are plotted in figures 2.6(a) and 2.6(b) respectively, as they were observed by a non-inertial viewer. Deviation of the gas streamlines trajectories in the vicinity of the bubble due to the more favourable path across the region of higher permeability is observed. Nevertheless, more interesting is to plot the velocity field as viewed by an observer moving with the bubble, as shown in figures 2.6(c) and 2.6(d). These figures show, for this slow bubble ($U_b < u_0$), two small regions in the laterals of the bubble where the gas recirculates and how the rest of the gas traverses the bubble from bottom to top, in agrement with the flow predicted by Davidson's model in the slow bubble case. The radius of the percolation circle that defines the limits of the lateral recirculation zones can be obtained using the 2-D Davidson's model as:

$$R_p = R_b \sqrt{\left| \frac{U_b + u_0}{U_b - u_0} \right|} = 3.12\, cm \tag{2.7}$$

where R_b has been calculated as the radius of the equivalent circular bubble with the same area. The circular bubble model seems to overestimate R_p which has a value of approximately $\sim 2.5\, cm$. This difference is owing to the non-circular geometry of the bubble and the non-axissymmetric particle velocity field.

A different behavior is predicted by Davidson's model when the bubble velocity is higher than the interstitial gas velocity. These fast bubbles are characterized by a cloud of gas recirculating in the bubble without penetration of external gas inside of this recirculation region. Figures 2.7(a) and 2.7(b) show the velocity vectors and the streamlines viewed by an stationary observer and figures 2.7(c) and 2.7(d) viewed by an observer moving with the bubble for a non-interacting fast bubble with a ratio between the bubble velocity and the interstitial velocity of $U_b/u_0 = 1.3$. Typical recirculation regions can be observed at both sides of the bubble, although an important part of the gas crosses the bubble from bottom to top and is not recirculated. This fact is the result of the non-vertical bubble ascent (note the appreciable horizontal component of the bubble velocity represented with a white coloured vector in figures 2.7(a) and 2.7(c))

In fact, Davidson's model shows a similar behavior for a circular bubble if an horizontal component is added to the bubble velocity. It is well known from Davidson's theory that the gas stream function for a circular bubble can be obtained as (Collins, 1965):

$$\psi_g = \psi_{g_0} + \psi_p \tag{2.8}$$

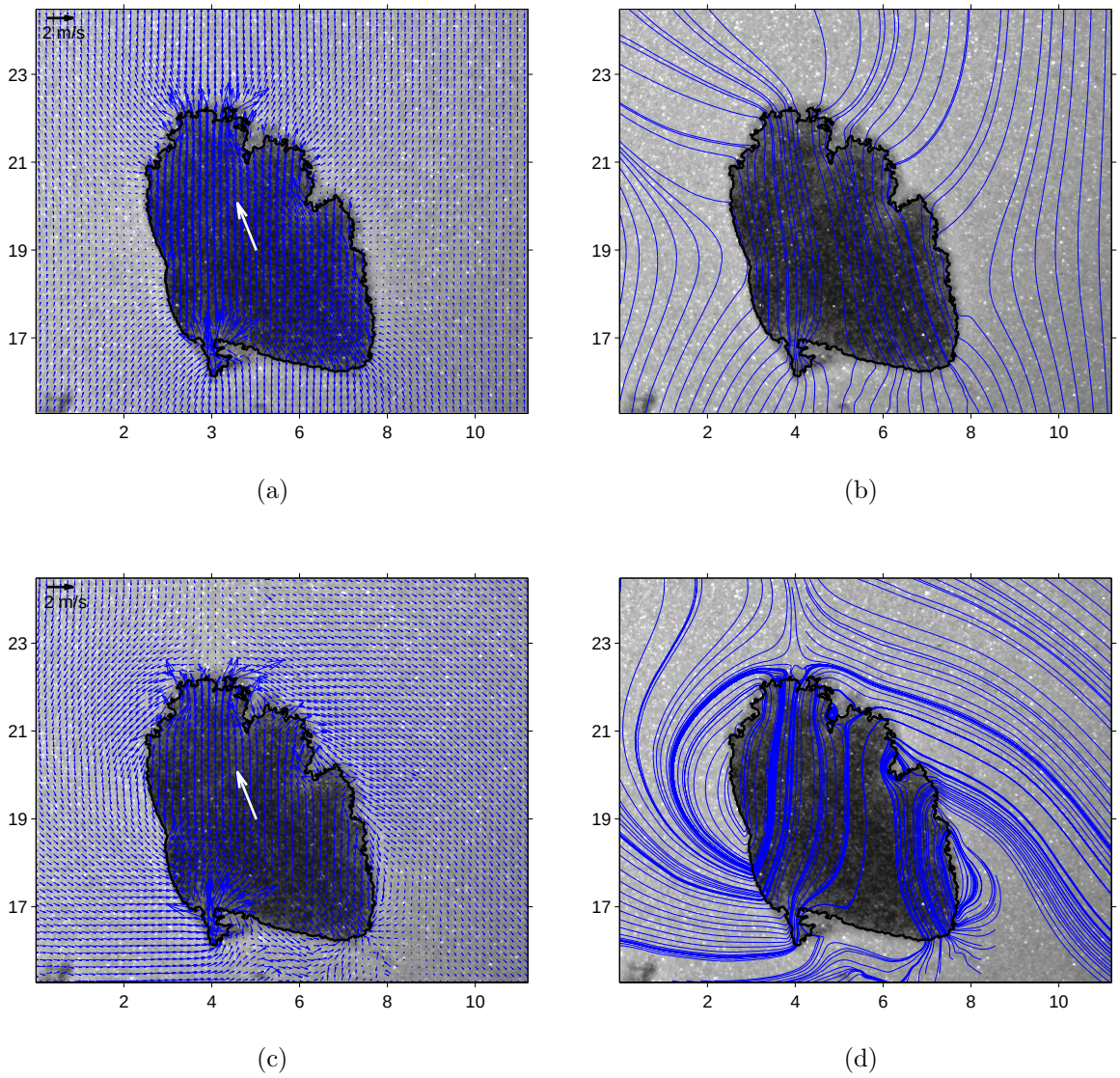

Figure 2.7: (a) Gas velocity vectors $\boldsymbol{u}$ and (b) streamlines as viewed by a stationary observer and (c) and (d) as viewed by an observer moving with the bubble. Fast bubble with $U_b/u_0 = 1.3$. White vector indicates the bubble velocity $U_b = 0.58\, m/s$. Scale in cm.

where

$$\psi_{g_0} = -u_0 \left(1 + \frac{R_b^2}{r^2}\right) r \sin(\theta) \tag{2.9}$$

is the gas stream function with $U_b = 0$, i.e., ψ_{g_0} represents the percolation of fluid through a fixed bed into a circle of radius R_b, and it is not affected by the bubble velocity. In contrast, the particle stream function ψ_p must be modified in order to take into account that the bubble is moving with a velocity forming and angle α with the vertical, that is

$$\psi_p = U_b \left(1 - \frac{R_b^2}{r^2}\right) r \sin(\theta + \alpha) \tag{2.10}$$

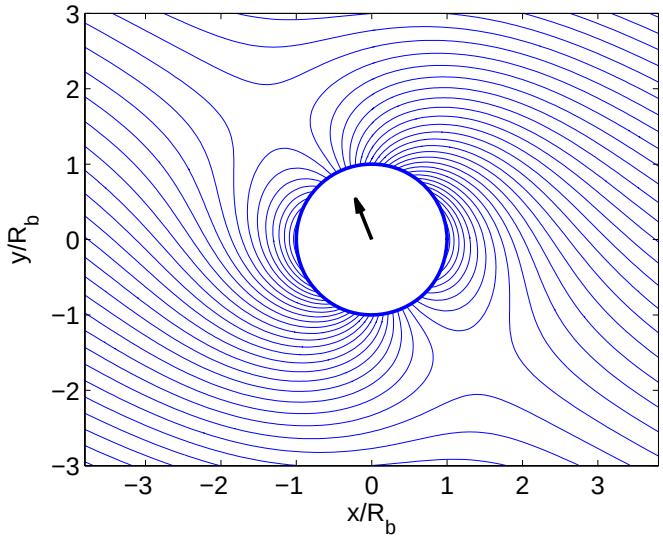

Figure 2.8: Gas streamlines according to equation (2.11) for a fast bubble with $U_b = 0.58\,m/s$, $u_{mf} = 0.446$ and $\alpha = 21.8\,deg$.

Combining equations (2.8)-(2.10) the following expression is obtained

$$\psi_g = (U_b \cos(\alpha) - u_0) \cdot r \sin(\theta) \cdot \left[1 - \frac{A^2}{r^2}\right] + U_b \sin(\alpha) \cdot r \cos(\theta) \cdot \left[1 - \frac{R_b^2}{r^2}\right] \quad (2.11)$$

where $A^2 = \frac{U_b \cos(\alpha)+u_0}{U_b \cos(\alpha)-u_0} R_b^2$ and the radial and tangential gas velocities can be obtained as follows

$$\begin{aligned} u_r &= \frac{-1}{r}\frac{\partial \psi_g}{\theta} = \\ &= \cos(\theta) \cdot \left(U_b \frac{\cos(\theta+\alpha)}{\cos(\theta)} + u_0\right) \cdot \left[\frac{R_b^2}{r^2} - \frac{U_b \cos(\theta+\alpha) - u_0 \cos(\theta)}{U_b \cos(\theta+\alpha) + u_0 \cos(\theta)}\right] \quad (2.12) \\ u_\theta &= \frac{\partial \psi_g}{r} = \\ &= \sin(\theta) \cdot \left(U_b \frac{\sin(\theta+\alpha)}{\sin(\theta)} + u_0\right) \cdot \left[\frac{R_b^2}{r^2} + \frac{U_b \sin(\theta+\alpha) - u_0 \sin(\theta)}{U_b \sin(\theta+\alpha) + u_0 \sin(\theta)}\right] \quad (2.13) \end{aligned}$$

The first term of the right side of equation (2.11) represents the streamlines due to the vertical component of the bubble velocity and has the same form as the original Davidson's equation changing U_b by $U_b \cos(\alpha)$. The second term represents the irrotational flow of particles around a circular bubble moving with an horizontal velocity $U_b \sin(\alpha)$. Note that equations (2.11), (2.12) and (2.13) recover the original Davidson's expressions for $\alpha = 0$. Figure 2.8 shows the streamlines obtained from the stream function (2.11) for a circular bubble with a velocity equal to the velocity of the bubble showed in figure 2.7. A qualitative agreement between the simple case of a circular bubble with the one showed in figure 2.7(d) is observed: two recirculation region at

both sides of the bubble but also part of the gas that traverses and leaves the fast bubble.

However, not only the direction of the bubble velocity affects the gas velocity field but also the bubble geometry significantly influences the gas flow. This can be seen in figure 2.7, where higher velocities are obtained in the left-bottom zone of the bubble because of the favorable path created by the bubble geometry in that region. This fact can not be observed in a circular bubble. Thus, the throughflow crossing the bubble is also influenced by the bubble geometry.

2.6 Erupting and interacting bubbles

Previous studies about erupting bubbles can be found in the literature focused either on the particle ejection velocity (Santana et al., 2005; Almendros-Ibáñez et al., 2006; Müller et al., 2007) or on the dome evolution and the gas flow through the bubble (Glicksman and Yule, 1986, 1995; Levy et al., 1988; Gera and Gautam, 1994). Although the particle velocity field was measured experimentally in bubbling beds using PIV, the few studies available about the throughflow in erupting bubbles are limited to isolated circular bubbles or artificial cavities at the bed surface rather than in real geometries.

Figure 2.9 shows the evolution of the velocity field and the streamlines viewed by an stationary observer for one bubble eruption at the bed surface. At $t = 0$ the bubble is approximating to the bed surface forming the typical dome. At $t = 40\,ms$ the dome breaks at a certain point due to the irregularities which appear in the dome (Müller et al., 2007) when its thickness decreases and the stalactites funnel the particles situated in the external surface of the dome. In this instant, most of the throughflow leaves the bubble through the small aperture opened at the breaking dome. The magnitude of the gas velocity is very high in this region and the rest of the dome decelerates because the gas that was dragging it, is drastically diminished and dome particles are moving only because of their inertia. Finally, at $t = 68\,ms$ the dome collapses and the gas velocity decreases due to the higher section opened for the gas flow at the dome aperture.

In addition, during the dome evolution showed in figure 2.9 a small bubble is observed at the bottom-right region of the pictures. This bubble seems to follow the path opened by the leading one due to the more favorable pressure gradient, although they do not coalescence before the leading bubble breaks the bed surface.

Figure 2.10 shows the evolution of an erupting bubble while another bubble is coalescing bellow the leading one. At $t = 0$ the bubble is isolated and it aproximantes, ascending vertically, to the bed surface with a velocity $U_b > u_{mf}$, as it is deduced from the gas recirculation vortexes at both sides of the bubble observed in figure 2.10(d),

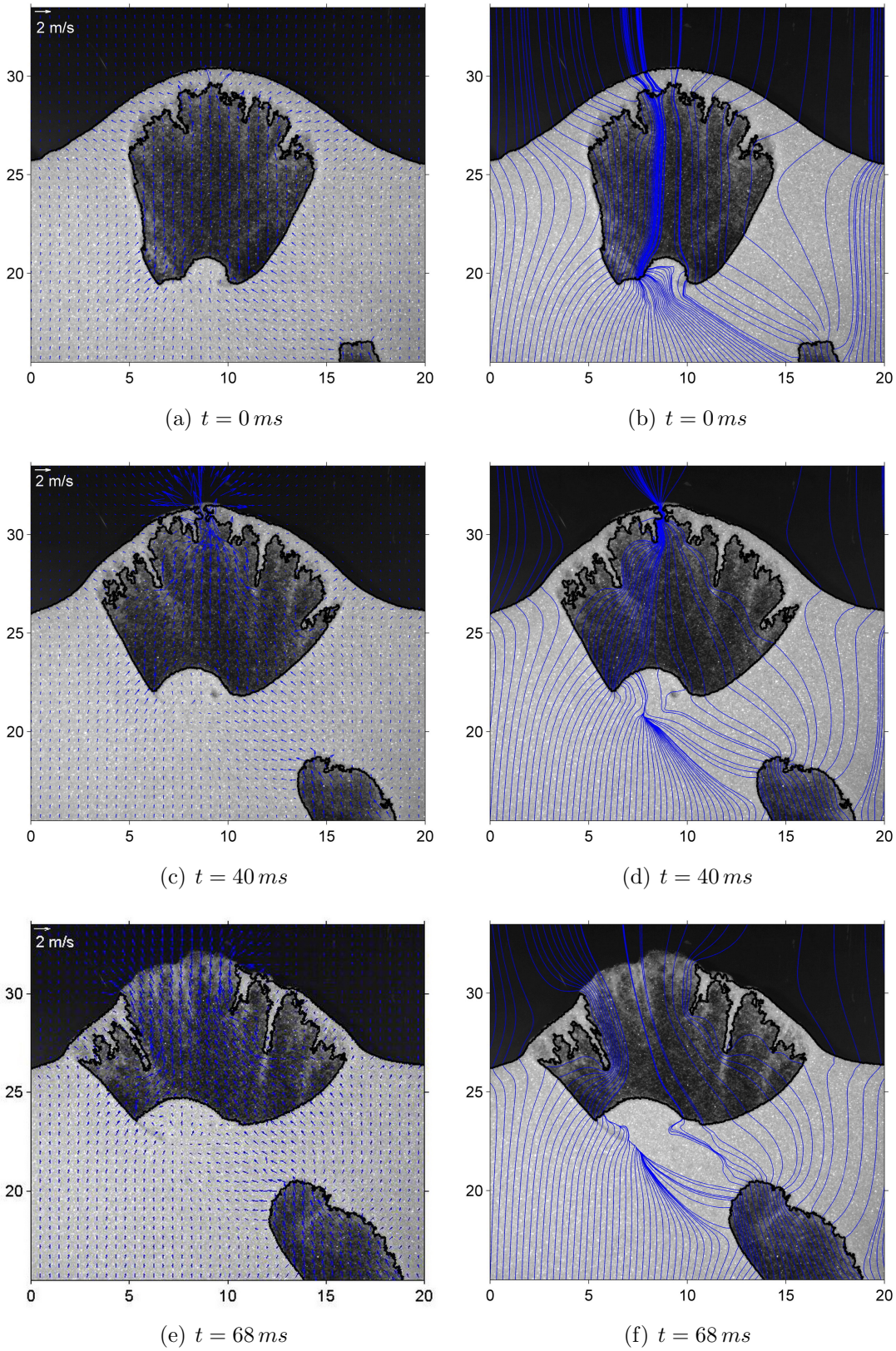

(a) $t = 0\,ms$ (b) $t = 0\,ms$

(c) $t = 40\,ms$ (d) $t = 40\,ms$

(e) $t = 68\,ms$ (f) $t = 68\,ms$

Figure 2.9: Gas velocity vectors $\boldsymbol{u}$ and streamlines for an erupting bubble viewed by a stationary observer. Scale in cm.

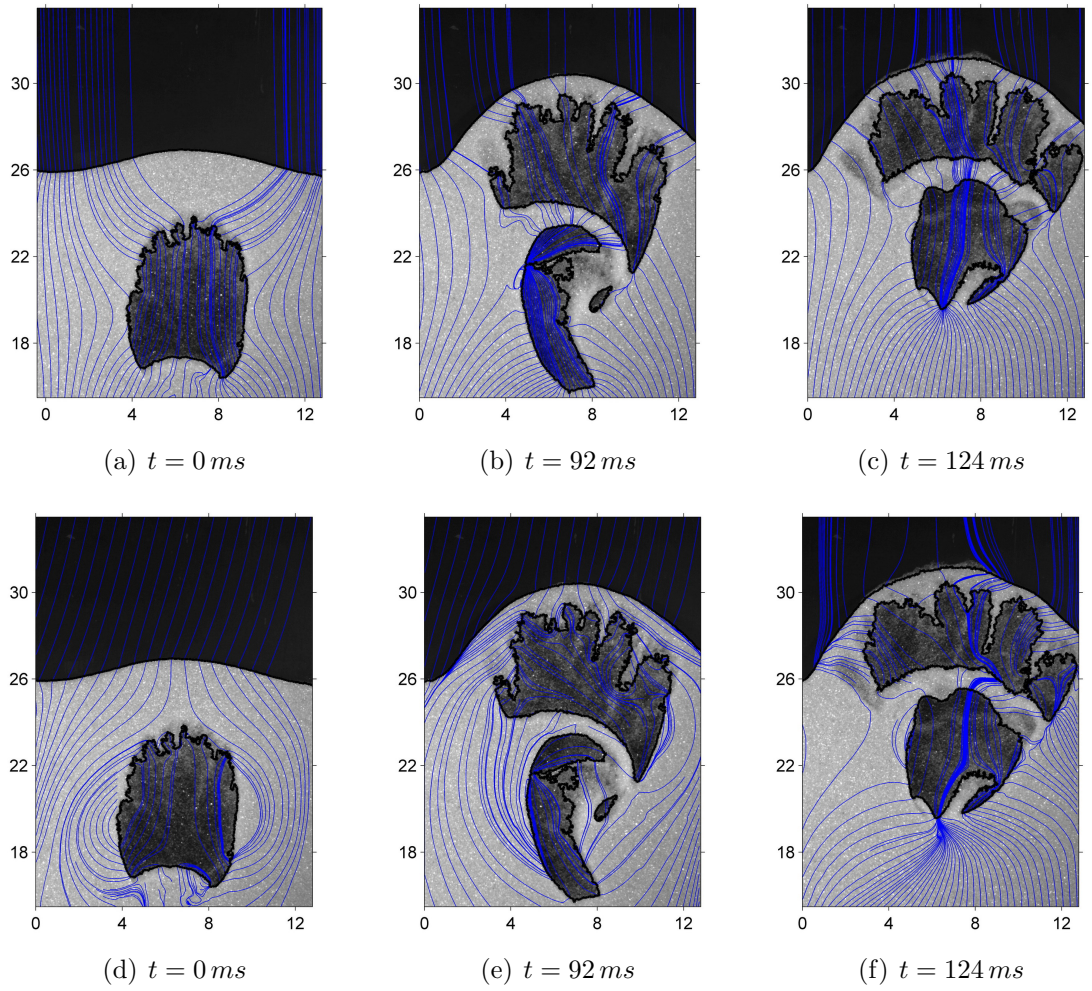

(a) $t = 0\,ms$ (b) $t = 92\,ms$ (c) $t = 124\,ms$

(d) $t = 0\,ms$ (e) $t = 92\,ms$ (f) $t = 124\,ms$

Figure 2.10: (a), (b) and (c) streamlines viewed by a stationary observer and (d), (e) and (f) streamlines viewed by an observer moving with the leading bubble. Scale in *cm*.

which are typical of fast bubbles. At $t = 92\,ms$ the leading bubble continues ascending through the bed with a velocity $U_b > u_{mf}$, but now another elongated bubble is approximating to the leading bubble. The more favorable pressure gradient through the path opened by the first bubble provokes an acceleration in the trailing bubble, which reaches a higher velocity. In this situation, a single gas cloud encompassing both bubbles can be seen, in agreement with the flow patterns of gas around a pair of bubbles aligned vertically observed by Shichi et al. (1968) (also reproduced in the first edition of the book by Kunii and Levenspiel (1969)). In addition, the peculiar geometry of both bubbles provoques additional smaller gas recirculations in the right side of both bubbles. Finally, at $t = 124\,ms$ the leading bubble decelerates and becomes a slow bubble ($U_b < u_{mf}$). The gas recirculations disappear and the roof of the bubble crumbles because of the rain of particles from the bubble roof in form of stalactites. In this situation, the first bubble acts as a preferential path for the gas flow near the

bubble. The gas reaches the freeboard from deep regions of the bed traversing both bubbles because of their lower resistance to the gas path.

The sequence of pictures of figure 2.10 also shows the change in the geometry of both bubbles. The leading bubble, initially slightly elongated becomes to grow and to expand in the horizontal direction as it breaks the bed surface. This bubble corresponds to the *collapsed dome bubbles* observed by Almendros-Ibáñez et al. (2006). This kind of bubbles is characterized by a very low bubble velocity and non-projected dome particles at eruption; rather, dome particles rain off and return to the dense phase.

The trailing bubble, which coalesces bellow the leading one, also changes its geometry: it initially elongates due to the acceleration during the approximation to the wake of the leading bubble. This picture is typical of coalescing bubbles. Later on, as the bubble decelerates, its geometry changes to an approximately round bubble, due to the increase of the wake section of the leading bubble.

2.7 Discussion and conclusions

Combination of PIV technique and FEM for studying the particle velocity field represents an easy and fast tool to determine the flow patterns of both particles and gas in real and more complex geometries in which analytical solutions are not possible. One of the main advantages of this method is the very low computational cost. The calculation time of $\boldsymbol{u}$ and p_f with the finite element program and $\boldsymbol{v}$ with PIV for any of the frames shown in this article is very low (around 3-4 minutes in a regular desktop computer) compared with the calculation times needed by CFD methods in much more powerful computers.

Although in this work a bubbling fluidized bed at low superficial gas velocities has been used, this experimental-numerical method is not restricted to these experimental conditions. The method could be used for higher gas velocities if the possible bed expansion and thereby the increase in the voidage ϵ is taken into account. Instead of Ergun's equation, whose validity is restricted to voidage values close to ϵ_{mf}, a different equation should be used. As an example the equation proposed by Gibilaro et al. (1985) which agrees with Ergun's equation at $\epsilon \approx \epsilon_{mf}$, but, in addition, predicts properly the pressure drop for higher void fractions where Ergun's equation is not valid.

In the present work, the equations of the classical model for the relative motion between fluid and particles proposed by Davidson in 1961 have been solved for the first time for real bubble geometries and particle velocities captured from a freely bubbling fluidized bed. Up to present, the Davidson's model has only been solved for bubbles with ideal geometries (i.e. circular, elliptical or kidney shape) with a strictly vertical

rising velocity.

Valenzuela and Glicksman (1985), in their work based on Davidson's model, computed the throughflow crossing bubbles for an array of spherical bubbles distributed in a bed. They showed that, if the porosity in the emulsion phase remains at the value corresponding to minimum fluidization conditions, all excess gas over U_{mf} which is not visible in form of bubbles traverses the bed as throughflow crossing the bubbles. They also concluded that the throughflow is not dependent on the bubble rise velocity or particle velocities but on the bubble shape and bubble distribution. Here, the instantaneous throughflow for each frame (rather than the mean time throughflow, which is the data usually presented in literature (Grace and Clift, 1974; Johnsson et al., 1991)) is computed for real bubble geometries. In agreement with Valenzuela and Glicksman (1985), bubble geometry is shown to play an important role in the throughflow, specially in the corners of the bubble contour (see figure 2.7(c)) where high gas velocities are observed.

The main features predicted by the original Davidson's model in circular bubbles are also observed in a real geometry. Among them is the different behavior observed depending on the ratio U_b/u_0: when $U_b/u_0 < 1$ the bubble is slow and most of the gas traverses it although two small regions appear at both sides of the bubble where the gas is dragged down by the particles and re-enters into the bubble (see figure 2.6(d)). On the other hand, when the bubble is fast ($U_b/u_0 > 1$) the gas leaving the roof of the bubble returns again to the bubble through its bottom without being in contact with the main stream. Moreover, when the bubble velocity has an appreciable horizontal component some of the gas traverses the gas from its bottom to its roof returning to the main stream. This fact can be observed in figure 2.7(d) and has been corroborated including and inclination angle α in the stream function of the particles ψ_p. The results of the original equations, including the horizontal component of the bubble velocity, agrees qualitatively with the numerical results.

Also the bubble eruption at the bed surface and the interaction between bubbles have been analysed by the same numerical scheme. The streamlines in figure 2.9(d) show how almost all throughflow leaves the bubble through the region where the dome is broken (although gas flow through the dome, whose porosity is assumed to remain at ϵ_{mf}, is allowed in the modeling).

Results for interacting bubbles show how a single cloud can encompass two coalescing bubbles.

In summary, the equations of Davidson's model (equations (2.1)-(2.3)) have been solved in a 2-D freely bubbling fluidized bed using a finite element solver program fed with experimental data from PIV measurements and a high speed video-camera. The

method, valid in a wide range of operating conditions, has a low computational cost and permits the prediction of gas streamlines in slow, fast, erupting and interacting bubbles with real geometries. In addition, the effect of non-vertical ascend of the bubble on gas streamlines has been studied by including an horizontal component to the bubble velocity in the original Davidson's equations. Finally, the finite element program permits easily to include a quadratic term into gas momentum equation, as it is shown in chapter 3.

2.8 Notation

d_p Particle diameter $[m]$

k Permeability of the medium $[m^2]$

p_f Fluid pressure $[Pa]$

R_b Bubble radius $[m]$

R_p Radius of the percolation circle around bubbles, defined by equation (2.7) $[m]$

r Radial coordinate

U Superficial gas velocity $[m/s]$

U_0 Superficial gas velocity in a uniform bed without bubbles $[m/s]$

$\boldsymbol{u}$ Interstitial gas velocity $[m/s]$

u_0 Interstitial gas velocity at minimum fluidization conditions $[m/s]$

$\boldsymbol{u_r}$ Radial gas velocity $[m/s]$

$\boldsymbol{u_\theta}$ Tangential gas velocity $[m/s]$

$\tilde{\boldsymbol{u}}$ Relative gas velocity defined in equation (2.3) $[m/s]$

$\boldsymbol{v}$ Particle velocity $[m/s]$

x Horizontal coordinate

y Vertical coordinate

α Angle formed by the bubble velocity and the vertical $[rad]$

ϵ Void fraction $[-]$

ϵ_{mf} Void fraction at minimum fluidization conditions $[-]$

θ Tangential coordinate

μ Fluid dynamic viscosity $[Pa \cdot s]$

ρ_f Fluid density $[kg/m^3]$

ρ_p Particle density $[kg/m^3]$

ψ_g Gas stream function

ψ_p Particle stream function

$(\,)_b$ Bubble phase or region free of particles

$(\,)_e$ Emulsion phase

Bibliography

Almendros-Ibáñez J.A., Sobrino C., de Vega M. and Santana D., 2006. A new model for ejected particle velocity from erupting bubbles in 2-D fluidized beds. *Chemical Engineering Science*, vol. 61, pp. 5981-5990

Clift R., Grace J.R., Cheung L. and Do T.H., 1972. Gas and solids motion around deformed and interacting bubbles in fluidized beds. *Journal of Fluid Mechanics*, vol. 51, pp. 187-205

Collins R., 1965. An extension of Davidson's theory of bubbles in fluidized beds. *Chemical Engineering Science*, vol. 20, pp. 747-755

Croxford A.J., 2006. Investigation of dynamics and control of fluidised beds using pressure measurements. PhD thesis, University of Bristol

Davidson J.F., 1961. Symposium on fluidisation-Discussion. *Transactions of the Institution of Chemical Engineers*, vol. 39, pp. 230-232

Davidson J.F. and Harrison D., 1963. *Fluidised particles*. Cambridge University Press

Ergun S., 1952. Fluid flow through packed columns. *Chemical Engineering Progress*, vol. 48, pp. 89-94

Geldart D., 1973. Types of gas fluidization, *Powder Technology*, vol. 7, pp. 285-292

Gera D. and Gautam M., 1994. Variation of throughflow velocity in a 2-D rising bubble. *Powder Technology*, vol. 79, pp. 257-263

Gibilaro L.G., Di Felice R., Waldran S.P. and Foscolo P.U., 1985. Generalized friction factor and drag coefficient correlations for fluid-particle interactions. *Chemical Engineering Science*, vol. 40, pp. 1817-1823.

Glicksman L.R. and Yule T., 1986. Gas throughflow in a bubbling fluidized beds, in K. Ostergaard, A. Sorensen (Eds.) *Fluidization V: Proceedings of the Engineering Foundation Conference*, Amer. Inst. of Chemical Engineers, Elsinore (Denmark), pp. 103-110

Glicksman L.R. and Yule T., 1995. Prediction of the particle flow conditions in the freeboard of a freely bubbling fluidized bed. *Chemical Engineering Science*, vol. 50, pp. 69-79

Grace J.R. and Clift R., 1974. On the two-phase theory of fluidization. *Chemical Engineering Science*, vol. 29, pp. 327-334

Hatano H. and Ishida M., 1982. Study on the cloud radius and interphase mass transfer coefficient for a gas-solid fluidized bed. *Kagaku Kogaku Ronbunshu*, vol. 10, pp. 184-191

Jackson J.R., 1963. The mechanics of fluidised beds: Part I: The stability of the state of uniform fluidisation. *Transactions of the Institution of Chemical Engineers*, vol. 41, pp. 13-21

Jackson J.R., 1963. The mechanics of fluidised beds: Part II: The motion of fully developed bubbles. *Transactions of the Institution of Chemical Engineers*, vol. 41, pp. 22-28

Jackson J.R., 2000. *The dynamic of fluidized particles*. Cambridge University Press

Johnsson F., Andersson S. and Leckner B., 1991. Expansion of a freely bubbling fluidized bed. *Powder Technology*, vol. 68, pp. 117-123

Johnsson F., Zijerveld R.C., Schouten J.C., van den Bleek C.M. and Leckner B., 2000. Characterization of fuidization regimes by time-series analysis of pressure fuctuations. *International Journal of Multiphase Flow*, vol. 26, pp. 663-715

Kunii D. and Levenspiel O., 1969. *Fluidization Engineering*. John Wiley & Sons

Kunii D. and Levenspiel O., 1991. *Fluidization Engineering*. Butterworth-Heinemann

Levy E.K., Chen H.K., Radcliff R. and Caram H.S., 1988. Analysis of gas flow through erupting bubbles in a gas-fluidized bed. *Powder Technology*, vol. 54, pp. 45-57

Lignola P.G., Donsi G. and Massimilla L., 1983. Mass spectrometric measurements of gas composition profiles associated with bubbles in a two dimensional bed. *AIChE Symposium Series*, vol. 79, pp. 19-25

Littman H. and Homolka G.A.J., 1973. The pressure field around a two-dimensinal gas bubble in a fluidized bed. *Chemical Engineering Science*, vol. 28, pp. 2231-2243

Müller C.R., Davidson J.F., Dennis J.S. and Hayhurst A.L., 2007. A study of the motion and eruption of a bubble at the surface of a two-dimensional fluidized bed using particle image velocimetry (PIV), *Industrial & Engineering Chemistry Research*, vol. 46, pp. 1642-1652

Murray J.D., 1965. On the mathematics of fluidization. Part 1. Fundamental equations and wave propagation. *Journal of Fluid Mechanics*, vol. 21, pp. 465-493

Murray J.D., 1965. On the mathematics of fluidization. Part 2. Steady motion of fully developed bubbles. *Journal of Fluid Mechanics*, vol. 22, pp. 57-80

Otsu N., 1979. A threshold selection method from gray-level histograms, *IEEE Transactions on Systems Man and Cybernetics*, vol. 9, pp. 62-66

Pallarès D. and Johnsson F., 2006. A novel technique for particle tracking in cold 2-dimensional fluidized beds-simulating fuel dispersion. *Chemical Engineering Science*, vol. 61, pp. 2710-2720

Raso G.G., Volpicelli G. and Maitz C., 1965. Sul movimento do bolle di gas in letti di particelle fluidizzati in colonne rettangolari. *Quaderni dell'ingegnere chimico italiano*, vol. 1, pp. 157-167

Santana D., Nauri S., Acosta A., García N. and Macías-Machín A., 2005. Initial particle velocity spatial distribution from 2-D erupting bubbles in fluidized beds. *Powder Technology*, vol. 150, pp. 1-8

Shichi R., Mori S. and Muchi I., 1968. Interaction between two bubbles in gaseous fluidization. *Kagaku Kogaku*, vol. 32, pp. 343-348

Stewart P.S.B., 1968. Isolated bubbles in fluidized beds - theory and experiment. *Transactions of the Institution of Chemical Engineers*, vol. 46, pp. 60-66

Sveen J.P., http://www.math.uio.no/∼jks/matpiv (Last modified in August, 2004. Accesed in 2008)

Toomey R.D. and Johnstone H.F., 1952. Gaseous fluidization of solid particles. *Chemical Engineering Progress*, vol. 48, pp. 220-226

Valenzuela J.A. and Glicksman L.R., 1985. Gas flow distribution in a bubbling fluidized bed. *Powder Technology*, vol. 44, pp. 103-113

van Wachem B.G.M. and Almstedt A.E., 2003. Methods for multiphase computational fluid dynamics. *Chemical Engineering Journal*, vol. 96, pp. 81-98

Chapter 3

Non-Darcy effects in fluidized beds

Contents

3.1 Abstract

In chapter 2, a novel experimental-numerical method combining PIV and FEM was developed for solving gas and particle motion in a real geometry captured from a freely bubbling fluidized bed, based on the equations of Davidson's model. This model of particle and gas motion around bubbles in fluidized beds have been extended in order to take into account non-Darcy effects. Davidson neglected inertial effects due to he assumed that gas velocity follows the well known Darcy's law for porous media. In this work, Darcy's equation has been replaced by Ergun's equation which includes both, the viscous or Darcy term and the inertial or Forchheimer term. The resulting governing equations have been solved numerically using a finite element program.

Two different approaches have been carried out. Firstly, the simplest case of one isolated circular or spherical bubble has been analysed, showing a small decrease (5%

for a maximum Reynolds number of $Re_{mf} \sim 10^2$) in the cloud size around fast bubbles assuming that the particle velocity field is irrotational. Secondly, the more realistic bubble geometry captured with a high speed video-camera have been studied. In this case, the assumption on particle flow have been avoided through the use of the actual particle velocity field. This field was obtained using Particle Image Velocimetry (PIV).

The gas velocity field including non-Darcy effects has been compared with the field obtained with the original Davidson's equations, which were explained in more detail in chapter 2, concluding that gas velocity magnitude decreases as Reynolds number increases. Nevertheless, in both cases the differences observed are small and the original Davidson's model can predicts qualitative the gas flow pattern around bubbles in fluidized beds.

3.2 Introduction

Davidson's model (Davidson, 1961; Davidson and Harrison, 1963) was the first and simplest try to model the flow of both, gas and particles, around one isolated steady state ascending bubble in a fluidized bed. This important breakthrough was *"...the seminal concept that guided research and advanced understanding of dense bubbling fluidized beds..."* (Kunii and Levenspiel, 1991), which, in spite of its simplicity, predicts properly the gas and particles movement and pressure distribution around rising bubbles.

Davidson's original idea assumed both streams as incompresible fluids and the porosity ϵ, defined as the ratio between the bed volume filled with gas and the total volume of the bed, constant everywhere outside the bubble and equal to that one at minimum fluidization conditions ϵ_{mf}. In addition, Davidson assumed that the relative velocity between gas and particles streams are proportional to the gas pressure gradient in agrement with the well known Darcy's law for porous media. With these assumptions, the governing equation of Davidson's model are:

$$\nabla \cdot \boldsymbol{u} = 0 \tag{3.1}$$

$$\nabla \cdot \boldsymbol{v} = 0 \tag{3.2}$$

$$\tilde{\boldsymbol{u}} = \boldsymbol{u} - \boldsymbol{v} = -\frac{k}{\mu}\nabla p_f \tag{3.3}$$

where $\boldsymbol{u}$ and $\boldsymbol{v}$ are respectively the gas velocity and the particle velocity, μ is the gas viscosity, p_f is the fluid pressure and k is the permeability of the porous media, which depends on the size and on the sphericity of the particle and on the porosity.

The equation system (3.1)-(3.3) provides (in the 2-D case) four equations in order

to obtain five unknowns (u_x, u_y, v_x, v_y and p_f). The additional necessary equation to solve the problem is obtained assuming that the particle flow around the circular bubble is irrotational. Therefore, neglecting wall effects, $\boldsymbol{v}$ can be obtained from the equations of the potential flow theory.

In chapter 2, using a finite element program together with the PIV technique, the set of equations (3.1)-(3.3) were solved in real geometries captured from a freely bubbling fluidized bed. Non-interacting slow and fast bubbles and also erupting and interacting bubbles were analysed and qualitative agreement was observed with the original Davidson's results, despite the differences in the bubble geometries.

Numerous studies about the flow through porous media and packed beds have demonstrated that Darcy's law is valid only in the creeping flow regimen, i.e. when the Reynolds number is small. For example, Dybbs and Edwards (1984) made an extensive experimental work using laser anemometry and flow visualization for a wide range of Reynolds numbers. They concluded that four different flow regimes can be found in a porous media, depending on the Reynolds number:

1. creeping or Darcy flow regime at $Re_{pore} < 1 - 10$
2. inertial flow regime at $1 - 10 \leq Re_{pore} \leq 150$
3. unsteady laminar flow regime at $150 \leq Re_{pore} \leq 300$ and
4. fully turbulent flow at $Re_{pore} > 300$

where the Reynolds number is based on the pore characteristic length d_{pore}, as:

$$Re_{pore} = \frac{\rho_f \, U \, d_{pore}}{\mu} \tag{3.4}$$

The linear relationship between pressure gradient and fluid velocity disappears progressively as Reynolds number increases over values of $Re_{pore} = 1 - 10$, although the fully turbulent flow is not observed until Reynolds number is one order of magnitude higher (Bear, 1972).

The use of the Re_{pore} as a criteria for non-Darcy flow fails in the difficulty of obtain the pore characteristic length d_{pore} for most porous media, specially for packed beds of non-uniform particle size distribution. That is the reason why other researchers prefer to use the Forchheimer number, defined as

$$Fo = \frac{k \, \beta \, \rho \, U}{\mu} \tag{3.5}$$

where β is the non-Darcy coefficient defined by

$$-\nabla p_f = \frac{\mu}{k} U + \beta \rho U^2 \tag{3.6}$$

as a criteria for non-Darcy effects.

Zenz and Grigg (2006) made a complete review of the criteria for non-Darcy flow in porous media. According to them, the limit value of the Reynolds number criteria varies from 1 to 100, depending on the Reynolds number definition and the author, and for the Forchheimer number criteria the maximum value ranges from 0.005 to 0.2, depending on the source. They suggested that the Forchheimer number is a more appropriated criteria because of the uncertainty in choosing the characteristic length in the Reynolds number and they proposed a limit value of 0.11, which corresponds to a 10% of non-Darcy effects.

Nevertheless, for a fixed bed the well known Ergun's equation (Ergun, 1952) predicts properly the pressure gradient across a bed for a wide range of Reynolds number if the porosity not depart so much from the one at minimum fluidization conditions (Bird et al., 2002). Ergun's equation included both, the viscous and the inertial term:

$$\frac{\Delta p_f}{L} = 150 \cdot \frac{(1-\epsilon_{mf})^2}{\epsilon_{mf}^3} \cdot \frac{\mu U}{(\phi d_p)^2} + 1.75 \cdot \frac{1-\epsilon_{mf}}{\epsilon_{mf}^3} \cdot \frac{\rho_f U^2}{\phi d_p} \tag{3.7}$$

where U is the superficial gas velocity ($U = \tilde{u} \cdot \epsilon$) and ϕ the particle sphericity.

In this work, the original Davidson's idea that the relative velocity $\tilde{u}$ follow the Darcy's law for porous media have been extended including a quadratic term for taking into account non-Darcy effects using the Ergun's equation, also known as the Darcy-Forchheimer equation in the porous media literature (Liu and Masliyah, 1996). The influence of the Forchheimer term in the simplest circular or spherical isolated bubble, and also, its effect in real geometries captured from experiments carried out in a 2-D freely bubbling fluidized bed have been studied.

In the next point, the Darcy's law extension and how it has been solved using a finite element program (Comsol Multiphysics v.3.2) will be explained. Thereafter, the influence of non-Darcy effects on the results obtained from the original Davidson's model for a wide range of particle sizes and densities will be studied. Then, the work presented in chapter 2 will be continued and extended comparing both Davidson's model and the new extended model including the quadratic term, in a real geometry. Finally, the main conclusions of the work will be discussed and summarized.

3.3 Davidson's model extension including non-Darcy effects

Original Ergun's expression (equation (3.7)) combines a linear term (Carman-Kozeny term), which predicts properly the pressure drop when the viscous forces dominate, and a quadratic term (Forchheimer term), which is valid when the inertial forces are more important than the viscous ones. It is generally accepted, and has been also experimentally demonstrated, that the sum of both terms predicts properly the pressure drop when both forces are of the same order of magnitude, i.e., at intermediate Reynolds numbers (Bird et al., 2002).

Equation (3.7) can be rearranged and nondimensionalized according to

$$\left(\frac{\Delta p_f}{L}\right)^* = \frac{85.714}{Re} + 1 = \frac{1}{Fo} + 1 \tag{3.8}$$

where

$$\left(\frac{\Delta p_f}{L}\right)^* = \frac{\Delta P}{L} \cdot \frac{\epsilon_{mf}^3 \, d_p \, \phi}{1.75 \, (1 - \epsilon_{mf}) \, \rho_f \, U^2} \tag{3.9}$$

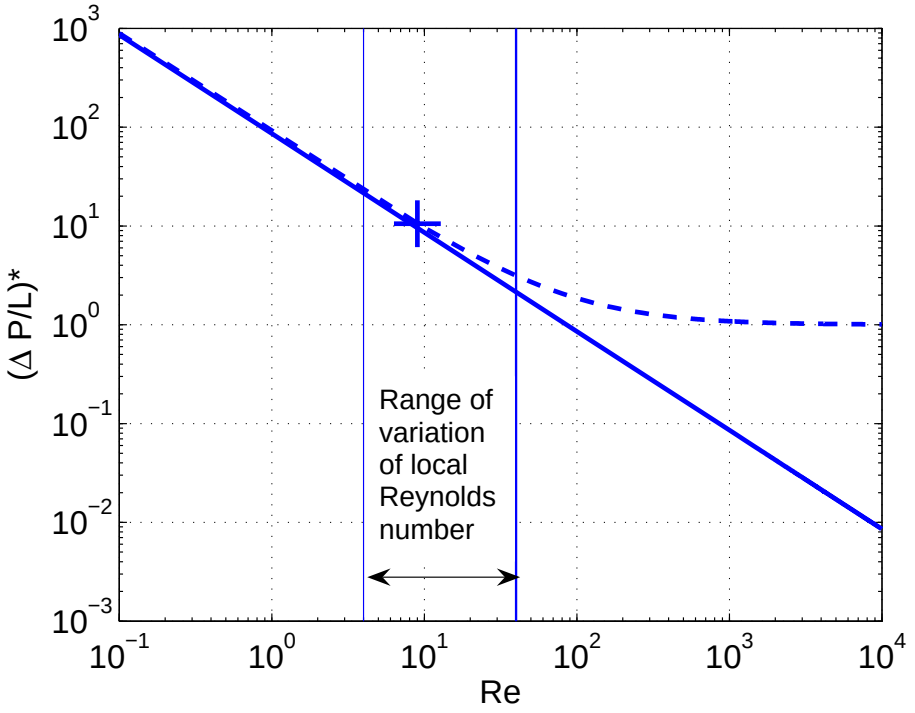

Figure 3.1: Graphical representation of the nondimensionalized Ergun's equation. Dashed line represents equation (3.8) and solid line only the lineal term of equation (3.8). The cross represents the operating conditions at minimum fluidization conditions and the vertical lines indicate the range of variation of the local Reynolds number for the experimental conditions of this work.

is a non-dimensional pressure gradient and the Reynolds number is defined by

$$Re = \frac{\rho_f \, U \, \frac{\phi \, d_p}{\left(1-\epsilon_{mf}\right)}}{\mu} \tag{3.10}$$

Equation (3.8) is plotted in figure 3.1, which shows that approximately around $Re \sim 1 - 10$ Ergun's equation departs from the lineal relation proposed by Darcy's law. For $Re \geq 10^4$ the value of $\left(\frac{\Delta p_f}{L}\right)^*$ is constant and independent of the Reynolds number. In this figure, the cross indicates the Reynolds number obtained at minimum fluidization conditions: $Re_{mf} = 9$. Nevertheless, this is a mean value and the gas velocity can vary notably in the vicinity of the bubbles. For the experimental conditions of this work, the local Reynolds number ranges between $Re_{min} \approx 4$ and $Re_{max} \approx 40$. In regions of higher Reynolds number the influence of non-Darcy effects will be significant.

In order to take into account non-Darcy deviations, Ergun's equation can be used instead of Darcy's law. In this way, the magnitude of the pressure gradient can be obtained from the following equation

$$|\nabla p_f| = B \, \tilde{u} + A \, \tilde{u}^2 \tag{3.11}$$

where $A = 1.75 \frac{\rho_f}{d_p \, \phi} \frac{\left(1-\epsilon_{mf}\right)}{\epsilon_{mf}}$ and $B = 150 \frac{\mu}{d_p^2 \, \phi^2} \frac{\left(1-\epsilon_{mf}\right)^2}{\epsilon_{mf}^2}$ are constants obtained from equation (3.7). The magnitude of the relative gas velocity can be obtained from (3.11) as follows

$$\tilde{u} = \frac{-B + \sqrt{B^2 + 4 \, A \, |\nabla p_f|}}{2 \, A} \tag{3.12}$$

and its components are proportional to the pressure gradient in each direction according to

$$\tilde{u}_x = \tilde{u} \cdot \frac{-\frac{\partial p_f}{\partial x}}{|\nabla p_f|}; \quad \tilde{u}_y = \tilde{u} \cdot \frac{-\frac{\partial p_f}{\partial y}}{|\nabla p_f|} \tag{3.13}$$

3.4 Non-Darcy effects on original Davidson's model

In order to take into account inertial effects, the original Darcy's law in Davidson's model has been replaced by equation (3.11). The set of resultant equations has been solved using a finite element program (Comsol Multiphysics v. 3.2), modifying the equations of the Darcy's law submodule in the Chemical Engineering module of the program.

In chapter 2, the original Davidson's equations were solved numerically with success, in combination with the PIV technique, in a geometry captured from a freely

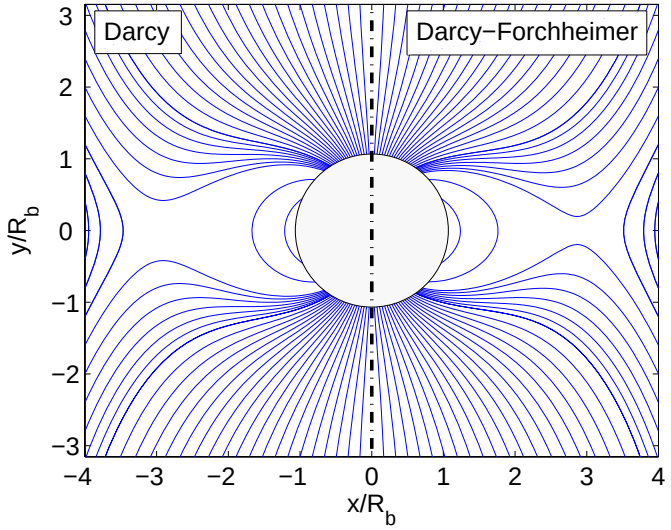

(a) $U_b/u_{mf} = 0.8$

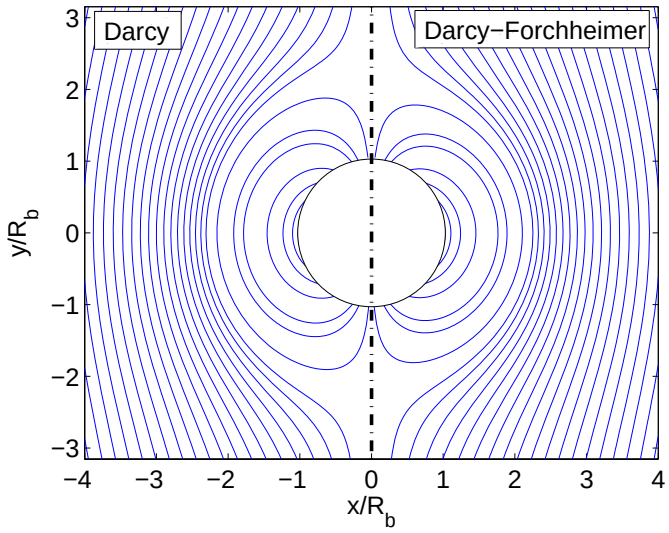

(b) $U_b/u_{mf} = 1.5$

Figure 3.2: (a) Slow bubble with $U_b/u_{mf} = 0.8$ and (b) fast bubble with $U_b/u_{mf} = 1.5$. In both cases U_{mf} has been calculated for $\rho_p = 2500\frac{kg}{m^3}$ and $d_p = 700\,\mu m$, which results in $Re_{mf} \simeq 40$.

bubbling fluidized bed. In addition, the numerical analysis agreed with the theoretical expressions developed by Davidson's using the potential flow theory for the simplest case of a circular bubble. In order to study how the non-Darcy effects modify the original Davidson's results, this simplest case of a circular or spherical bubble will be studied firstly.

The computational domain was assumed symmetrical respect to the vertical axis $x = 0$. Half of a bubble of $R_b = 1$ was situated at $x = y = 0$. In order to avoid the influence of the boundary conditions, the domain contours had to be situated far away

from the bubble. Finally, all the boundaries were placed 50 diameters away from the center of the bubble. A uniform flow equal to U_{mf} was imposed as boundary condition at the bottom of the bed and constant pressure at the top. The boundary condition for the lateral limit was no-penetration. Nevertheless, this boundary condition does not affect the flow around the bubble, as it is situated 50 bubbles diameters away from it.

Figure 3.2 shows a comparative results between the streamlines obtained with the original 2-D Davidson's model, represented in the left side of each figure, and the ones obtained with the extended model including the Forchheimer term, in the right side, for (a) a slow bubble and (b) a fast bubble. In both cases $Re_{mf} \simeq 40$ and no appreciable differences between both cases are observed. Only a small decrease in the radius of the recirculation cloud around the bubble can be observed in the fast bubble case. As constant flow boundary condition is imposed in both cases, the are no noticeable differences on the gas velocity magnitude. In contrast, the pressure gradient necessary for that flow increases with Reynolds number according to

$$\frac{|\nabla p_f|_{D-F}}{|\nabla p_f|_D} = 1 + \frac{1.75}{150} Re_{mf} \tag{3.14}$$

Thus, for a Reynolds number of $Re_{mf} \simeq 85$ the pressure gradient is double the pressure gradient neglecting inertial forces, for the same gas flow.

In order to study how the size of the gas recirculation decreases with the Reynolds number, a range of Reynolds numbers usually found in typical fluidized bed applications was swept. U_{mf} was calculated according to Kunii and Levenspiel (1991) for different particles diameters, ranging from $100\mu m$ to $1000\mu m$ and for different particle densities varying from $1000\frac{kg}{m^3}$ to $3000\frac{kg}{m^3}$. The range of Reynolds number resulting varies from 10^{-3} to 10^2. Table 3.1 shows the numerical values of U_{mf} and Re_{mf} obtained for each combination of particle size and density.

Figures 3.3(a) and 3.3(b) show that the size of the gas recirculation region of fast bubbles decreases when the Reynolds number increases. The data of table 3.1 are plotted versus Re_{mf}, for a constant value of U_b/u_{mf} and all the points fit in with the same line. When U_b/u_{mf} increases, the ratio R_{D-F}/R_D approximates to 1 because both radius, R_{D-F} and R_D tend asymptotically to the same value: the bubble radius R_b. Thus, the influence of Re_{mf} becomes less important as the bubble velocity increases, for the same superficial gas velocity. Nevertheless, for the highest Reynolds number tested $Re_{mf} \simeq 100$ and the lowest bubble velocity $U_b = 1.1\, u_{mf}$, the radius of the recirculation could decreases less than 5%. No important differences are observed between the 2-D and the 3-D case in the range of Re_{mf} tested.

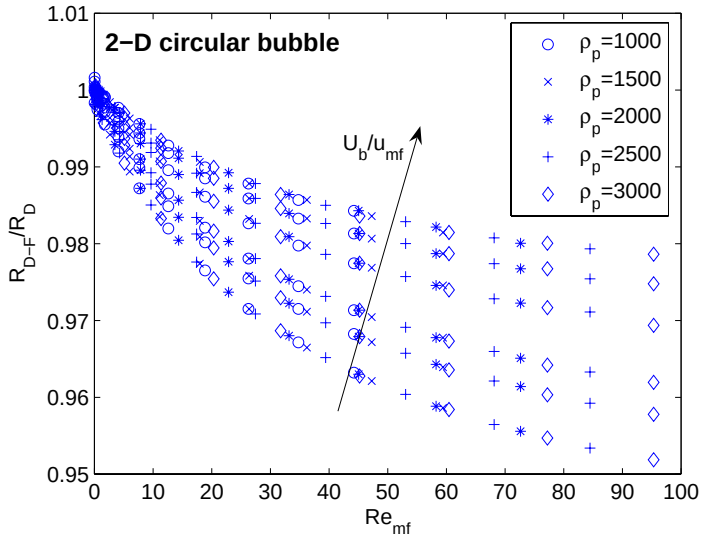

(a)

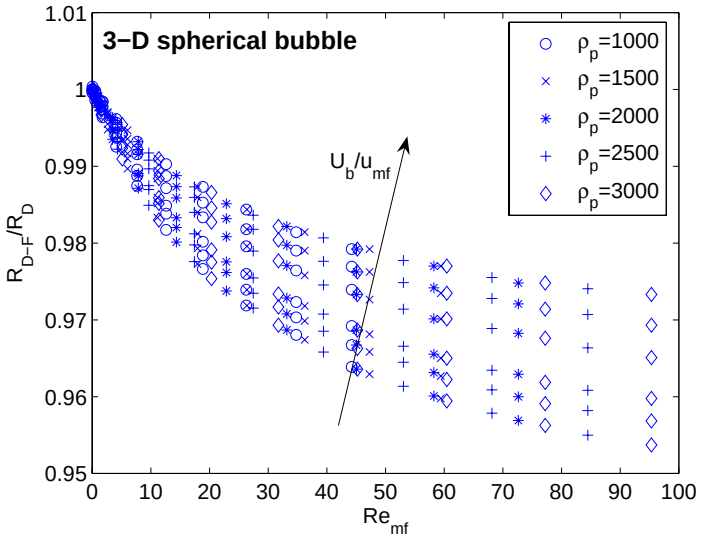

(b)

Figure 3.3: Comparison of the ratio R_{D-F}/R_D for the data showed in table 3.1, for different values of $U_b/u_{mf} = 1.1, 1.3, 1.5, 2.0, 2.5, 3.0$ for a 2-D circular bubble (a) and a 3-D spherical bubble (b). Particle density in kg/m^3.

3.5 Non-Darcy effects in a 2-D freely bubbling fluidized bed

In chapter 2 the equations proposed by Davidson's model were solved in a real bubble geometry captured from a 2-D fluidized bed using a high speed video-camera. The particle velocity was measured using a PIV software and solving the equations (3.1) and (3.3) with a finite element program, the gas velocity field and the pressure distribution

Particle Density (kg/m³)		Particle Diameter (μm)									
		100	200	300	400	500	600	700	800	900	1000
1000	Re_{mf}	0.067	0.533	1.774	4.097	7.693	12.626	18.856	26.280	34.779	44.236
	U_{mf}(m/s)	0.0059	0.0233	0.0517	0.0895	0.1345	0.1840	0.2355	0.2872	0.3378	0.3867
1500	Re_{mf}	0.101	0.798	2.636	6.018	11.134	17.970	26.392	36.221	47.283	59.431
	U_{mf}(m/s)	0.0088	0.0349	0.0768	0.1315	0.1947	0.2618	0.3296	0.3958	0.4593	0.5196
2000	Re_{mf}	0.134	1.061	3.482	7.867	14.368	22.881	33.186	45.044	58.252	72.644
	U_{mf}(m/s)	0.0117	0.0464	0.1015	0.1719	0.2512	0.3334	0.4144	0.4922	0.5658	0.6351
2500	Re_{mf}	0.167	1.322	4.313	9.651	17.429	27.450	39.420	53.059	68.142	84.493
	U_{mf}(m/s)	0.0146	0.0578	0.1257	0.2109	0.3047	0.4000	0.4923	0.5798	0.6619	0.7386
3000	Re_{mf}	0.201	1.582	5.130	11.377	20.342	31.740	45.214	60.455	77.220	95.330
	U_{mf}(m/s)	0.0176	0.0691	0.1495	0.2486	0.3557	0.4625	0.5647	0.6606	0.7501	0.8334

Table 3.1: Values of U_{mf} and Re_{mf} for different particle sizes and densities fluidized with atmospheric air.

in the bed were obtained. The study covered different kinds of bubbles: slow and fast non-interacting bubbles and also interacting and erupting bubbles.

In this section, the results obtained including non-Darcy effects are compared with the ones obtained neglecting the inertial forces, which were showed and explained in more detail in chapter 2. The particles employed during the experiments were spheres with a mean particle diameter of $d_p = 350\,\mu m$ and a density of $\rho_p = 2500 kg/m^3$, which corresponds to fluidization type B according to Geldart classification (Geldart, 1973). With this particles a value of $Re_{mf} \simeq 9$ is obtained, which is represented in figure 3.1 with a cross.

The boundary conditions implemented were the same used in chapter 2, which are similar to the ones used in the circular or spherical isolated bubbles explained in the previous section of this chapter, except the boundary condition at the bottom of the bed. In the previous section a boundary condition of $U = U_{mf}$ was imposed, in contrast, for the bubbles captured in the freely bubbling bed a boundary condition of constant pressure equal to the weight of the particles were employed. In this way, as the pressure gradient including or not the non-Darcy term is the same, some diferencies in the magnitude of the gas velocity are expected.

Figure 3.4(a) shows the gas streamlines viewed by an inertial observer moving with the bubble for a slow bubble with $U_b/u_{mf} = 0.69$. They look quite similar to the streamlines obtained neglecting the Forchheimer term in equation (3.11), which were plotted in figure 2.6(d). Non-Darcy term does not affect noticeable the direction of $\boldsymbol{u}$, although some differences are observed in the magnitude of the gas velocity. In figure 3.4(b) the relative difference between the magnitude of the gas velocity including or not non-Darcy effects, expressed as

$$\Delta u = \frac{u_D - u_{D-F}}{u_D} \tag{3.15}$$

is plotted. This figure shows that the maximum differences are observed in the nose and in the wake of the bubble, where the magnitud of $\boldsymbol{u}$ is higher because of the bubble is a preferential path for the gas flow. The magnitude of $\boldsymbol{u}$ in these regions is of the order of the gas velocity crossing the bubble. For a 2-D bubble this velocity is $\sim 2 \cdot U_{mf}$, although this value increases with the bubble aspect ratio. In contrast, the diferencies are minimum at both sides of the bubble, where u is lower. Nevertheless, the value of the relative difference is $\Delta u \leq 0.12$ around the bubble and the maximum differences are observed at points situated close to the nose and close to the wake of the bubble.

Figure 3.5 shows a fast bubble case. Similar results to the ones obtained in the slow bubble are observed, higher differences in the region close to the top of the bubble

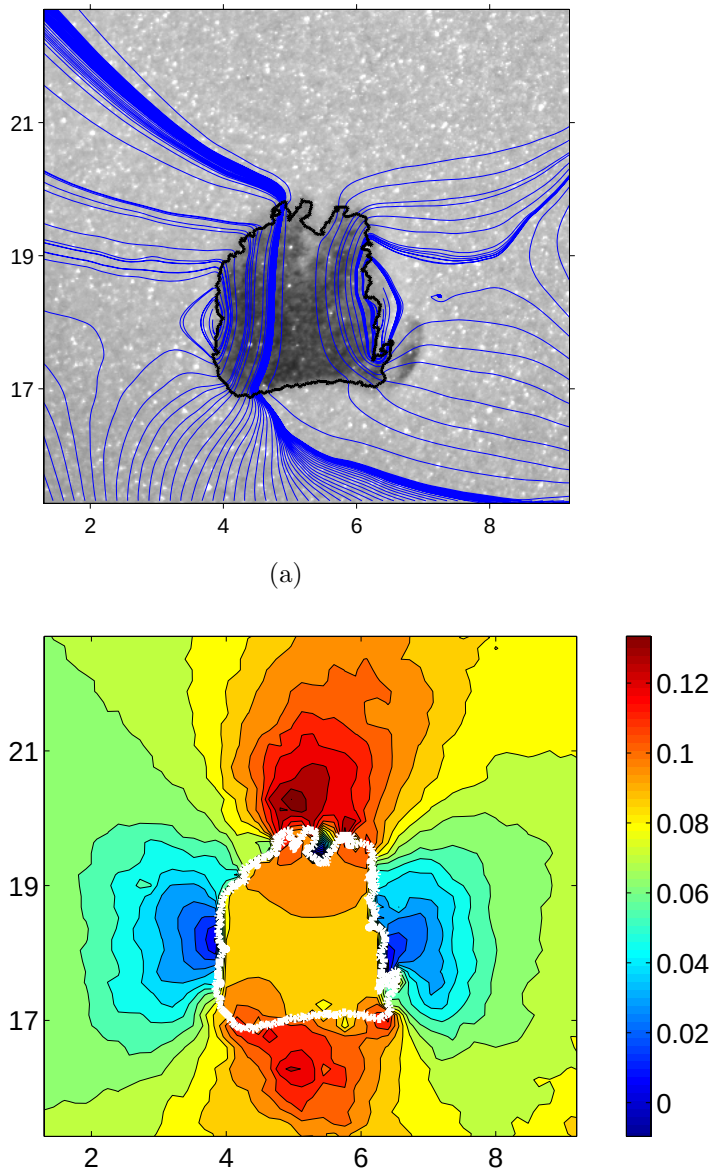

Figure 3.4: (a) Gas streamlines of one slow bubble ($U_b/u_{mf} = 0.69$) viewed by an observer moving with the bubble including non-Darcy effects and (b) relative difference in the magnitude of $\boldsymbol{u}$. Scale in cm.

and lower in the recirculation regions. Although in this case, the maximum difference ($\Delta u \sim 0.3$) is higher, due to the higher bubble velocity.

In both cases, as it is expected, the values of u_D are higher than those of u_{D-F}. The magnitude of the gas velocity is higher neglecting Forchheimer effects for the same pressure gradient. The difference increases with the Reynolds number, although the streamlines in the vicinity of the bubble are not affected appreciably.

Two more cases were analysed: one erupting bubble at the bed surface and two interacting bubbles. The former is showed in figure 3.6, at the instant when the bubble

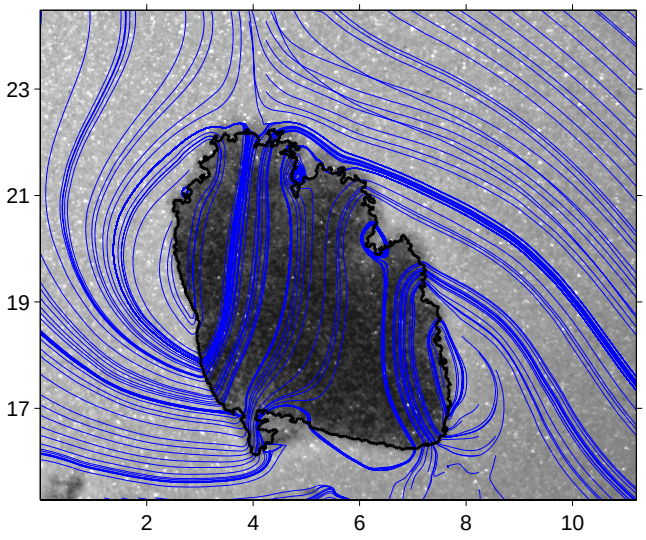

(a)

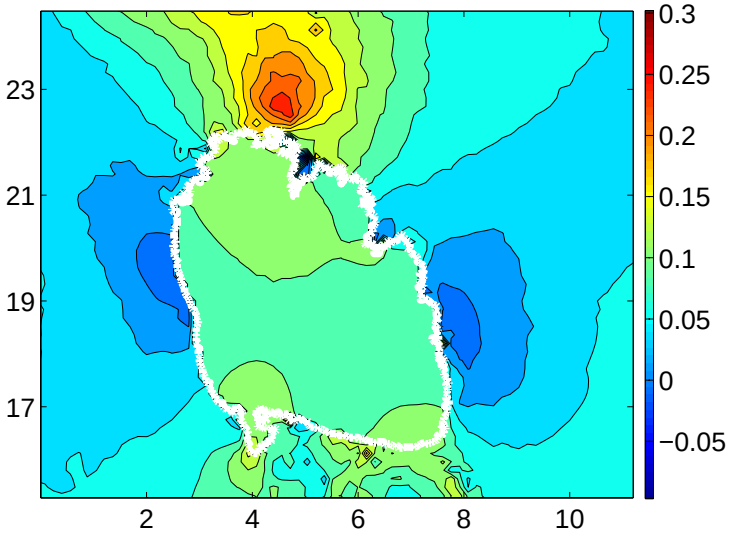

(b)

Figure 3.5: (a) Gas streamlines of one fast bubble ($U_b/u_{mf} = 1.3$) viewed by an observer moving with the bubble including non-Darcy effects and (b) relative difference in the magnitude of $\boldsymbol{u}$. Scale in cm.

breaks the bed surface and most of the gas crossing the bubble reaches the freeboard through the small aperture opened on the top of the dome contour. Although the velocity in this aperture is very high, the value of Δu in this region is not high because the interior of the bubble is connected to the freeboard. Both regions are modeled with a high permeability and, consequently, the non-linear effects are not important in these regions. The latter can be seen in figure 3.7, where the streamlines of the leader bubble interact with the second bubble. In this case, the highest differences in the gas velocity are observed in the top of the leader bubble and in the region situated between the bubbles.

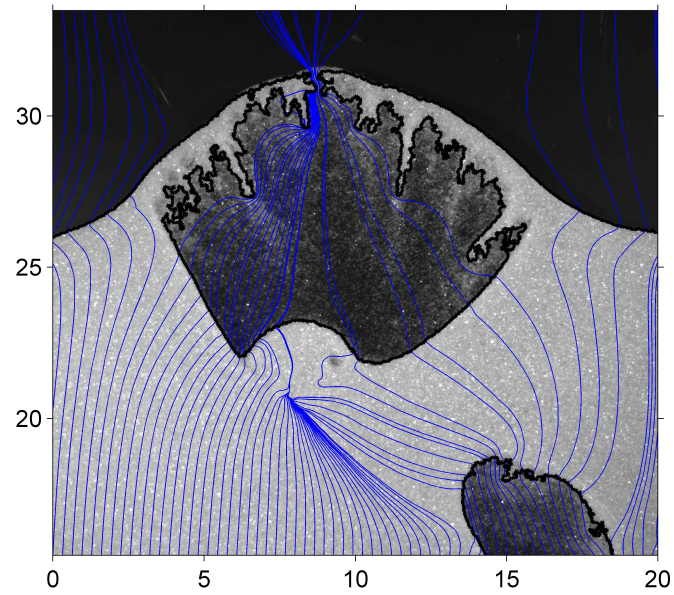

(a)

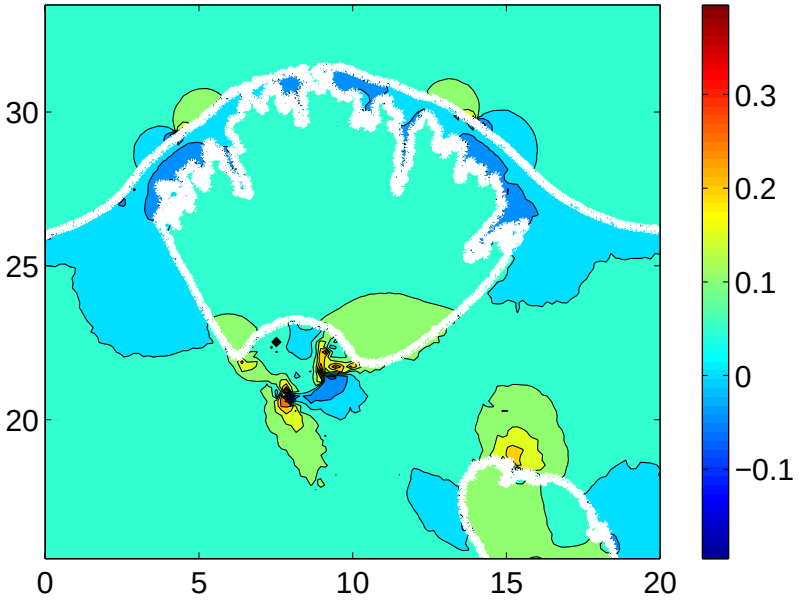

(b)

Figure 3.6: (a) Gas streamlines of one erupting bubble, in the instant when the bubble breaks the bed surface, viewed by a stationary observer including non-Darcy effects and (b) relative difference in the magnitude of $\boldsymbol{u}$. Scale in cm.

Although high differences ($\Delta u \sim 0.3$) are observed in a few isolated points in both cases (erupting and interacting bubbles), the mean difference in the gas velocity inside the bubbles is around $\Delta u \sim 0.1$.

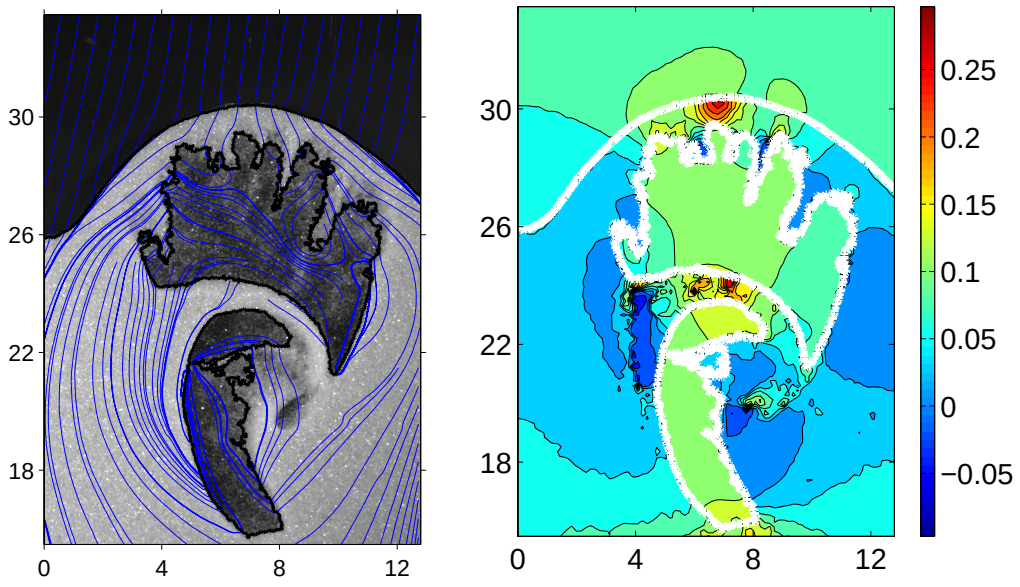

(a) (b)

Figure 3.7: (a) Gas streamlines of two interacting bubbles viewed by an observer moving with the leader bubble including non-Darcy effects and (b) relative difference in the magnitude of $\boldsymbol{u}$. Scale in cm.

3.6 Discussion and conclusions

The original Davidson's model has been extended, including a quadratic term, for taking into account inertial forces using Ergun's equation. According to Zenz and Grigg (2006), non-Darcy effects should be taken into account when Forchheimer number $Fo \geq 0.11$, which corresponds with a limit Reynolds number, defined by equation (3.10), of $Re_{mf_{max}} \approx 10$ using Ergun's equation. This maximum value agrees with the limit suggested by Dybbs and Edwards (1984) for the Darcy flow regime. Nevertheless, the definitions of both Reynolds numbers differ in the characteristic length, and from this study it can not be concluded that the pore characteristic length d_{pore} is equal to $\frac{\phi\, d_p}{(1-\epsilon)}$, specially if ϵ departs so much from ϵ_{mf}. For higher porosities, Ergun's equation is not valid and a different equation should be used. For example, the one proposed by Gibilaro et al. (1985). This expression agrees with Ergun's equation if $\epsilon = \epsilon_{mf}$. In addition, it predicts properly the pressure drop for higher void fractions where Ergun's equation fails.

The results obtained for isolated circular or spherical bubble, show that the cloud radius around fast bubbles decreases when non-Darcy effects become important, i.e., when Reynolds number increases. In addition, the ratio R_{D-F}/R_D tends to one as the ratio U_b/u_{mf} increases. Nevertheless, the maximum diferencie observed between the cloud radius including or not non-Darcy effects is less than 5% for a maximum

Reynolds number of $Re_{mf} \sim 10^2$.

The comparison of the gas velocity field obtained from the bubble geometry captured from a 2-D bubbling bed, including and neglecting the quadratic term in equation (3.11), predicts some differences in the gas velocity $\boldsymbol{u}$. The gas velocity magnitude decreases as the inertial effects become more important, showing maximum differences in the regions around the bubble where $\boldsymbol{u}$ (and consequently the Reynolds number) are higher, that is, in the region close to the nose and to the wake of the bubble.

Nevertheless, in the simplest circular bubble and in the real bubbles captured with the high speed video-camera, the streamlines predicted by Davidson's model do not differ appreciably from the ones computed including non-Darcy effects. Thus, Davidson's model can still be used to predict qualitative the gas flow pattern around bubbles.

In summary, the governing equations of Davidson's model including a quadratic term into gas momentum equation have been successfully solved using a finite element program. The increase of the computational cost with the inclusion of the quadratic term in pressure drop equation is negligible and the time consumed to calculate $\boldsymbol{u}$, $\boldsymbol{v}$ and p_f for one picture does not change and it is still around 3-4 minutes per picture in a regular desktop computer. The numerical results show that the cloud radius is sightly smaller when non-Darcy effects are taken into account and small differences are observed in the gas velocity magnitude u for the same pressure gradient. Nevertheless, these differences are not high enough to modify appreciably the gas stream lines pattern around bubbles, which are properly described by original Davidson's model.

3.7 Notation

A Constant defined in equation (3.11) $[kg/m^4]$

B Constant defined in equation (3.11) $[kg/(s \cdot m^3)]$

d_p Particle diameter $[m]$

Fo Forchheimer number defined by equation (3.5) $[-]$

k Permeability of the medium $[m^2]$

L Length of the bed $[m]$

p_f Fluid pressure $[Pa]$

R Cloud radius around fast bubbles $[m]$

R_b Bubble radius $[m]$

Re Reynolds number defined by equation (3.10) $[-]$

Re_{pore} Reynolds number based on the pore characteristic length defined by equation (3.4) $[-]$

U Superficial gas velocity $[m/s]$

U_0 Superficial gas velocity in a uniform bed without bubbles $[m/s]$

$\boldsymbol{u}$ Interstitial gas velocity $[m/s]$

u_0 Interstitial gas velocity at minimum fluidization conditions

$\tilde{\boldsymbol{u}}$ Relative gas velocity defined in equation (3.3) $[m/s]$

$\boldsymbol{v}$ Particle velocity $[m/s]$

x Horizontal coordinate

y Vertical coordinate

β Non-Darcy coefficient $[m^{-1}]$

ϵ_{mf} Void fraction at minimum fluidization conditions $[-]$

μ Fluid dynamic viscosity $[Pa \cdot s]$

ρ_f Fluid density $[kg/m^3]$

ρ_p Particle density $[kg/m^3]$

ϕ Particle sphericity $[-]$

$(\,)_D$ Darcy

$(\,)_{D-F}$ Darcy-Forchheimer

$(\,)_x$ x component

$(\,)_y$ y component

Bibliography

Bear J., 1972. *Dynamics of fluids in porous media*. American Elsevier

Bird R.B., Stewart W.E. and Lightfoot E.N., 2002. *Transport phenomena (2nd edition)*. John Wiley & Sons, Inc.

Davidson J.F., 1961. Symposium on fluidisation-Discussion. *Transactions of the Institution of Chemical Engineers*, vol. 39, pp. 230-232

Davidson J.F. and Harrison D., 1963. *Fluidised particles*. Cambridge University Press

Dybbs A. and Edwards R.V., 1984. A new look at porous media fluid mechanics - Darcy to turbulence, in: J. Bear, M.Y. Corapcioglu, *Fundamentals of Transport Phenomena in Porous Media*, Dordrecht: Martinus Nijhoff Publishers, pp. 199-254

Ergun S., 1952. Fluid flow through packed columns. *Chemical Engineering Progress*, vol. 48, pp. 89-94

Geldart D., 1973. Types of gas fluidization, *Powder Technology*, vol. 7, pp. 285-292

Gibilaro L.G., Di Felice R., Waldran S.P. and Foscolo P.U., 1985. Generalized friction factor and drag coefficient correlations for fluid-particle interactions. *Chemical Engineering Science*, vol. 40, pp. 1817-1823.

Kunii D. and Levenspiel O., 1991. *Fluidization Engineering*. Butterworth-Heinemann

Liu S. and Masliyah J.B., 1996. Single fluid flow in porous media. *Chemical Engineering Communications*, vol. 150, pp. 653-732

Zenz Z. and Grigg G., 2006. A Criterion for Non-Darcy Flow in Porous Media. *Transport in Porous Media*, vol. 63, pp. 57-69

Chapter 4

Voidage distribution around bubbles in a fluidized bed: influence on throughflow

Contents

4.1 Abstract

In this work, a new method for measuring void fraction distribution around endogenous bubbles in a 2-D fluidized bed is presented. The technique is based on illuminating a transparent-wall 2-dimensional bed with diffuse light from the rear and recording the distribution of light that penetrates the bed. The recording is made with a high speed video-camera, which gives frames with grey level corresponding to the light penetration and from which the voidage distribution around the bubbles can be determined. In this

way, voidage distribution in the region very close to the bubble contour ($r/R_b \lesssim 1.2$) is obtained, which was not possible in previous studies due to limitations in spatial resolution. A correlation is proposed for the voidage at the contour of the bubble, with the voidage depending on the radial position and the polar angle $\epsilon\,(r, \theta)$.

In addition, the effect of the voidage distribution on the throughflow crossing the bubbles was studied and an increase of 20% was determined for the average bubble geometry of the more than 100 bubbles analysed.

4.2 Introduction

In most of gas fluidized beds applications, bubbles appear when the superficial gas velocity exceeds the minimum velocity required to overcome the weight of the bed. Toomey and Johnstone (1952) supposed that all the air in excess over minimum fluidization velocity traverses the bed in the form of gas pockets or bubbles. This assumption is known as the "*two-phase theory*" and was adopted by Davidson (1961) in his model.

Later, Jackson (1963) extended Davidson's model including the momentum equation for the particle phase and assuming that the voidage can vary around the bubble. Jackson included the voidage variation in the function $\beta\,(\epsilon)$ which defines the drag force experienced by the particles. Jackson's model has no analytical solution and an iterative method is needed to solve the system of equations. Also Murray (1965) developed a model similar to Jackson, although he confined the voidage variation in a boundary layer around the bubble. Murray linearized the equations of motion and obtained an analytical solution for the problem.

In order to corroborate these models, Lockett and Harrison (1967) developed a capacitance probe in order to measure the voidage around endogenous bubbles in a 2-D fluidized bed. They demonstrated that around bubbles the voidage of the emulsion phase is higher than ϵ_{mf} and obtained qualitative agreement with Jackson's model. Stewart (1968) showed that adopting an appropriated bubble velocity correlation, the experimental results of Lockett and Harrison (1967) agree with Jackson's model. Nguyen et al. (1973) obtained similar experimental results in a "falling" two-dimensional bed with an artificial bubble made with a gauze cap.

Some years after, Collins (1989) obtained a general expression for the experimental results of Lockett and Harrison (1967) and Nguyen et al. (1973) in the form

$$\frac{1-\epsilon}{1-\epsilon_{mf}} = \exp\left(-k_2\left(\frac{R_b}{r}\right)^3\right) \tag{4.1}$$

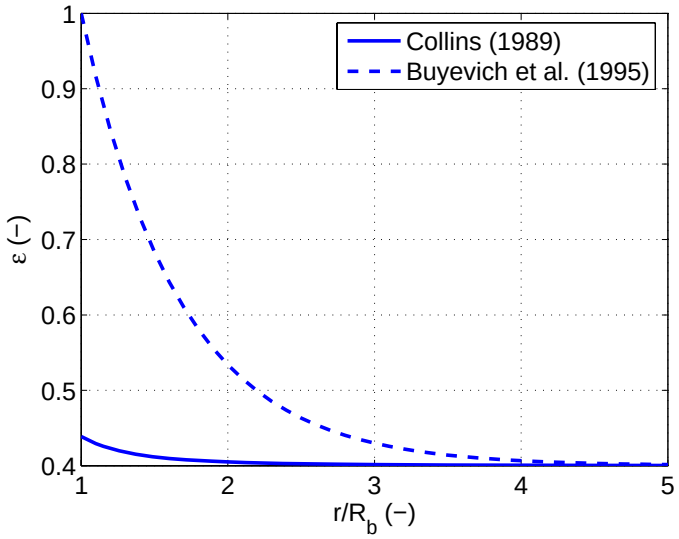

Figure 4.1: Comparison of the radial voidage distribution obtained from equations (4.1) and (4.2) assuming $\epsilon_{mf} = 0.4$.

where R_b is the bubble radius (assumed circular bubbles), r is the distance from the center of the bubble and $k_2 = 1/15$ is a constant adjusted experimentally. Equation (4.1) is obtained assuming radial symmetry for the bubble and for the voidage distribution $\epsilon = \epsilon(r)$.

Using X-rays in a 3-D fluidized bed, Yates et al. (1994) observed the voidage distribution around a stream of injected bubbles. Buyevich et al. (1995) fitted the following exponential equation to the experimental results of Yates et al. (1994)

$$\frac{\epsilon - \epsilon_{mf}}{1 - \epsilon_{mf}} = \exp\left(-1.5\left(\frac{r}{R_b} - 1\right)\right) \tag{4.2}$$

assuming again a radially symmetrical distribution.

Equations (4.1) and (4.2) give much different voidage distributions around bubbles as figure 4.1 shows. The equation proposed by Buyevich et al. (1995) assumed that the voidage is equal to 1 at bubble boundary while Collins (1989) obtained a value of $\epsilon_{bc} = 0.44$, much closer to the value far away from the bubble. The differences observed can be attributed to the different bed geometries (equation (4.1) was obtained for experiments carried out in 2-D fluidized beds, while equation (4.2) was obtained from 3-D experiments). Also the experimental measurement techniques employed in the experiments and the uncertainty and accuracy of the measurements could influence in the deviation between both equations.

In this work, a new method for measuring the voidage distribution around endogenous bubbles in a 2-D freely bubbling fluidized bed is presented. The technique is based on illuminating the bed with a diffuse light from the rear and measure how much light

penetrates the bed (Duru and Guazzelli, 2002). This means that light penetrates the bed when a bubble passes and no light penetrates when there is no bubble present. Around the bubble contour, there is a gradual change in light from full light to no light. The light is recorded by a high speed video-camera which then quantifies the incoming light as grey levels around the bubbles. In this way, voidage levels can be obtained in the region near the bubble contour ($r/R_b \lesssim 1.2$), i.e. where Lockett and Harrison (1967) and Nguyen et al. (1973) could not obtain such values due to limitations in spatial resolution. A new expression for voidage distribution is proposed in the region $r/R_b \lesssim 1.2$.

In addition, following the work of Collins (1989), the influence of the voidage variation on the throughflow crossing the bubbles was analysed numerically. For this study, the mean bubble geometry of the more than 100 bubbles analysed to obtain the voidage distribution was used. The numerical analysis shows that the throughflow crossing the bubble is 20% higher than the throughflow assuming a constant voidage $\epsilon = \epsilon_{mf}$ in the emulsion phase around the bubble.

In the remainder of the paper, the experimental set-up and the calibration method will be described. Then, the main experimental results, together with a correlation for the voidage distribution will be presented. In section 4.5 the influence of the voidage variation on the throughflow crossing the bubble will be analysed numerically. Finally, section 4.6 summaries and discusses the main conclusions of the work.

4.3 Experimental set-up and calibration

The experimental facility employed during the experiments is similar to the one described in more detail in Santana et al. (2005). A 2-D fluidized beds (110 cm width, 60 cm height and 0.5 cm thickness) made with two glass walls. The rear wall of the bed was illuminated with a spotlight and onion paper was placed behind the bed with the aim of spreading the light as much as possible and avoiding flared highlights. A high speed video-camera of 1.3 Megapixels resolution (1024 $\times$ 1240 pixels) was placed in the front of the bed taking pictures. The time that the shutter was open in each picture was only 1/5000 s in order to prevent blurring by the motion of the bubbles. In all experiments the superficial velocity was varied between $1 \leq U/U_{mf} \leq 2$. Higher velocities were discarded in order to prevent the entrainment of particles out of the bed. The height of the fixed bed during the experiments was 30 cm approximately.

Two types of spherical glass particles were employed in the experiments, both of them with a density of $\rho_p = 2500\,\frac{kg}{m^3}$. One group of particles had a mean diameter of $d_p = 350\,\mu m$ and the other one $d_p = 600\,\mu m$. Two different particle sizes were tested

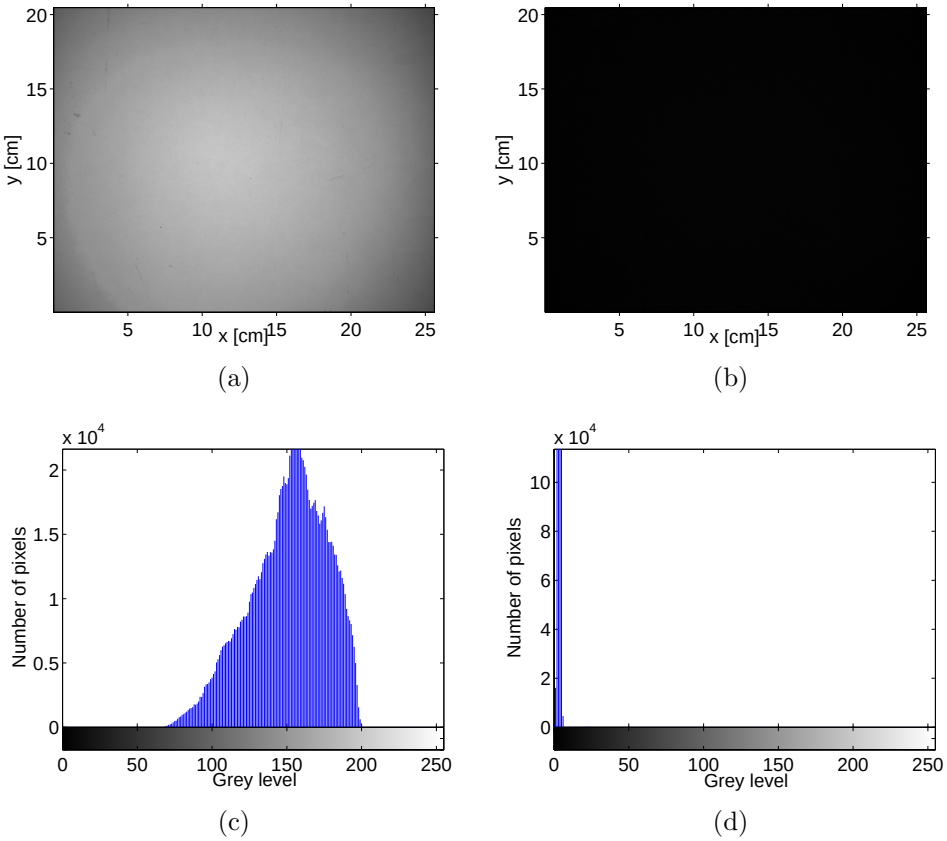

Figure 4.2: (a) Average picture of the empty bed and (b) average picture with the bed at minimum fluidization condition, while (c) and (d) show the grey histograms respectively.

in order to study the influence of d_p in the voidage distribution, although finally no noticeable differences were observed between them.

Before each experiment, two series of 100 pictures were captured for calibration. One with the empty bed and another one with the bed slightly under minimum fluidization conditions in order to avoid the presence of bubbles. The grey level obtained with the empty bed was used as a spatial calibration of voidage $\epsilon = 1$ (Goldschmidt et al., 2003). The grey map obtained from the pictures at minimum fluidization conditions is ϵ_{mf}. In order to determine the value of ϵ_{mf}, the weight of the particles was measured before introducing them into the bed. A value of $\epsilon_{mf} = 0.4$ was obtained for both particles sizes.

The mean picture of two calibration series are shown in figure 4.2 together with their histograms. The size of the picture captured from the central region of the bed with the camera is approximately $20 \times 25\,cm$. Thus, only a small section of the bed is captured in order to get a high spatial resolution. The white picture is similar to the one obtained by Goldschmidt et al. (2003) who used it to correct local light intensities in their segregation study. A lighter region appears in the center of the

image. During the calibration, a proper selection of the light intensity and the aperture of the diaphragm must be taken. Very high light intensity or long time of exposure can result in appearance of flared highlights in the center of the picture, although low intensity or short time of exposition could reduce the range of variation of the grey levels so much. In contrast, figure 4.2(b) shows that at minimum fluidization conditions almost no light traverses the bed and the histogram is narrow and near 0.

According to Russ (1994), there is a logarithmic relationship between the grey level (G.L.) and the ratio of the incident light that penetrates through the bed without been absorbed or scattered (I/I_0). On the other hand, in order to obtain a relationship

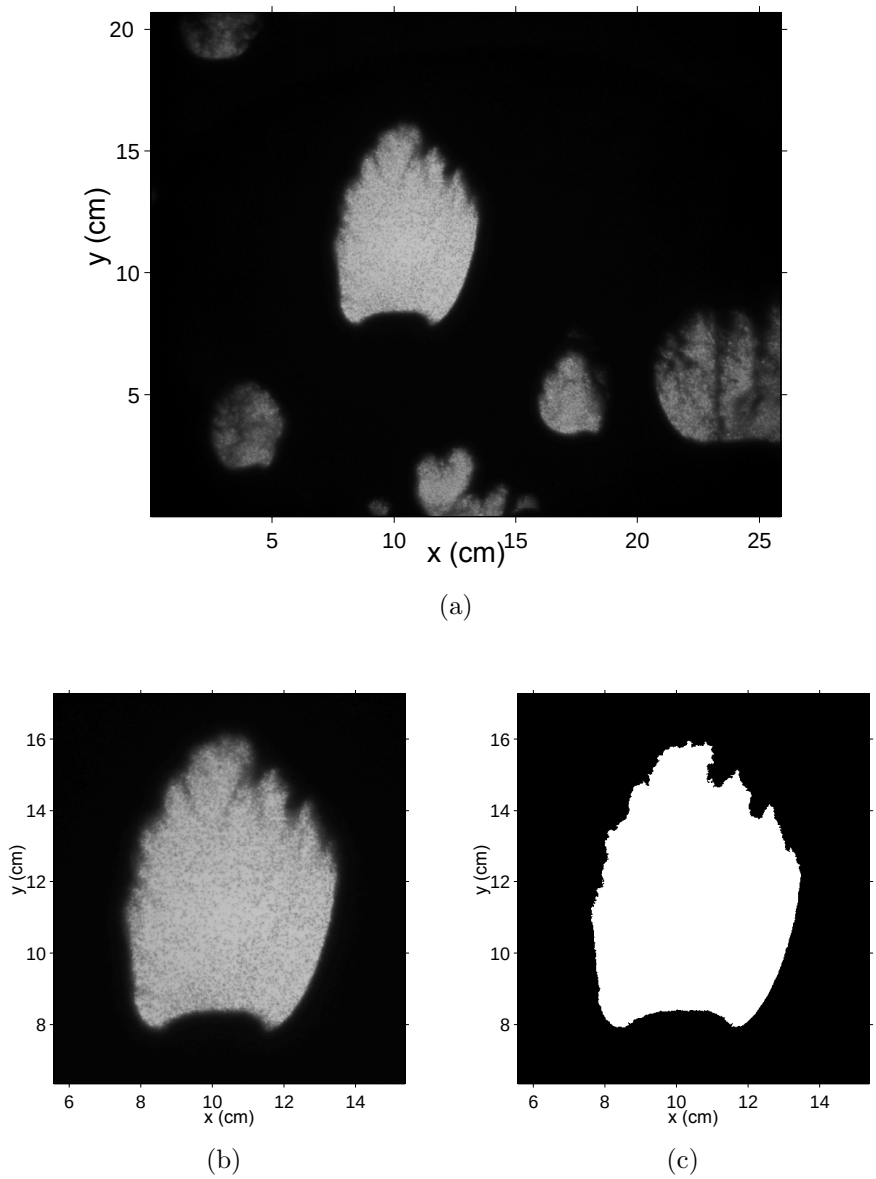

(a)

(b) (c)

Figure 4.3: (a) Typical picture captured with the high speed video-camera, (b) bubble selected and (c) bubble contour obtained using the threshold algorithm proposed by Otsu (1979).

between the grey level and the voidage, an exponential law is assumed to relate the light intensity with the particle concentration $(1-\epsilon)$. In this way, a linear relationship between the grey level and the solid concentration is obtained (Poletto et al., 1995; Boerefijn and Ghadiri, 1998).

Therefore, a linear relationship was assumed to transform grey levels into voidage values. The calibration picture with the empty bed was assumed as spatial calibration for $\epsilon = 1$ and the one at minimum fluidization conditions was assumed as $\epsilon = \epsilon_{mf}$.

4.4 Experimental results

For each particle size, a total of six series of pictures were taken. The time lag between each serie was 5 minutes approximately, resulting in a total time of 30 minutes. A total of 3272 pictures were captured at a rate of 250 fps in each serie. Approximately, 10 bubbles from each serie were selected to analyse the voidage distribution. Finally, a total of 116 different bubbles were analysed (65 bubbles from experiments with particles of $d_p = 350\,\mu m$ and 51 from experiments with particles of $d_p = 600\,\mu m$).

Figure 4.3(a) shows a typical picture captured with the high speed video-camera when the bed is freely bubbling. Once a bubble was selected, a rectangular region enclosing the bubble was cut (figure 4.3(b)). The bubble contour was obtained applying a local threshold value, calculated according to the method developed by Otsu (1979), which obtains optimal threshold values compared with other methods (Gonzales-Barron and Butler, 2006). This threshold value was calculated only in the neighborhood of the bubble (figure 4.3(c)). Note that the illumination can not be per-

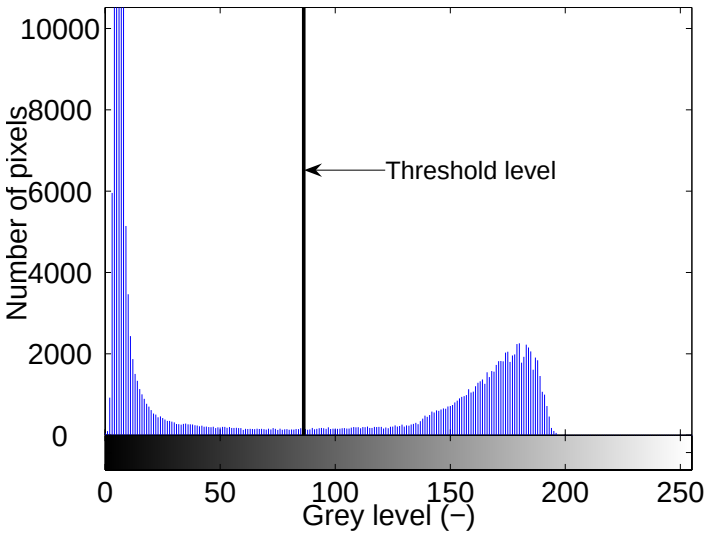

Figure 4.4: Grey histogram and threshold value obtained for picture showed in fig 4.3(b).

fectly uniform (see figure 4.2(a)) and the threshold value will be higher in the central region of the picture and lower in periphery. Thus, a local threshold value is necessary in order to detect properly the bubble contour. Figure 4.4 shows the histogram obtained for the picture showed in figure 4.3(b) and the threshold value that defines the bubble contour. The histogram is wide enough and both phases (bubble and dense phase) can be distinguished properly.

From figure 4.3(b) it can be inferred that the interior of the bubble is not completely free of particles, and therefore the voidage inside of the bubble is $\epsilon_b \lesssim 1$. Figure 4.3(b) also shows that at the nose of the bubble typical instabilities appear and the particles rain in the form of "stalactites". These elongated group of particles can reach the bottom of the bubble and split the bubble in two (Rowe and Partridge, 1965). This effect could be more common in 2-D beds because of the wall effect.

Bubbles of different sizes and shapes were analysed. Figure 4.5 shows the distribution of the bubble size, bubble eccentricity and bubble orientation. The bubble size was calculated as the surface equivalent diameter, whereas the bubble eccentricity was obtained as the eccentricity of the ellipse[1] that has the same second-moments as the bubble. The bubble orientation was defined as the angle (in degrees) between the horizontal axis and the major axis of the ellipse that has the same second-moments as the bubble. The Probability Density Functions (PDF) were obtained as the distributions that maximize the Shannon's entropy (Santana et al., 2006).

Figure 4.5 shows no-important differences between the distributions obtained for both particle sizes. Bubbles captured from the experiments carried out with particles of $d_p = 600\mu m$ seem to be more elongated (higher eccentricities), although the bubble size distribution is quite similar in both cases.

With the threshold value obtained for the bubble contour, the grey level was transformed into voidage values, as was explained in section 4.3. Figure 4.6 shows the voidage at the bubble contour, ϵ_{bc}, obtained for more than 100 different bubbles. The mean value is $\bar{\epsilon}_{bc} = 0.665$. Particles of higher mean diameter seem to obtain higher values of ϵ_{bc}, although a clear tendency is not observed because of the high scattering of the experimental results. Buyevich et al. (1995) developed a theoretical model for the voidage distribution along the vertical axis of a circular bubble. They concluded that ϵ_{bc} is the same at the top and at the bottom of the bubble. In addition, for a value of $\epsilon_{mf} = 0.4$, neglecting the influence of the particle pressure and applying the continuity equations across the bubble contour, they obtained values of $\epsilon_{bc-} = 0.75$ and $\epsilon_{bc+} = 0.56$ at the inside and outside bubble surface respectively. The mean value

[1]The eccentricity of an ellipse is the ratio of the distance between the foci of the ellipse and its major axis length. A value of 0 is actually one circle, while a value of 1 corresponds with a line.

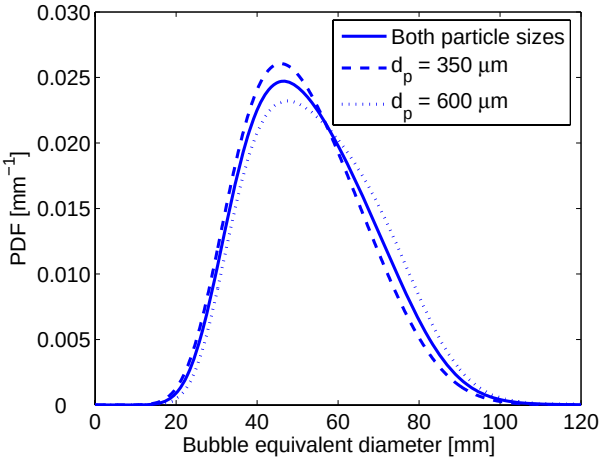

(a)

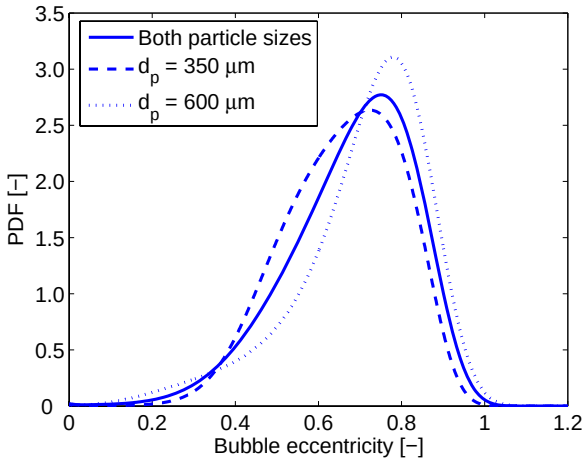

(b)

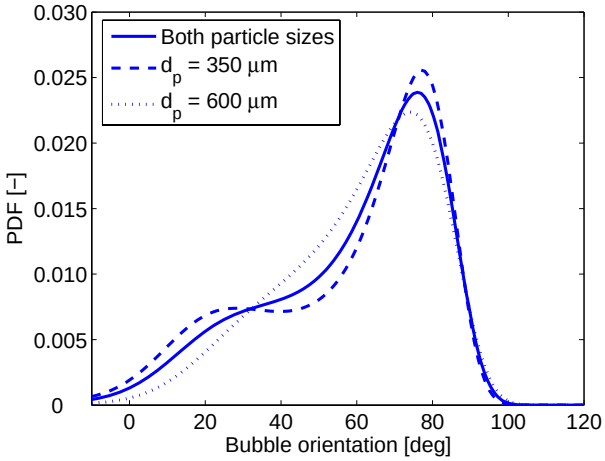

(c)

Figure 4.5: Probability Density Functions of (a) bubble size, (b) bubble eccentricity and (c) bubble orientation. Data obtained from experiments carried out with two different particle sizes.

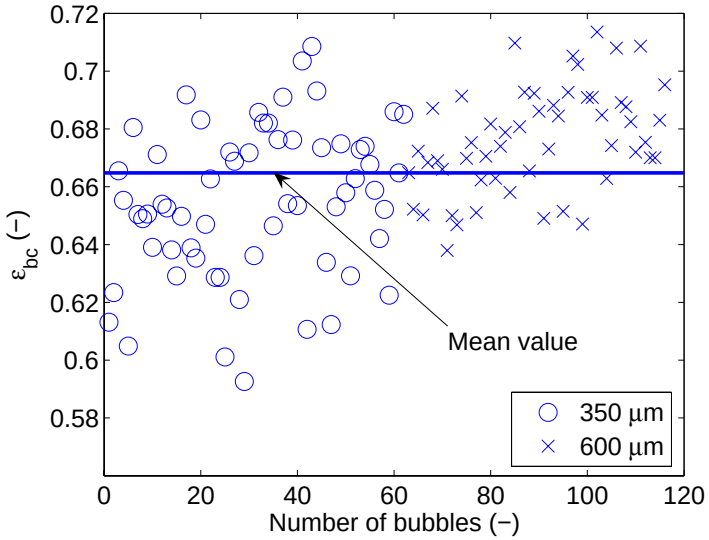

Figure 4.6: Voidage values at the bubble contour for two different particle sizes ($d_p = 350\mu m$ and $d_p = 600\mu m$). The solid line indicates the mean value $\bar{\epsilon}_{bc} = 0.665$.

obtained here and all individual data showed in figure 4.6 fall into both limits.

Around the bubbles, different voidage contours, i.e. different grey levels, were obtained. Figure 4.7(a) shows the results obtained for the bubble showed in figure 4.3(b). The value of the voidage at the bubble contour is $\epsilon_{bc} = 0.681$. A zoom of the nose of the bubble is showed in figure 4.7(b). In the same figure, the effect of the particles raining as one "stalactite" is observed: the voidage gradient is lower in that region, because the particles rain and spread in the interior of the bubble. This effect results in a more difficult detection of the bubble contour in the nose of the bubble. The voidage contours were properly detected until a minimum value of

$$\epsilon^*_{min} = \frac{\epsilon_{min} - \epsilon_{mf}}{\epsilon_{bc} - \epsilon_{mf}} \simeq 0.2 \tag{4.3}$$

Lower values of voidage could not be obtained because there is not enough grey range between ϵ_{min} and ϵ_{mf} and also, in some cases, a closed contour of constant voidage does not appear for such low values of ϵ.

In order to obtain a voidage distribution $\epsilon = \epsilon(r, \theta)$ around the bubbles, 12 lines forming and angle of $\pi/6\, rad$ between them were traced from the center of mass of each bubble. The intersection between the bubble contour and these lines defined 12 points at the bubble contour. From these starting points, 12 lines perpendicular to the contour of the bubble were traced and the intersections of these lines with the constant voidage contours defined the voidage gradient for each direction (see figure 4.8).

Collins (1989) supposed radial symmetry when he adjusted equation (4.1) to the experimental data of Lockett and Harrison (1967) and Nguyen et al. (1973). The

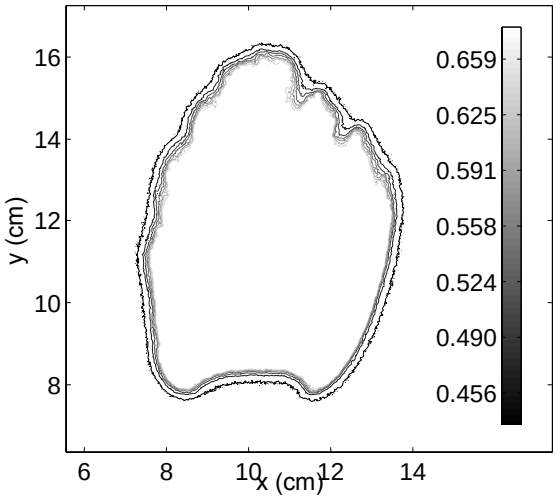

(a)

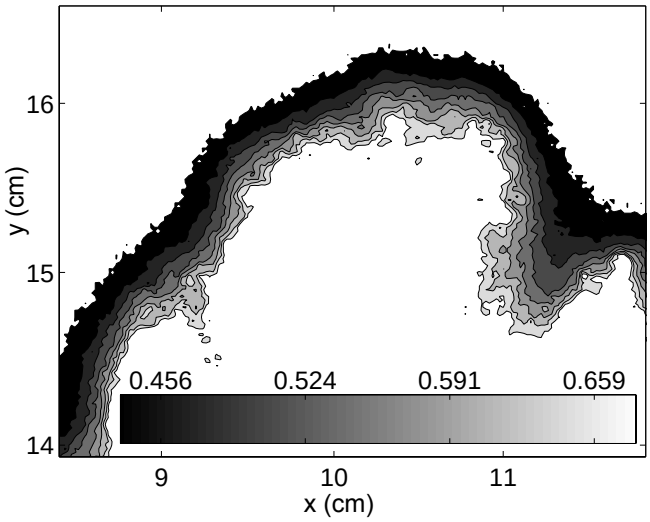

(b)

Figure 4.7: (a) Voidage constant lines around the bubble showed in figure 4.3(b) with $\epsilon_{bc} = 0.681$ and (b) detail of the nose of the bubble with one "stalactite".

voidage data profiles of Lockett and Harrison (1967) were obtained for bubbles with an approximately circular shape. Although some elongated bubbles were observed, only the data from the nose and from the wake were measured for these bubbles. Moreover, the geometry of the fixed artificial bubble employed by Nguyen et al. (1973) was also circular. Both series of experiments obtained voidage profiles in a region of $r/R_b > 1.2$, where the voidage values are $\epsilon^* \lesssim 0.2$. Buyevich et al. (1995) also assumed radial symmetry in equation (4.2). The voidage distribution data were obtained from the horizontal section across the equator of injected bubbles and they did not observed differences along the upper half of the bubble. No data of the voidage distribution in

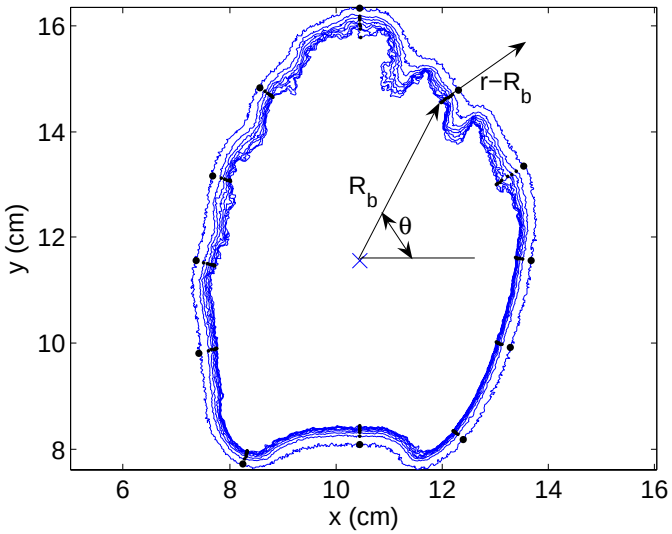

Figure 4.8: Voidage variation in each direction. The points are the intersection of the constant voidage curves with the perpendicular line to the bubble contour. The cross indicates the center of mass of the bubble.

the lower half were obtained.

In contrast, most of the bubble observed in this work were elongated bubbles (see figure 4.5(b)) because of the interaction and coalescence between bubbles in freely bubbling beds. Also, lower voidage gradients in the nose of the bubble because of the effect of the "stalactites" could be expected. In this way, an equation of the form

$$\epsilon^* = \frac{\epsilon - \epsilon_{mf}}{\epsilon_{bc} - \epsilon_{mf}} = \exp\left(-k_1(\theta) \cdot \left(\frac{r}{R_b} - 1\right)\right) \tag{4.4}$$

was proposed to fit the data of all bubbles in each direction, where $k_1(\theta)$ is a positive function of the direction. Higher values of $k_1(\theta)$ implies higher voidage gradients, as ϵ decreases faster, and viceversa. The variables θ, R_b and r are defined in figure 4.8.

In agreement with the observation of Buyevich et al. (1995), no noticeable differences were observed for k_1 in the upper half of the bubble ($0 \leq \theta \leq \pi$), although higher values of k_1 were obtained in the lower half. The voidage distribution is symmetric

$\boldsymbol{\theta}$	$\boldsymbol{k_1}$
$[0 - \pi]$	15.5
$-\pi/6, -5\pi/6$	25.0
$-\pi/3, -2\pi/3$	29.7
$-\pi/2$	22.8

Table 4.1: Experimental values of k_1 for different values of θ adjusted for 116 different bubbles. Symmetry around the vertical axis is assumed.

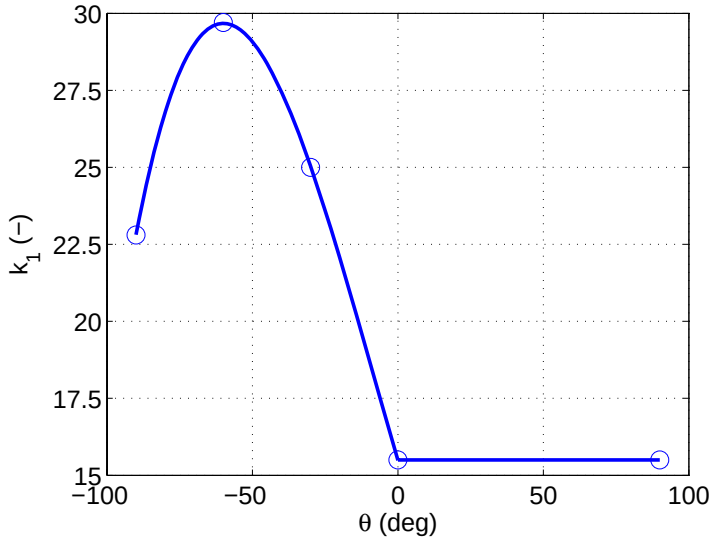

Figure 4.9: Variation of k_1 with the angle θ. The circles indicate the data showed in table 4.1. The data are symmetric respect to the vertical axis of the bubble.

respect to the vertical axis, although the value of k_1 varies with θ, thus, there is not radial symmetry. Table 4.1 shows the numerical values of k_1 for different values of θ and figure 4.9 shows graphically the variation of k_1 with θ using a cubic spline interpolation for the data between $-\pi/2 \leq \theta \leq 0$.

In the following section, the influence of the voidage distribution (equation (4.4)) on the throughflow crossing the bubble is studied numerically. Higher values of voidage imply lower resistance to the gas flow. Consequently, the throughflow is higher than the one calculated assuming a constant voidage value $\epsilon = \epsilon_{mf}$ in the emulsion phase (Collins, 1989; Gera and Gautam, 1994).

4.5 Influence of voidage variation on the gas flow through a bubble

The voidage distribution around bubbles showed that, in the region very close to the dome contour $r/R_b \lesssim 1.2$, neither the bubble geometry nor the voidage distribution are radially symmetrical, although both of them are symmetrical respect to the vertical axis of the bubble. Thus, in order to study the influence of the voidage variation on the gas flow around a bubble, the mean geometry of the 116 bubbles observed in the experiments will be used, instead of an artificial circular or kidney shape bubble.

The mean geometry is obtained from the points detected at the bubble contour separated $\pi/6\,rad$. The mean position of each point is shown in figure 4.10 as circles. All the points, except the one situated at the bubble wake ($\theta = -\pi/2$) adjust properly

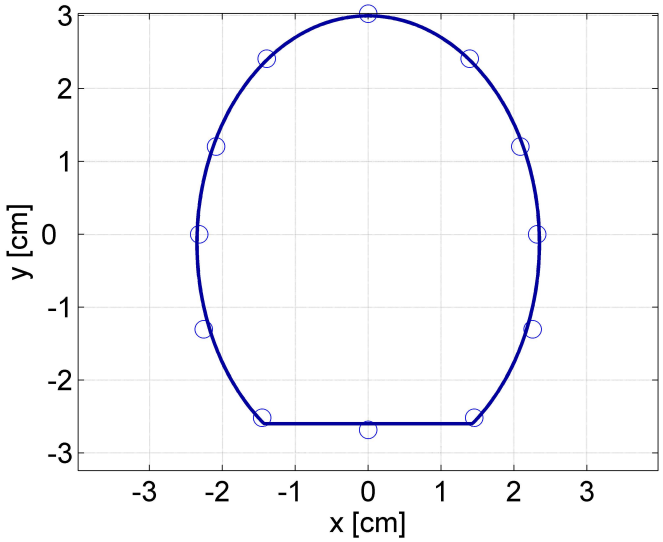

Figure 4.10: Mean bubble geometry obtained from 116 bubbles.

to an ellipse of $A = 31.2\,mm$ and $B = 23.5\,mm$, where A and B are the major and minor semiaxes respectively. In contrast, the wake region of the bubble is approximately flat. Thus, the mean bubble geometry can be modeled as a truncated ellipse.

In order to study how the voidage variation around bubbles influences on the gas through the bubble, numerical results obtained assuming a variable voidage outside the bubble are compared with those obtained with constant voidage $\epsilon = \epsilon_{mf}$. Jackson (1963) developed a model including the porosity variation in the emulsion phase, extending the previous and simpler model of Davidson (1961), which assumed $\epsilon = \epsilon_{mf}$. The governing equations proposed by Jackson (1963) for an observer moving with the bubble are

$$\nabla \cdot (\epsilon\, \boldsymbol{u}) = 0 \tag{4.5}$$

$$\nabla \cdot ((1-\epsilon)\, \boldsymbol{v}) = 0 \tag{4.6}$$

$$\nabla p_f + \beta\,(\epsilon)\ (\boldsymbol{u} - \boldsymbol{v}) = 0 \tag{4.7}$$

$$\rho_p\ (1-\epsilon)\ \boldsymbol{v} \cdot \nabla \boldsymbol{v} - \rho_p\ (1-\epsilon)\ \boldsymbol{g} - \beta\,(\epsilon)\ (\boldsymbol{u} - \boldsymbol{v}) = 0 \tag{4.8}$$

where equations (4.5) and (4.6) are the continuity equations and (4.7) and (4.8) the momentum equations for gas and solid phases respectively. Davidson (1961) neglected the particle momentum equation (assuming irrotational particle flow) and simplified equations (4.5)-(4.7) assuming a constant porosity. In this way, Collins (1989), in order to study the effect of voidage variations on the gas flow associated with a bubble ascending in a fluidized bed, retained porosity spatial variations in equations (4.5)-(4.7),

although he maintained the Davidson's idea of irrotational flow for particle phase. With these assumptions, Collins (1989) showed that the pressure field p_f is independent of the particle motion and, as a result, the interstitial gas velocity can be obtained as

$$\boldsymbol{u} = \boldsymbol{v} + \tilde{\boldsymbol{u}} \tag{4.9}$$

where $\tilde{\boldsymbol{u}}$ is the relative velocity between both interstitial velocities.

Nevertheless, focus in this work is on studying the increase of the throughflow crossing a bubble on account of the higher values of the porosity around the bubble. The voidage value within the bubble was assumed as $\epsilon_b \approx 1$ although figure 4.3(b) reveals the presence of some dispersed particles within the bubble, raining down from the bubble roof. However, the volume filled in with particles is negligible respect to the bubble volume because the number of raining particles is small and uniformly distributed. In consequence

$$u_b = \tilde{u}_b = \frac{U_b}{\epsilon_b} \approx U_b \tag{4.10}$$

Equation (4.10) shows that the throughflow crossing the bubble is independent of the particle movement within the bubble. In this way, to determine U_b, equations (4.5)-(4.7) can be simplified assuming $\boldsymbol{v} = 0$. Then, the equations to solve are reduced to

$$\nabla \cdot (\epsilon\, \boldsymbol{u}) = 0 \tag{4.11}$$

$$\nabla p_f + \beta(\epsilon)\, \boldsymbol{u} = 0 \tag{4.12}$$

Introducing the concept of the permeability of the medium, defined as $K_e(\epsilon) = \frac{\mu\,\epsilon}{\beta(\epsilon)}$, and taking into account the relationship between the interstitial and superficial gas velocity $U = u\,\epsilon$, equations (4.11) and (4.12) can be combined resulting in

$$\nabla \cdot \left[-\frac{K_e(\epsilon)}{\mu} \nabla p_f \right] = 0 \tag{4.13}$$

Then, the pressure field can be obtained solving equation (4.13) and the gas velocity components from equation (4.12).

In fact, Davidson and Harrison (1963) followed the same procedure to obtain the throughflow crossing the bubble, although they assumed $\epsilon = \epsilon_{mf}$ and equation (4.13) reduced to the Laplace equation

$$\nabla^2 p_f = 0 \tag{4.14}$$

which was solved analytically for circular and spherical bubbles with appropriate boundary conditions.

Different functions can be found in the literature that relate the permeability K_e with the porosity ϵ. In this work, the linear term of Ergun equation (Ergun, 1952), also known as the Carman-Kozeny equation:

$$K_e(\epsilon) = \frac{\epsilon^3 (\phi\, d_p)^2}{150\ (1-\epsilon)^2} \tag{4.15}$$

was employed, where ϕ is the particle sphericity ($\phi = 1$ in our case).

Equation (4.13) was solved using a finite element program, Comsol Multiphysics. In order to solve numerically the problem of a bubble moving in a infinite medium, the dimensions of the domain must be much larger than the bubble radius, in order to avoid influences of the boundary conditions and approximate to the theoretical infinite medium. Finally, a rectangular domain with dimensions of $200\, R_b$ high and $100\, R_b$ width was chosen, which was tested to be large enough to eliminate boundary conditions influences. Larger dimensions of the domain does not change the final result and increase the computational cost.

Constant pressure was used as boundary condition for the bottom and pressure outlet for the top of the computational domain, because a bubble ascending in an infinite medium at minimum fluidization conditions is assumed. The numerical value of the pressure at the bottom of the bed is not relevant because the value of the flow is imposed by the pressure drop in the bed, which is obtained by the medium permeability (equation (4.15)). No penetration condition was chosen for the lateral boundaries. The same boundary conditions were assumed by Croxford (2006) in order to solve the Laplace equation (equation (4.14)) to obtain the pressure field in a freely bubbling fluidized bed and in a bed with injected bubbles. Croxford (2006) compared satisfactorily the numerical results with data from experimental measurements.

The mean bubble geometry shown in figure 4.10 was situated in the middle of the domain and $\bar{\epsilon}_{bc} = 0.665$ was chosen as mean value of the voidage at the bubble contour. The voidage distribution around the bubble was calculated according to equation (4.4) using the values of $k_1(\theta)$ shown in figure 4.9, until the voidage reaches a value of $\epsilon = \epsilon_{min} = 0.46$. Equation (4.4) is not valid for low values of ϵ. Instead, the distribution proposed by Collins (1989) (equation (4.1)), which is based on voidages $\epsilon \leq 0.46$, obtained for $r \gtrsim 1.2 \cdot R_b$, is used. Also these data were obtained from experiments in 2-D beds, similar to the one used in this work. The constant $k_2 = 1/15$ of equation (4.1) was modified in order to get a continuous voidage distribution and avoid an abrupt change in the voidage because of the different correlations. Instead, a value of k_2 in the range $[1/7 - 1/8]$ (depending on the value of θ) was used. Figure 4.11 shows the variation of ϵ for $\theta = 0$. A region very close to the bubble contour where

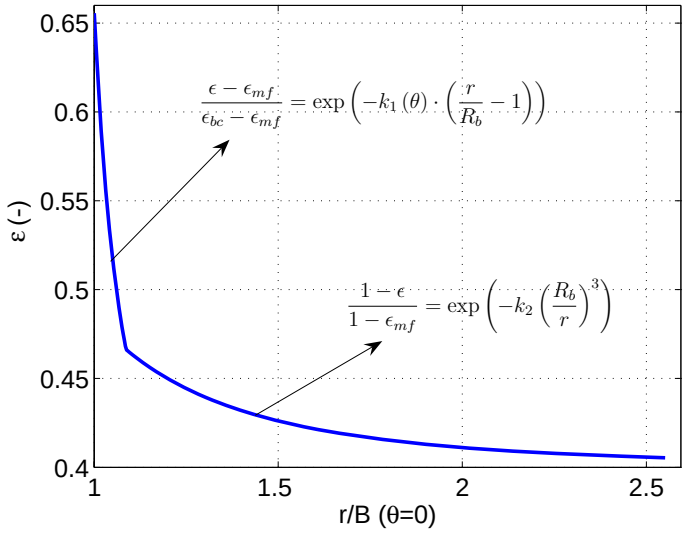

Figure 4.11: Voidage distribution around the mean bubble at $\theta = 0$. $k_1 = 15.5$ and $k_2 = 1/7$.

the voidage decreases rapidly down to ϵ_{min} can be seen. Then the voidage decreases more slowly according to the equation proposed by Collins (1989).

The permeability in the emulsion phase outside of the bubble, k_b, obtained from equation (4.15) ranged between 10^{-9} and 10^{-10} for maximum and minimum porosities respectively. The bubble interior was numerically modeled as a region of very high permeability $K_b \gg K_e$. In this way, the bubble is a preferential path for the gas flow crossing the bed.

The numerical scheme was verified against the simplest case of an isolated circular bubble, which was analysed previously in chapter 2. Having the Davidson's model as basis, the results obtained in chapter 2 show that the flow crossing the circular bubble is $q_b = 4 \cdot U_0 \cdot R_b$ and the pressure is constant within the bubble and equals to the pressure at same height level far away from the bubble. Thereby, agreeing with the characteristic streamlines for slow and fast bubble cases obtained analytically by Davidson (1961).

Figures 4.12(a) and 4.12(b) represent, respectively, the velocity vectors $\boldsymbol{u}$ and the streamlines obtained for the mean bubble geometry viewed by a stationary observer. The left side of each figure represents the results obtained assuming $\epsilon = \epsilon_{mf} = 0.4$ everywhere outside the bubble and the right side the data assuming a variable voidage. Streamlines are quite similar and there is little difference between the two cases. Thus, the gas path is not affected by variations in voidage. In contrast, the modules of the velocity vectors obtained for the constant voidage case are slightly smaller than those of the variable-voidage case. An integration of the gas flow along the minor semi-axis

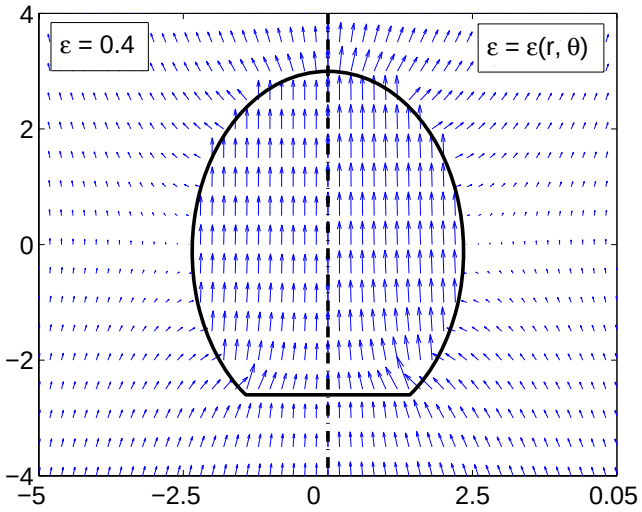

(a)

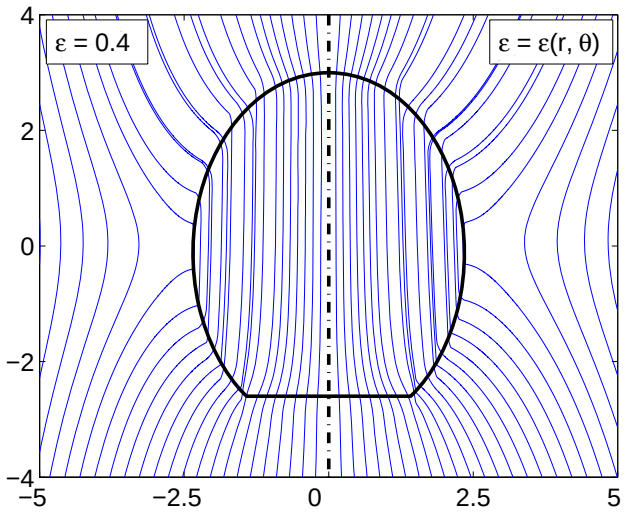

(b)

Figure 4.12: Representation of $\boldsymbol{u}$, the right side of the bubble represents the result obtained with a variable voidage and the left side the result assuming a constant voidage value of $\epsilon = \epsilon_{mf} = 0.4$ in the emulsion phase. (a) Velocity vectors and (b) Streamlines.

of the bubble yields

$$\left.\frac{q_b}{U_0 \cdot B}\right|_{\epsilon=0.4} = 4.53 \tag{4.16}$$

for the constant voidage case and

$$\left.\frac{q_b}{U_0 \cdot B}\right|_{\epsilon=\epsilon(r,\theta)} = 5.44 \tag{4.17}$$

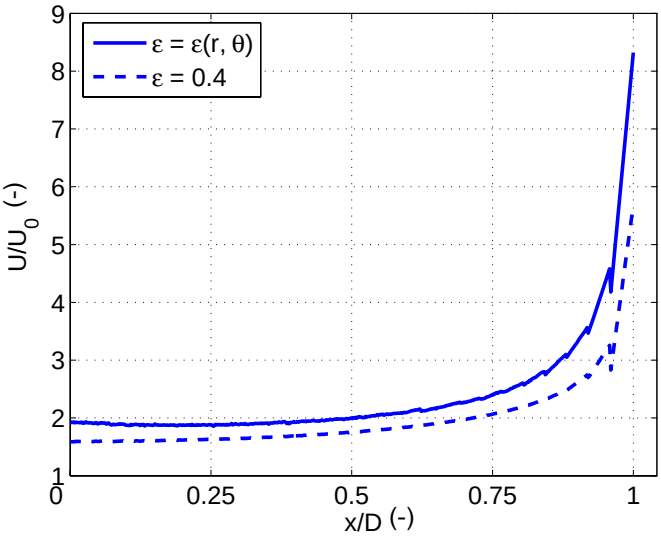

Figure 4.13: Gas flow crossing the bubble through the flat region of the bubble's wake.

for the variable voidage. Thus, including the voidage distribution around the bubble results in an increases of 20% in the flow crossing the bubble. This result is logical, as higher porosities around the bubbles mean higher permeabilities and therefore lower resistance to the gas flow.

Figure 4.13 shows the gas flow profiles crossing the bubble through the flat wake of the bottom of the bubble assuming variable (solid line) and constant voidage (dashed line). In both cases, in the region close to the corner ($x/D \simeq 1$), the gas flow is much higher than in the middle region of the bubble wake ($x/D \simeq 0$). This indicates that the truncated geometry of the bubble gives a significant increase in the flow in the region corresponding to $\theta = -\pi/3$ and $\theta = -2\,\pi/3$, where the ellipsoidal geometry of the bubble is transformed into a flat wake.

4.6 Discussion and conclusions

Benveniste et al. (1983) and Qassim et al. (1989) studied the influence of the voidage variation around isolated circular bubbles, assuming a voidage distribution given by equation (4.1). They obtained an analytical solution for both, gas and particle stream functions, in the form of an infinite summation. They concluded that the voidage variation does not affect appreciably the streamlines of both flows and the use of the Davidson's model is justified. Collins (1989) following a similar reasoning developed also analytical expressions for both stream functions (although retaining only the firsts terms of the infinite sum) and justified the incompressible assumption in Davidson's model. The conclusions obtained in these previous works for circular bubbles are

consistent with the results in the present work for bubbles with a truncated ellipse geometry.

In addition, Collins (1989) found that the increase in the gas flow crossing a circular bubble because of the change in the voidage is only 1.5%. This modest increase contrasts with the higher value of 20% obtained in this work. Nevertheless, Collins (1989) assumed a voidage at the bubble contour of $\epsilon_{bc} = 0.439 = 1.10\epsilon_{mf}$, while a value of $\epsilon_{bc} = 0.665 = 1.66\epsilon_{mf}$ is experimentally determined in the present work, which lies behind the higher value of the throughflow crossing the bubble. Also Gera and Gautam (1994) applied Jackson's model (Jackson, 1963) on elliptical bubbles and observed an increase of the flow crossing the bubble with both bubble aspect ratio and voidage at the nose of the bubble.

However, not only the increase in the voidage around bubbles increases the flow crossing them. Also the geometry of the bubble plays an important role in the gas flow. The gas flow obtained from equation (4.16), i.e. 4.53, can be compared with the one obtained for a circular bubble with a radius $R_b = B$ (Davidson and Harrison, 1963), i.e.:

$$\frac{q_b}{U_0 \cdot R_b} = 4 \tag{4.18}$$

or for non-truncated ellipse of aspect ratio A/B (Grace and Harrison, 1969), that is,

$$\frac{q_b}{U_0 \cdot B} = 2 \cdot \left(1 + \frac{A}{B}\right) = 4.66 \tag{4.19}$$

Thus, the gas crossing a bubble of the same cross sectional area is higher for a truncated ellipse than for the circular one, as it is expected because of the higher aspect ratio. In contrast, the throughflow is lower for a truncated elliptical bubble than for a non-truncated geometry. In addition, the interface area (length, in a 2-D bed) between the bubble and the dense phase seems to influence the throughflow too. A higher interface area implies a higher throughflow.

On the other hand, the voidage distribution obtained in this work has not radial symmetry, as it was supposed by Collins (1989) and Buyevich et al. (1995) in equations (4.1) and (4.2) respectively. This fact is the result of the instabilities appearing at the nose of the bubbles, which gives the rain of particles in the form of the typical "stalactites". As a result, the value of $k_1(\theta)$ in equation (4.4) was higher in the bottom region of the bubble where these instabilities do not appear. Moreover, the maximum value of $k_1(\theta)$ is reached at $\theta = -\pi/3,\ -2\,\pi/3$ where the change in the bubble geometry occurs and also where the gas flow crossing the bubble contour is maximum.

In conclusion, a new method for measuring voidage distribution around bubbles in a 2-D fluidized bed has been presented. This method permits to obtain voidage

contours in the region very close to the bubble ($r/R_b \lesssim 1.2$) where previous techniques employed by other researchers (Lockett and Harrison, 1967; Nguyen et al., 1973) had no enough spatial resolution. The results obtained indicate the existence of a very narrow region around the bubble where ϵ decreases rapidly according to equation (4.4) with the values of $k_1(\theta)$ showed in table 4.1 and figure 4.9. In addition, a mean value of $\bar{\epsilon}_{bc} = 0.665$ for the voidage at the bubble contour was obtained for a set of more than 100 bubbles obtained from experiments carried out with two different particles sizes. Finally, numerical modeling indicates that this higher voidage region surrounding the bubble results in an increase of the throughflow crossing the bubble in a 20% with the representative bubble geometry of the 116 bubbles analysed.

4.7 Notation

A Mayor semiaxis of the ellipse $[31.2 \cdot 10^{-3} m]$

B Minor semiaxis of the ellipse $[23.5 \cdot 10^{-3} m]$

D Half of the length of the bubble's flat wake $[16.0 \cdot 10^{-3} m]$

d_p Particle diameter $[m]$

$\boldsymbol{g}$ Gravity $[m/s^2]$

$G.L.$ Grey level $[-]$

I Light intensity $[cd]$

I_0 Intensity of the incident light $[cd]$

K_e Permeability of the emulsion defined in equation (4.15) $[m^2]$

K_b Permeability of the bubble interior $[m^2]$

k_1 Constant defined in equation (4.4) $[-]$

k_2 Constant defined in equation (4.1) $[-]$

p_f Fluid pressure $[Pa]$

q_b Gas flow crossing the bubble $[m^2/s]$

R_b Bubble radius $[m]$

r Radial distance from the center of the bubble $[m]$

U Superficial gas velocity $[m/s]$

U_0 Superficial gas velocity far way from the bubble $[m/s]$

U_b Gas velocity crossing the bubble $[m/s]$

$\boldsymbol{u}$ Gas velocity $[m/s]$

$\tilde{\boldsymbol{u}}$ Relative gas velocity $[m/s]$

$\boldsymbol{v}$ Particle velocity $[m/s]$

β Function that defines the drag force $[kg/\left(s \cdot m^3\right)]$

ϵ Voidage $[-]$

ϵ_b Mean voidage at the bubble interior $[-]$

ϵ_{bc} Voidage at the bubble contour $[-]$

ϵ_{mf} Voidage at minimum fluidization conditions $[-]$

θ Angle formed with the horizontal $[rad]$

μ Gas viscosity $[Pa \cdot s]$

ρ_p Particle density $\left[\frac{kg}{m^3}\right]$

ϕ Particle sphericity $(= 1)$ $[-]$

$(\,)_-$ Inside surface of the bubble

$(\,)_+$ Outside surface of the bubble

Bibliography

Almendros-Ibáñez J.A., Sobrino C., de Vega M. and Santana D., 2006. A new model for ejected particle velocity from erupting bubbles in 2-D fluidized beds. *Chemical Engineering Science*, vol. 61, pp. 5981-5990

Benveniste D.E., Kinrys S. and Qassim R.Y., 1983. Flow past the fluidization bubble: effect of voidage variation, in: D. Kunii D., R. Toei (Eds.), *Fluidization 4*, Engineering Foundation, New York, pp. 9-14

Boerefijn R., Ghadiri M., 1998. High speed video image analysis of flow of fine particles in fluidized bed jets. *Advanced Powder Technology*, vol. 9, pp. 229-243

Buyevich Y.A., Yates J.G., Cheesman D.J. and Wu K.T., 1995. A model for the distribution of voidage around bubbles in a fluidized bed. *Chemical Engineering Science*, vol. 50, pp. 3155-3162

Collins R., 1989. A model for the effects of the voidage distribution around a fluidization bubble. *Chemical Engineering Science*, vol. 44, pp. 1481-1487

Croxford A.J., 2006. Investigation of dynamics and control of fluidised beds using pressure measurements. PhD thesis, University of Bristol

Davidson J.F., 1961. Symposium on fluidisation-Discussion. *Transactions of the Institution of Chemical Engineers*, vol. 39, pp. 230-232

Davidson J.F. and Harrison D., 1963. *Fluidised particles*. Cambridge University Press

Duru P., Guazzelli E., 2002. Experimental investigation on the secondary instability of liquid-fluidized beds and the formation of bubbles. *Journal of Fluid Mechanics*, vol. 470, pp. 359-382

Ergun S., 1952. Fluid flow through packed columns. *Chemical Engineering Progress*, vol. 48, pp. 89-94

Gera D. and Gautam M., 1994. Effect of voidage variation and bubble aspect ratio on throughflow in 2-D elliptical bubbles. *Powder Technology*, vol. 79, pp. 159-165

Goldschmidt M.J.V., Link J.M., Mellena S. and Kuipers J.A.M., 2003. Digital image analysis measurements of bed expansion and segregation dynamics in dense gas-fluidised beds. *Powder Technology*, vol. 138, pp. 135-159

Gonzales-Barron U., Butler f., 2006. A comparison of seven thresholding techniques with the k-means clustering algorithm for measurement of bread-crumb features by digital image analysis. *Journal of Food Engineering*, vol. 74, pp. 268-278

Grace J.R. and Harrison D., 1969. The behaviour of freely bubbling fluidised beds. *Chemical Engineering Science*, vol. 24, pp. 497-508

Jackson J.R., 1963. The mechanics of fluidised beds: Part II: The motion of fully developed bubbles. *Transactions of the Institution of Chemical Engineers*, vol. 41, pp. 22-28

Lockett M.J. and Harrison D., 1967. The distribution of voidage fraction near bubbles rising in gas-fluidized beds, in: A.A.H. Drinkenburg (Ed.), *Int. Symp. on Fluidization*, Netherlands University Press, Amsterdam, pp. 257-267

Murray J.D., 1965. On the mathematics of fluidization. Part 2. Steady motion of fully developed bubbles. Journal of Fluid Mechanics, vol. 22, pp. 57-80

Nguyen X.T., Leung L.S. and Weiland R.H., 1973. On void fractions around a bubble in a two dimensional fluidized bed, in: H. Angelino, J.P. Couderc, H. Gilbert, C. Lagarie (Eds.), *Proc. Int. Cong. Fluidization and its Applications*, Toulouse, pp. 230-239

Otsu N., 1979. A threshold selection method from gray-level histograms, *IEEE Transactions on Systems Man and Cybernetics*, vol. 9, pp. 62-66

Poletto M., Bai R., Joseph D.D., 1995. Propagation of voidage waves in a two-dimensional liquid-fluidized bed. *International Journal of Multiphase Flow*, vol. 21, pp. 223-239

Qassim R.Y., Kinrys S. and Benveniste D.E., 1989. Effect of voidage variation on flow past a fluidisation bubble. *Chemical Engineering Science*, vol. 44, pp. 1307-1313

Rowe P.N. and Partridge B.A., 1965. An x-ray study of bubbles in fluidised beds, *Transactions of the Institution of Chemical Engineers*, vol. 43, pp. 157-175

Russ J.C., 1994. *The Image Procesing Handbook*, 2nd edition. CRC Press

Santana D., Nauri S., Acosta A., García N. and Macías-Machín A., 2005. Initial particle velocity spatial distribution from 2-D erupting bubbles in fluidized beds. *Powder Technology*, vol. 150, pp. 1-8

Santana D., Rodríguez-Rodríguez J., Almendros-Ibáñez J.A. and Martínez-Bazán C., 2006. Characteristic lengths and maximum entropy estimation from probe signals in the ellipsoidal bubble regime. *International Journal of Multiphase Flow*, vol. 32, pp. 1123-1139

Stewart P.S.B., 1968. Prediction of voidage fraction near bubbles in fluidised beds. *Chemical Engineering Science*, vol. 23, pp. 396-397

Toomey R.D. and Johnstone H.F., 1952. Gaseous fluidization of solid particles. *Chemical Engineering Progress*, vol. 48, pp. 220-226

Yates J.G., Cheesman D.J. and Sergeev Y.A., 1994. Experimental observations of voidage distribution around bubbles in a fluidized bed. *Chemical Engineering Science*, vol. 49, pp. 1885-1895

Chapter 5

Experimental observations on the different mechanisms for solid ejection in gas-fluidized beds

Contents

5.1 Abstract

This work presents an experimental study of the ejection velocity for different mechanisms of solid ejection in fluidized beds. The experiments were carried out in a 2-D fluidized bed, where the bubble eruptions were recorded with a frequency of 250 frames per second using a high speed video-camera with a resolution of 1.3 Megapixels.

The results show that in isolated bubble eruption, the dome velocity is significantly reduced by the effect of a group of raining particles in the form of stalactites within the bubble. Higher velocities are observed when bubble coalescence takes place. If bubbles coalesce before the leading bubble breaks, the momentum of the trailing bubble together with the increase in the throughflow accelerate the dome of the leading bubble. In contrast, when coalescence occurs after the breakage of the leading bubble, the wake of the trailing bubble is projected into the freeboard with a very high velocity (wake spike mechanism). The last observed mechanism, the jet spike mechanism, occurs when a stream of bubbles reaches the bed surface following the path opened by the previous bubbles. A cloud of particles moving upward is observed, although their velocities are not as high as in the wake spike mechanism due to the interchange of momentum during the collisions with other particles.

5.2 Introduction

Entrainment and/or elutriation are important phenomena in fluidized beds. Entrainment refers to the total flux of bed material carried out of the bed while elutriation is the outward flux of solids of a specific size, typically fine particles. Although in chemical reactors the chemical reactions or the dryer process could occur mainly in the dense phase, the freeboard usually takes up most of the bed volume in industrial units (Werther and Hartge, 2003). The height of the freeboard is usually chosen to prevent the loss of a large amount of bed material by the gas flow, although in some cases, the height of the freeboard could be determined by other factors. For example, the height could be controlled by the need to have enough gas residence time to complete the reactions in biomass gasifiers (Devi et al., 2003; Ross et al., 2007) or to control the particle flux for the proper design of separation equipments such as cyclones and filters (Santana et al., 1999).

Regarding particle entrainment, the flux of elutriated particles of size d_{p_i} can be defined as

$$E_i = \frac{\int_A \overline{\rho_i} \cdot v_i \cdot dA}{\int_A dA}, \tag{5.1}$$

where $\overline{\rho_i} = (1-\epsilon)\cdot\rho_p$ is the mass of solids of size d_{p_i} per bed volume at one determined height, v_i is the upward velocity and A is the cross sectional area of the bed. Therefore, the total mass of solids carried out is

$$E = \sum_i E_i \tag{5.2}$$

The entrainment flux varies with height over the bed surface h. Kunii and Levenspiel (1990) represented the complex phenomena of the particle flow in the freeboard with a simple model in which the solids are divided into three phases: dispersed solids moving up, agglomerates of solids moving up and agglomerates and a thin-walled layer of particles moving down. In this way, E varies exponentially with h according to

$$\frac{E - E_\infty}{E_0 - E_\infty} = \exp\left(-a \cdot h\right) \tag{5.3}$$

where the constant a can be estimated as $a \approx 4\,m^{-1}$ if no detailed information is available (Wen and Chen, 1982), and E_∞ and E_0 represent the flux of solids elutriated from a very tall bed and the flux projected from the bed surface, respectively.

The flux E_∞ can be defined as the flux of particles that have a terminal velocity u_t lower than the superficial gas velocity U, although experimental results show some discrepancies (Werther and Hartge, 2003). The height over the bed surface at which the flux of particles is equal to E_∞ is known as the Transport Disengaging Height (TDH). If the height of the bed H is longer than the TDH, the flux of solids elutriated does not vary with h and is equal to E_∞. Different correlations can be found in the literature to calculate E_∞, although differences of one order of magnitude can be observed between them. A summary of the most common correlations expressed in SI units can be found in Werther and Hartge (2003).

At the bed surface, the initial flux of ejected particles E_0 depends on the mean density at that level, which can be approximated as $\overline{\rho_{i0}} = (1 - \epsilon_{mf}) \cdot \rho_p$ (Chen and Saxena, 1978; Pemberton and Davidson, 1986; Smolders and Baeyens, 1997), and on the particle ejection velocity v_0, which is related with the bubble velocity (Hatano and Ishida, 1981; Levy et al., 1982; Almendros-Ibáñez et al., 2006). There are fewer experimental studies in the literature about E_0 because of the difficulty of accurately measuring this flux. Pemberton and Davidson (1986) extrapolated the E_0 equation (5.3) to $h = 0$ using experimental data of different researchers, although this process of obtaining E_0 is not very accurate due to the uncertainty in the exact position of $h = 0$ in a bubbling bed. Wen and Chen (1982) developed an expression for E_0 by adjusting the following equation to data from different studies:

$$E_0 = 3.07 \cdot 10^{-9} \frac{\rho_g^{3.5}\, g^{0.5}}{\mu^{2.5}}\, A\, D_b\, \left(U - U_{mf}\right)^{2.5} \tag{5.4}$$

Some years later, Choi et al. (1989) extended equation (5.4) including the influence of bed temperature on the flux of particles E_0.

However, equation (5.4) does not take into account the origin of the projected

particles. Several theories have been discussed over the years about the origin of the projected particles. Some authors consider the bubble roof (or bubble dome/nose) as the dominant mechanism (Zenz and Weil, 1958; Chen and Saxena, 1978; Saxena and Mathur, 1984) while others suggest that most of the elutriated particles come from the bubble wake (Yates and Rowe, 1977; George and Grace, 1978; Briens et al., 1988). Pemberton and Davidson (1986) developed two different models of particle ejection: from the roof and from the wake of the bubble. They showed how the wake model predicts values of E_0 one order of magnitude higher than the roof model for the same superficial gas velocity, and they concluded that for group B particles with $U/U_{mf} < 10 - 15$ the roof model is suitable, while for group A particles and group B with $U/U_{mf} > 10 - 15$, the projection from the wake dominates due to the increase of bubble coalescence at the bed surface. In contrast, the Smolders and Baeyens model (Smolders and Baeyens, 1997) predicts much higher values of E_0 assuming that the particles are projected from the bubble roof, in contrast with the results of Pemberton and Davidson.

Therefore, the ejection mechanisms and the origin of the elutriated particles in fluidized beds are still not completely understood. Moreover, the mechanisms of solid ejection from the bed surface are not only the bubble roof and bubble wake. Levy et al. (1983) undertook an extensive study about the different mechanisms for solid ejection in 2-D and 3-D fluidized beds and observed four different mechanisms:

1. *Bulge bursting mechanism*, the most common. The bulge layer is projected when the bubble reaches the bed surface, whereas the height attained by the particles is somewhat less than the bubble diameter and the bubble wake remains intact.

2. The *double bubble mechanism* occurs when two bubbles coalesce at the bed surface and the middle layer of solids between the leader and the trailing bubble is projected together with the leading bulge.

3. The *wake spike mechanism* occurs when two or more bubbles coalesce at the bed surface and the wake of the trailing bubble is projected in the form of a spike.

4. The *jet spike mechanism* occurs when two or more bubbles coalesce at the bed surface and the bubbles form a flow passage that transports solids from the bed, projecting them into the freeboard.

The last three mechanisms are related to bubble coalescence. Although they are less frequent (Levy et al., 1983), the velocity of the projected particles when coalescence occurs is higher than in isolated bubbles (Hatano and Ishida, 1981).

This work tries to clarify some aspects of the different mechanisms for solid ejection observed by Levy et al. (1983). In particular, this article is focused on the particle ejection velocity, which has been observed to be much higher when bubble coalescence is involved. Therefore, the particles projected with these mechanisms, although they are less frequent, could attain higher heights in the freeboard and consequently could be the main cause of elutriation and entrainment.

In the remainder of the paper, the experimental set-up will be briefly described. Then, different mechanisms of solids ejection will be analysed in this order: isolated bubbles, two coalescing bubbles, wake spike and jet spike. Finally, the main conclusions of the work will be presented.

5.3 Experimental set-up

The experiments were carried out in a 2-D fluidized bed ($110\,cm$ width $\times$ $60\,cm$ height $\times$ $0.5\,cm$ thickness) made with two glass-walls that allow the user to see its interior. The bed was illuminated with two $650\,W$ spot-lights from the front of the bed, with a dark background at the rear in order to attain high contrast between the white particles and the regions free of particles (bubbles and freeboard). Bubble eruptions at the bed surface were captured using a high speed video camera with a resolution of $1280 \times 1024 = 1.3$ Megapixels. The pictures were captured from the central region of the bed at a rate of $250\,fps$, although the exposure was only $1/5000\,s$ in order to properly detect the bubble contour and prevent blurring due to the bubble motion.

Spherical glass particles with a mean particle diameter of $350\,\mu m$ and a density of $2500\,kg/m^3$ (type B according to Geldart's classification (Geldart, 1973)) were fluidized with air. The height of the fixed bed was approximately $30\,cm$, and the superficial gas velocity during the experiments was varied between $1 \leq U/U_{mf} \leq 2$. Higher velocities were avoided in order to prevent the entrainment of solids from the bed.

5.4 Isolated bubble eruption. The stalactite effect

When an isolated bubble reaches the bed surface, it projects the solids from the dome formed during the eruption process. Usually, the bubble wake is not projected unless there is another bubble of similar or higher size coalescing bellow when the leading bubble breaks the bed surface.

Before obtaining the initial particle velocity of the ejected particles, the instant when the bubble breaks the bed surface needs to be determined. There is no general agreement on the definition of this time. Pemberton and Davidson (1986) assumed that

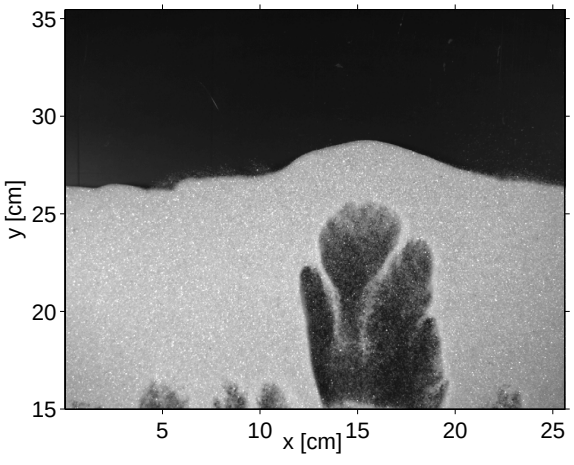

(a) $t = 0\,ms$

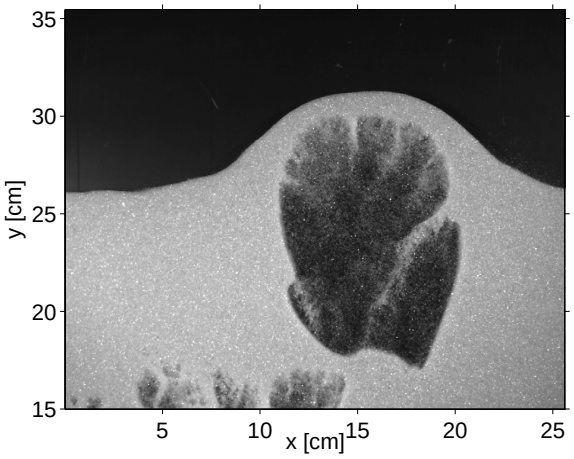

(b) $t = 56\,ms$

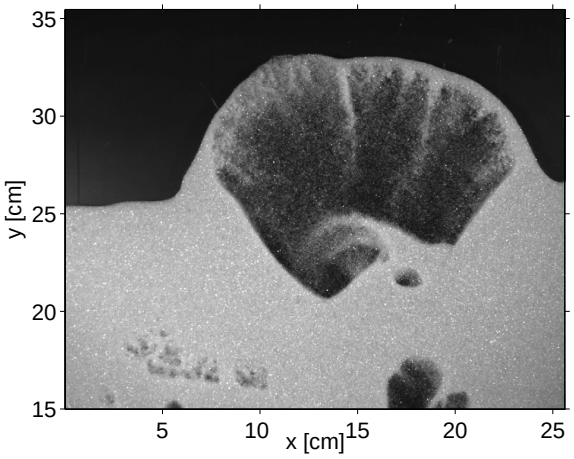

(c) $t = 124\,ms$

Figure 5.1: Evolution of one isolated bubble breaking at the bed surface.

the bubble dome is projected into the freeboard when the dome thickness is equal to the particle diameter. In contrast, in 2-D fluidized beds, the dome thickness is typically much higher than the particle size (Saxena and Mathur, 1984; Almendros-Ibáñez et al., 2007). Müller et al. (2007) defined the eruption instant as the time when the vertical velocity of the dome nose reaches its maximum, which corresponds approximately to a ratio between the dome thickness and the particle diameter of $\delta/d_p \sim 3$ under their experimental conditions. Santana et al. (2005) and Almendros-Ibáñez et al. (2006) defined the eruption instant as the time when the bubble interior and the freeboard join at some point of the bubble dome. The same criteria will be followed in this work. The evolution of the external surface of the bubble dome will be followed during the eruption process until the bubble dome breaks at a certain point due to the instabilities that appear before its breakage.

Figure 5.1 shows three frames of one isolated bubble erupting at the bed surface. At $t = 0\,ms$ the bubble approximates the bed surface forming the typical dome. Then, $56\,ms$ later, the nose of the bubble is over the mean bed height and the external surface of the dome is still smooth. At $t = 124\,ms$, the bubble dome breaks the bed surface. The dome contour at this moment is not smooth, and irregularities appear due to the effect of the stalactites, which funnel the particles situated in the bubble dome. A similar eruption process was observed Müller et al. (2007) for isolated injected bubbles.

In order to follow the evolution of the dome contour, the grey pictures were transformed into black and white pictures with a threshold value obtained according to Otsu (1979). Then, the external surface of the dome formed during the bubble eruption was followed until the dome breaks at a certain point. Figure 5.2(a) shows the evolution of the external surface of the dome during the bubble eruption process for the isolated bubble shown in figure 5.1. The evolution is captured during 32 consecutive frames ($128\,ms$). The contour of the dome is smooth in the first 20-25 frames. Then, some irregularities appear in the central region of the dome, where the particle displacement is vertical. Finally, the dome collapses and the bubble breaks.

The irregularities in the dome contour are caused by the rain of particles in the interior of the bubbles in the form of stalactites, which can divide the bubble in two (Rowe and Partridge, 1965). The effect of these stalactites on the bubble dome becomes more important as the dome thickness decreases. Figure 5.1(b) shows one stalactite at the bubble nose, which funnels the particles situated between the bubble contour and the free surface of the bed, although the free surface of the bed is not affected by this rain of particles and it remains smooth. In contrast, as the bubble ascends and the dome thickness decreases, the particles at the external surface of the dome are funneled by the stalactite, and the irregularities appear at the contour of the dome.

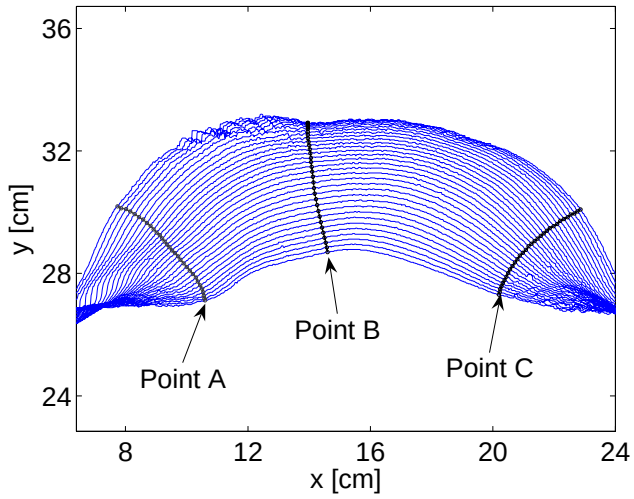

(a)

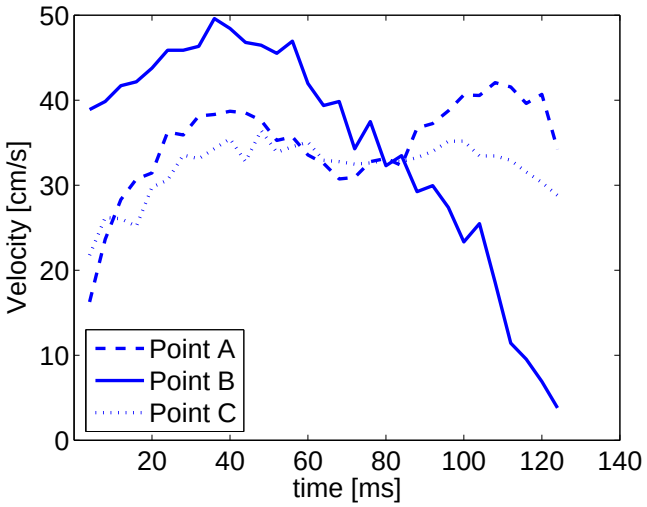

(b)

Figure 5.2: (a) Evolution of the external surface of the bubble dome with a time delay of $4\,ms$ between contours and (b) velocity of the points A, B and C.

The stalactite influence can be observed more clearly plotting the particle velocity at the dome contour. Figure 5.2(b) shows the velocity of one point situated at the nose of the dome (point B) and another two points (points A and C) located at the edges of the dome. The velocity is obtained by tracing the perpendicular to the dome contour from the initial point. The intersection of this line with the contour of the next frame defines the displacement between frames. The velocity of point B is vertical, although the velocity of points A and C have an appreciable horizontal component, especially during the last several frames. Point B accelerates until $t = 40\,ms$, when it reaches its maximum velocity and then decelerates with a rate of approximately $\sim -7\,m/s^2$. In contrast, points A and C, which are not directly affected by the stalactite, show a

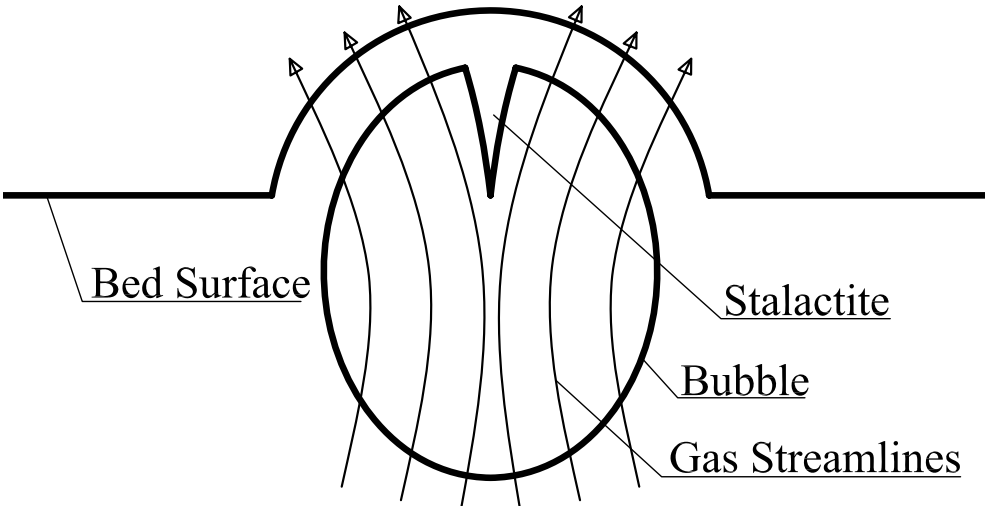

Figure 5.3: Scheme of the gas streamlines when one isolated bubble erupts at the bed surface with a group of particles raining in the form of a stalactite.

different evolution. They initially accelerate as point B does until $t = 40\,ms$. Then, their velocity seems to decrease slightly, but they finally accelerate again and maintain their velocity over $30\,cm/s$.

The rain of particles in the form of stalactites at the bubble nose suggests that the flow of air crossing the bubble (throughflow) deviates its path. Since the throughflow cannot drag the particles of the stalactite, the flow deviates and drags the particles situated at the sides of the dome, which are projected with higher velocities than the particles situated at the central region of the dome. Figure 5.3 shows a sketch of the process. Thus, in isolated erupting bubbles, whose dominant mechanism of particle ejection is the bulge bursting mechanism, when particles in the form of stalactites rain from the bubble dome, the vertical velocity of the particles is very low because of they are funneled by the stalactite. Higher velocities are reached by the particles situated at the edges, although their velocity has an appreciable horizontal component, and consequently, they have a low probability of reaching high heights in the freeboard.

Figure 5.4 shows more examples of isolated erupting bubbles, which all exhibit a similar behaviour. The points of the external surface of the dome situated over one stalactite (solids lines in figures 5.4(b), 5.4(d) and 5.4(f)) initially have a high velocity, although as the dome thickness decreases, they decelerate progressively until the dome breaks. In contrast, the points situated at the sides of the dome or between two stalactites (see point B in figure 5.4(e)), plotted in dotted lines in figures 5.4(b), 5.4(d) and 5.4(f) initially have a lower velocity. However, these points do not decelerate as much and maintain a higher velocity at the moment of eruption. In fact, some points even accelerate (point D in figure 5.4(b)).

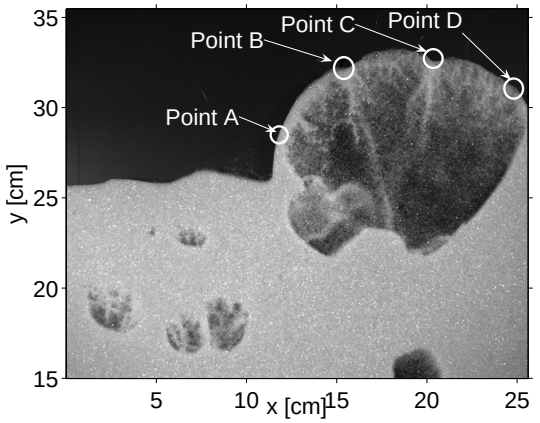

(a)

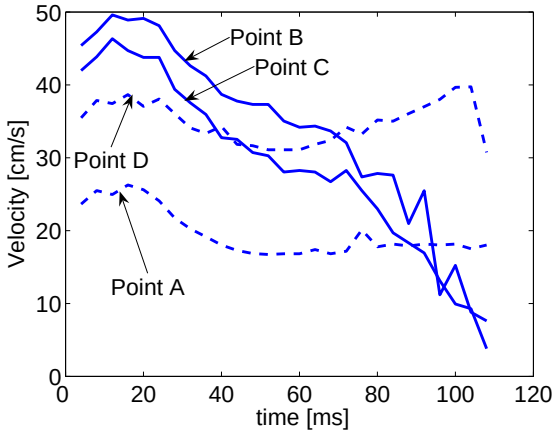

(b)

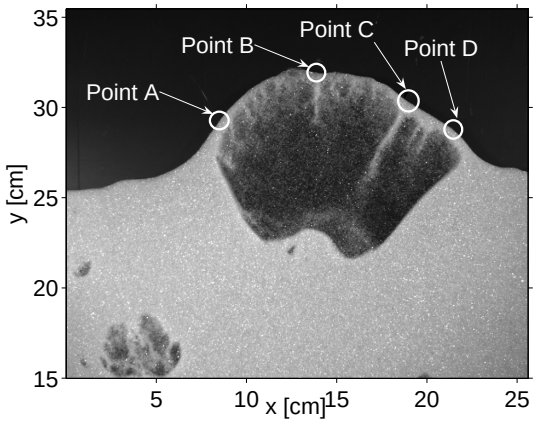

(c)

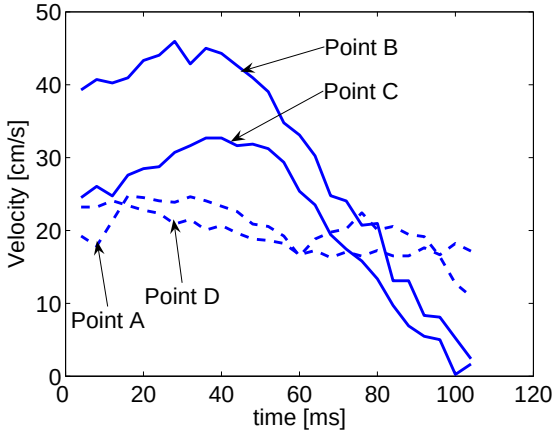

(d)

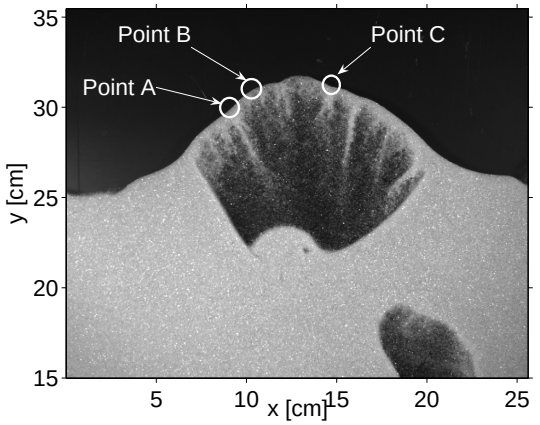

(e)

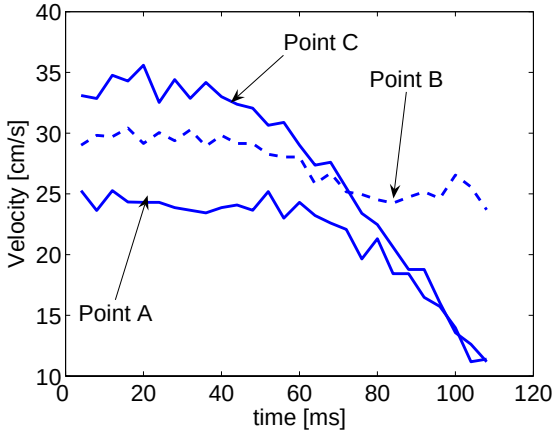

(f)

Figure 5.4: Some examples of isolated erupting bubbles: (a), (c) and (e) show the eruption instant and (b), (d) and (f) show the velocity of the points indicated in each figure during the eruption process.

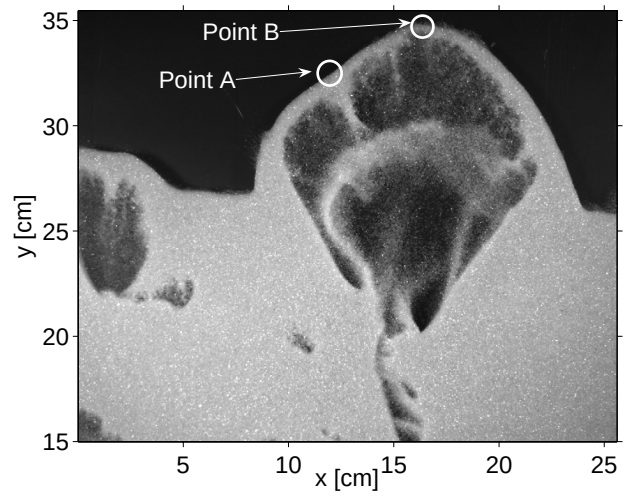

(a)

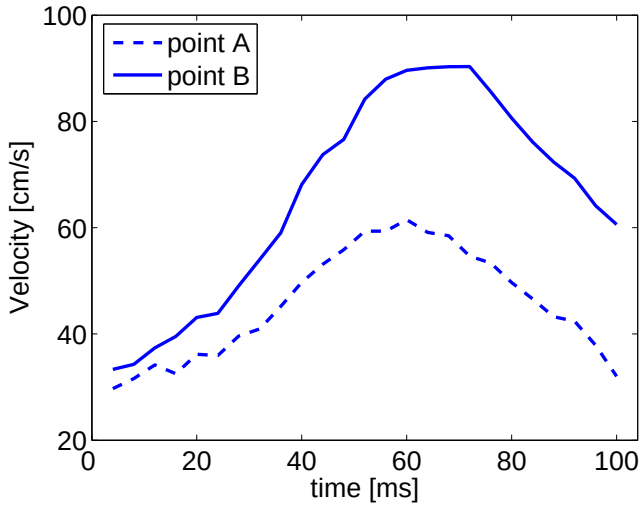

(b)

Figure 5.5: (a) Two bubbles coalescing at the bed surface and (b) velocity of the points A and B during the eruption process.

5.5 Two bubbles coalescing at the bed surface

When two bubbles coalesce while the leading one erupts at the bed surface, not only the middle layer of solids is projected to the freeboard. Also, the bulge of particles in the dome of the leading bubble is accelerated and projected at high velocities.

Figure 5.5 shows two bubbles coalescing at the bed surface when the leading bubble is erupting. Point A is situated just over one stalactite, while point B is on the bubble nose. Unlike the case of one isolated bubble, in this case the bubble dome is accelerated notably by the momentum transferred by the trailing bubble. The coalescence takes place at $t \approx 20\,ms$, the time when the slope of both lines changes. Point A accelerates

until $t \approx 60\,ms$, when it reaches its maximum velocity and then decelerates until a velocity approximately equal to its initial one. Point B shows a similar evolution, although this reaches a higher velocity (almost 90 cm/s), and its final velocity is double the velocity at $t = 20\,ms$.

The dome of the leading bubble is not simply accelerated by the momentum transferred by the trailing bubble. When both bubbles coalesce, an elongated region that is highly permeable to gas flow is formed just under the bed surface. This cavity divers the gas trajectory and the gas reaches the freeboard crossing the bubble due to the more favourable pressure gradient. The throughflow increases with the bubble aspect ratio because the pressure gradient, which forces the gas to flow, also increases (Glicklsman and Yule, 1986). Thus, when two bubbles coalesce, a significant increase of the throughflow accelerates the particles of the bubble dome and projects them to the freeboard with higher velocities than in the isolated bubble mechanism.

5.6 Wake spike mechanism

The wake spike mechanism for solid ejection observed by Levy et al. (1983) typically occurs when two or more bubbles coalesce consecutively at the bed surface and the wake of the trailing bubble is projected into the freeboard in the form of a spike.

The three frames of figure 5.6 show the eruption of three consecutive bubbles. Two wake spikes are observed after the eruption of the second and the third bubbles. The first spike has a peculiar geometry, similar to the vortex ring formed from a nozzle during the injection of a water jet (van Dyke, 1982), while the second spike is more elongated and geometrically more similar to a spike. The bulge of particles between bubbles 1 and 2 are also projected to the freeboard (double bubble mechanism (Levy et al., 1983)), although this group of particles moving upward collides with the particles raining from the dome of the first bubble, which where previously projected. As a result, figure 5.6(b) shows a very irregular dome in the second bubble, the consequence of the collision of the two groups of particles moving in opposite directions. This effect is more important in 2-D geometries, where the movement in the third dimension is limited by the bed walls. In addition, the thickness of the bubble dome in 2-D beds at the instant of eruption seems to be wider than in 3-D beds (Saxena and Mathur, 1984; Almendros-Ibáñez et al., 2007); thus, the collision is more important.

Figure 5.7(a) and 5.7(b) respectively, show the velocity of the first and second wake spikes shown in figure 5.6. In both cases, the displacement of the nose of the spike is followed during the solid projection until it collides with the particles projected from the bubble dome. The results shown in figure 5.7 demonstrate that the ejection velocity

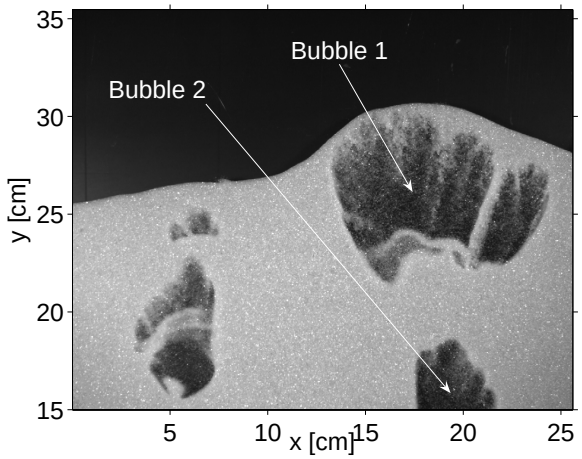

(a) $t = 0\,ms$

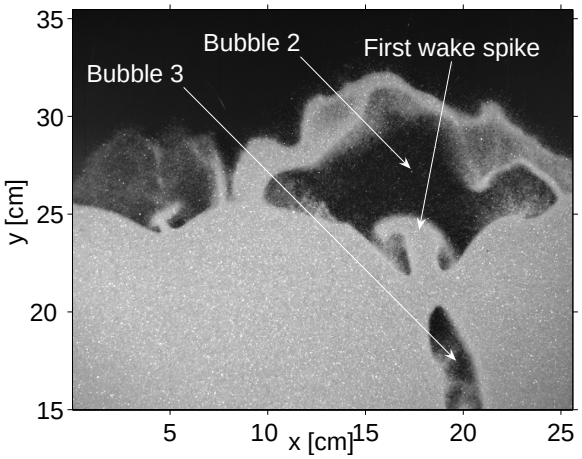

(b) $t = 152\,ms$

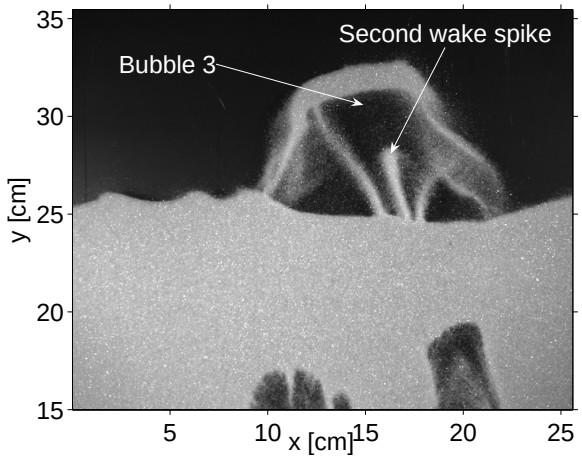

(c) $t = 272\,ms$

Figure 5.6: Three consecutive bubbles coalescing at the bed surface with two wake spikes between them.

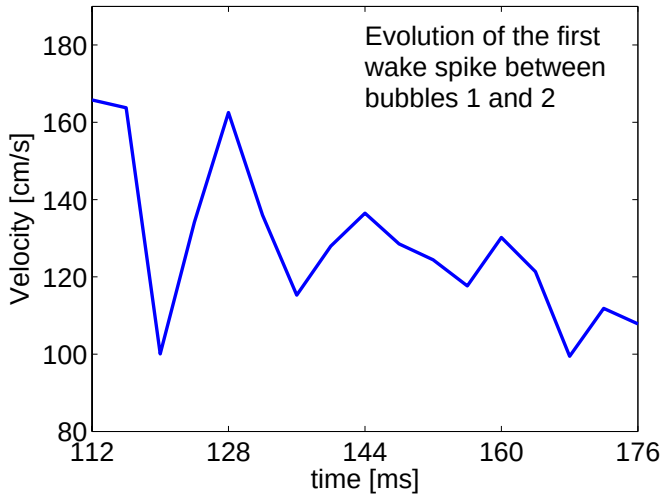

(a)

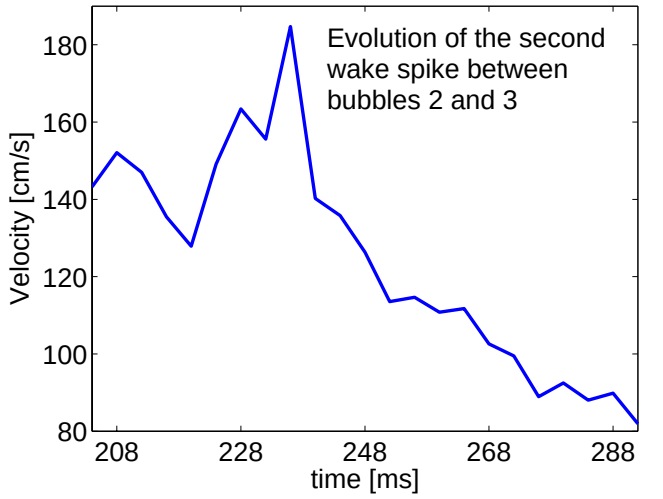

(b)

Figure 5.7: (a) Velocity of the first wake spike shown in figure 5.6(b) and (b) velocity of the second wake spike shown in figure 5.6(c).

in the wake spike mechanism is much higher than in isolated bubbles. The velocity of both spikes is over $1\,m/s$ during almost the entire ejection process, while in the case of isolated bubbles, the ejection velocity seldom exceeds $0.5\,m/s$. Even with two bubbles coalescing (figure 5.5(b)), the ejection velocity is lower.

The particle ejection velocity in the wake spike mechanism seems to be higher at the initial instant. Then, it decreases progressively until the spike reaches a height where it collides with the particles projected from the dome. The deceleration process is not smooth, and the velocity fluctuates during the ejection process. These irregularities are caused by the continuous rain of particles from the bubble dome.

5.7 Jet spike mechanism

In this solid ejection mechanism, the particles are not projected in a coherent group (a dome or a spike). Instead, the jet spike occurs when a stream of bubbles coalescing at the bed surface forms a channel through which particles are transported and projected from the interior of the bed to the freeboard. The solids form a continuous cloud of particles with a poorly defined geometry. Thus, in order to measure the velocity of the ejected particles in this mechanism, rather than follow the displacement of the contour of a well-defined geometry, Particle Image Velocimetry (PIV) will be used.

Different works can be found in the literature using PIV in granular flows (Lueptow et al., 2000), silo discharge (Böhrnsen et al., 2004; Ostendorf and Schewedes, 2005; Slominski et al., 2007) and fluidized beds (Santana et al., 2005; Müller et al., 2007). The same PIV software used by Müller et al. (2007) (MATPIV 1.6.1 (Sveen, 2004)) and the same iterative process and filters of this work were followed. Müller et al. (2007) used MATPIV 1.6.1 to measure the particle velocity around isolated injected bubbles erupting at the surface of a bed at minimum fluidization conditions. In this work, this software will be used to obtain the particle velocity field in the jet spike mechanism for solids ejection in a freely bubbling fluidized bed.

Figures 5.8 and 5.9 show a sequence of six frames captured during the ejection of solids by the jet spike mechanism. A total of 12 bubbles reached the freeboard through the channel opened at the bed surface during $0.7\,s$. The channel formed diverts the trajectory of most of the flow crossing the bed (either visible flow in the form of bubbles or throughflow) through the opened channel. This effect could cause defluidization in some regions of the bed, particularly in the vicinity of the jet, because the gas flow has been reduced under minimum fluidization conditions. This effect is similar to the one caused by the rat-holes that appear when type C particles are fluidized (Geldart, 1973). The ejection of solids is violent, and the dome and wake of one erupting bubble collides with the particles ejected by the previous ones. As a consequence, the ejected particle velocity is strongly influenced by the collision with other particles and the resulting interchange in momentum between them. Thus, the resulting velocity is not as high as would be expected by solely considering the high pressure gradient, which projects the particles to the freeboard. The highest velocities are observed when the particles moving down return to the bed (see figure 5.9(b)) and at some local points situated in the jet.

Figures 5.8 and 5.9 show the general behaviour of how the particles within the bed are pushed to the interior of the channel by the gas flow. Once the particles are inside the channel, these particles move upward, dragged by the gas flow until they are ejected

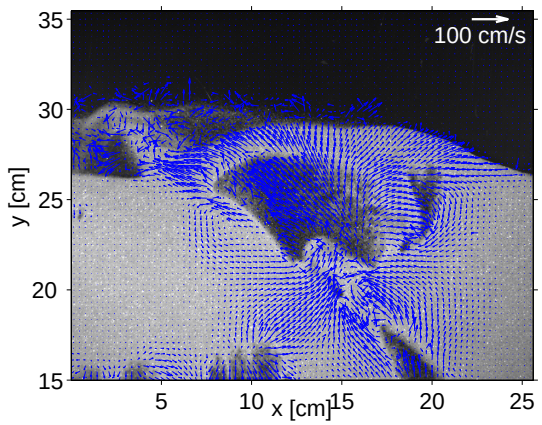

(a) t=0 ms

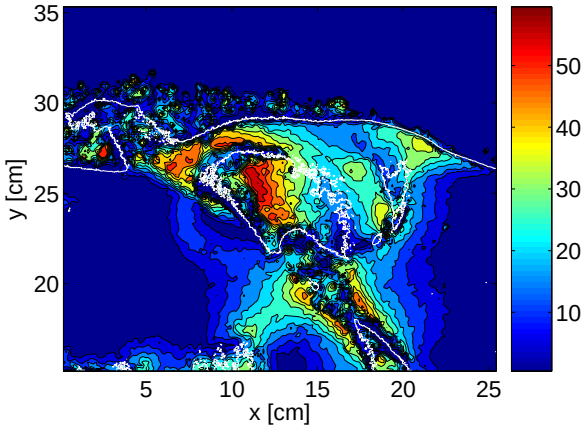

(b) t=0 ms

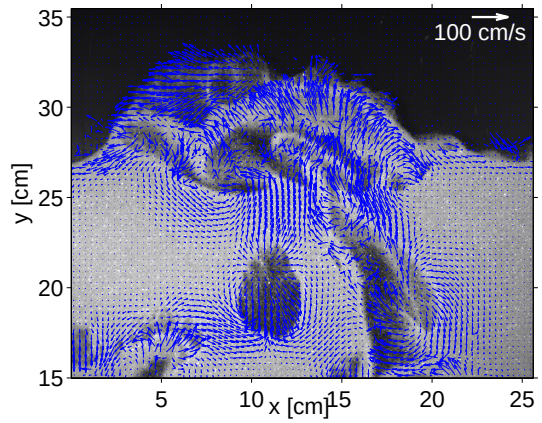

(c) t=116 ms

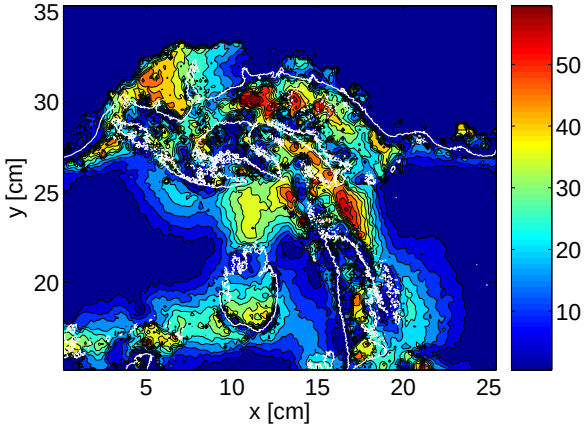

(d) t=116 ms

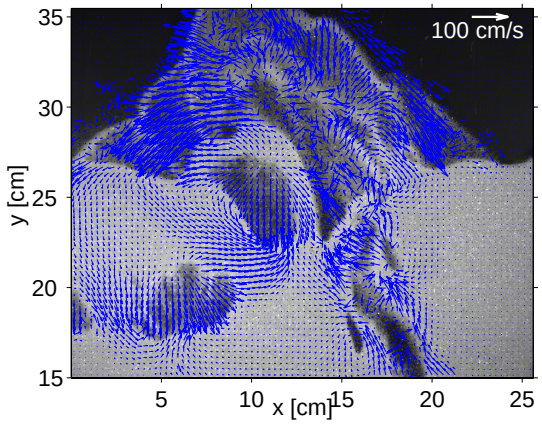

(e) t=220 ms

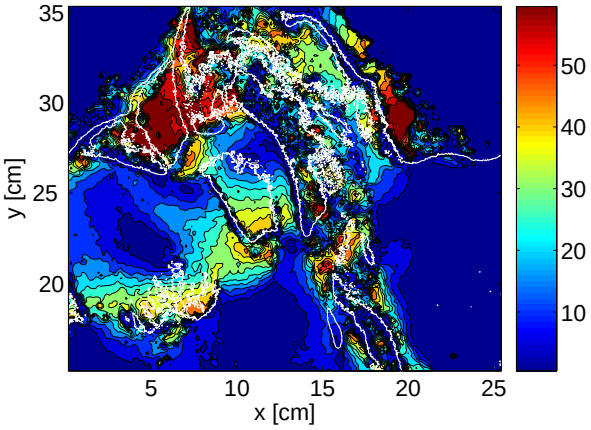

(f) t=220 ms

Figure 5.8: PIV results in a jet spike. Figures (a), (c) and (e) shows velocity vectors and (b), (d) and (f) velocity magnitude in cm/s.

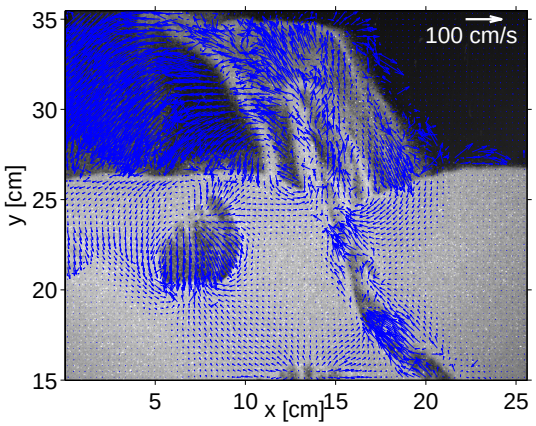

(a) t=332 ms

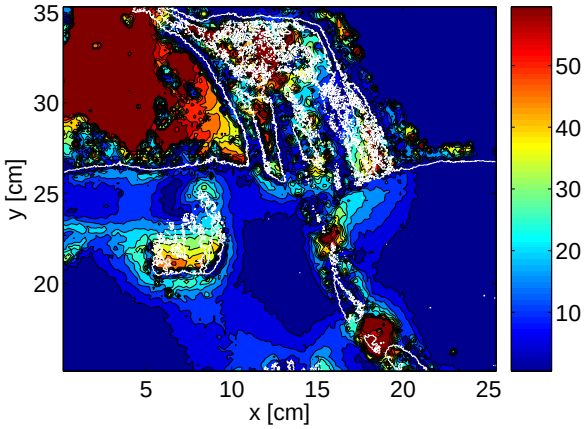

(b) t=332 ms

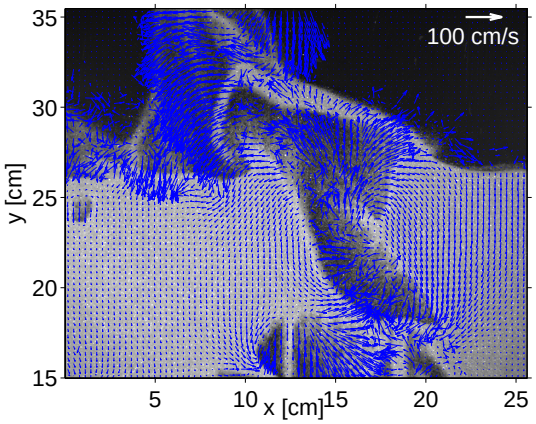

(c) t=460 ms

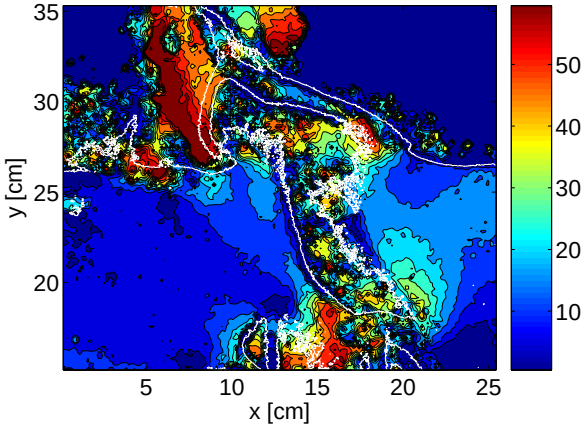

(d) t=460 ms

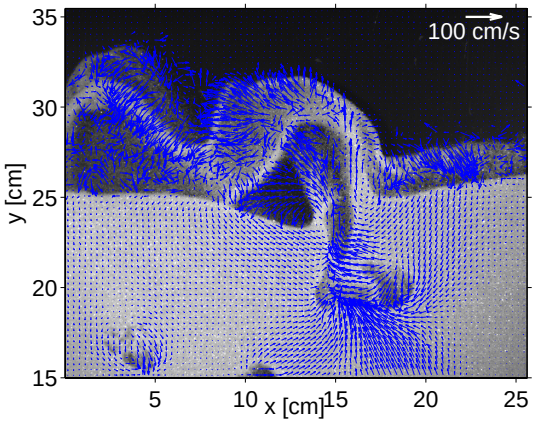

(e) t=584 ms

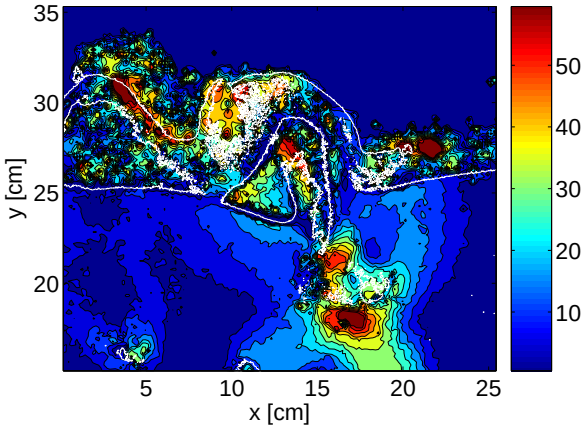

(f) t=584 ms

Figure 5.9: PIV results in a jet spike. Figures (a), (c) and (e) shows velocity vectors and (b), (d) and (f) velocity magnitude in cm/s.

into the freeboard. In contrast, the particles inside of other bubbles located at the left side of the jet (see figures 5.8(c) and 5.9(a)) move down because of the throughflow in these bubbles can not drag the raining particles. Müller et al. (2007) observed similar results in the interior of isolated injected bubbles erupting at the bed surface. They observed that the particle velocity is zero at a distance of approximately $D_b/4$ from the bubble top. The particles above that point move upward, while those located bellow it move downward. A similar behavior was observed in the bubbles not influenced by the jet in figures 5.8 and 5.9.

5.8 Discussion and conclusions

In this work, the particle ejection velocity for different ejection mechanisms has been observed in a 2-D bed. The evolution of the dome contour in isolated erupting bubbles, as well as in two coalescing bubbles, were tracked during the eruption process. In the wake spike mechanism the velocity of the nose of the spike was measured, and this mechanism had the highest ejection velocities. In the jet spike mechanism, PIV was used to measure the particle ejection velocity because a cloud of dispersed particles is observed rather than a group of particles with a well define shape.

In isolated erupting bubbles, groups of particles are observed raining in the form of stalactites within the bubble. This effect causes a deceleration in the particles situated just over the stalactites, which result in the typical instabilities at the contour of the bubble dome during the eruption process observed by Müller et al. (2007). In addition, the throughflow crossing the bubble cannot drag the raining particles, and thus, is deviated. Thus, the throughflow drags the particles located at the sides of the dome where the ejection particle velocity has an appreciable horizontal component.

The general behaviour is different when two or more bubbles coalesce. If the coalescence takes place when the leading bubble approaches the bed surface but still has not broken the bed surface, the momentum of the trailing bubble, together with the increase in the throughflow, accelerate the dome of the leading bubble, and consequently, the ejection velocity increases. In contrast, if coalescence occurs when the interior of the leading bubble is in contact with the freeboard (the dome is broken), then the wake spike mechanism appears: the wake of the trailing bubble is projected with a very high velocity.

In the jet spike mechanism, there is no group of particles with a well-defined geometry. In this mechanism, a cloud of particles is continuously ejected to the freeboard. Thus, the ejection velocity is not as high as in the wake spike mechanism because the momentum of the particles is notably reduced by collisions with other particles. The

channel formed during the process forces the bubbles, and also the invisible flow, to reach the freeboard through this channel, and defluidized regions could also appear in the bed.

Levy et al. (1983) concluded that around 90% of the more than 5000 erupting bubbles observed in 2-D and 3-D fluidized beds were isolated bubbles, and only in 10% bubble coalescence was involved. Nevertheless, although isolated erupting bubbles are more frequent, the ejection velocity of the solids projected by this mechanism is low. Moreover, when the stalactite effect appears, the vertical velocity of the ejected solids is notably reduced. Thus, the TDH, which can be defined as the highest height reached by the particles of largest size, should be obtained from the ejection mechanism in which higher velocities are observed.

In this work, the highest ejection velocities have been observed when bubble coalescence is involved, especially in the wake spike mechanism. In addition, this mechanism ejects particles from the wake of the bubble where the mean particle size is higher than in the bubble nose. Thus, the ejection velocity and the particle sizes are higher, and consequently the solids ejected by this mechanism will reach higher heights in the freeboard (Zenz and Weil, 1958; Do et al., 1972). The maximum height reached by the solids ejected by the wake and jet spike mechanisms cannot be observed experimentally due to the 2-D geometry of the experimental facility. The particle movement in the third direction is restricted by the walls of the bed. As a consequence, ejected solids collide with the solids ejected previously from the bubble dome or from previous bubbles before reaching the maximum height. Moreover, the dome thickness in 2-D beds is higher than in 3-D beds (Pemberton and Davidson, 1986; Almendros-Ibáñez et al., 2007).

In summary, the particle ejection velocity has been observed for different mechanisms of solids ejection. In isolated bubble eruption, the dome of the bubble is ejected to the freeboard, although these particles travel at low velocities due to the rain of particles within the bubble in the form of stalactites. When two or more bubbles coalesce, if the coalescence takes place before the leading bubble breaks, the momentum of the trailing bubble together with the increase in the throughflow crossing both bubbles accelerates the dome of the leading bubble. If coalescence occurs when the leading bubble has broken, the wake of the rear bubble is ejected at a very high velocity. Finally, the jet mechanism occurs when a stream of bubbles follows the path opened by the previous one. A cloud of particles moving upward is observed, although their velocity is notably reduced by their collision with other particles.

5.9 Notation

A Cross sectional area of the bed $[m^2]$

a Experimental constant in equation (5.3) $[m^{-1}]$

D_b Bubble diameter $[m]$

d_p Particle diameter $[m]$

E Flux of elutriated particles defined by equation (5.2) $[kg/(s \cdot m^2)]$

g Gravity constant $[9.81\, m/s^2]$

h Height measured over the bed surface $[m]$

U Superficial gas velocity $[m/s]$

u_t Terminal velocity of the particles $[m/s]$

v Particle velocity in the freeboard $[m/s]$

δ Thickness of the bubble dome at the eruption instant $[m]$

μ Dynamic gas viscosity $[(N \cdot s)/m^2]$

$\overline{\rho}$ Mass of particles per unit of bed volume $[kg/m^3]$

ρ_g Gas density $[kg/m^3]$

ρ_p Particle density $[kg/m^3]$

$(\ )_i$ Magnitude refereed to particles of size d_{p_i}

$(\ )_{mf}$ Magnitude refereed at minimum fluidization conditions

$(\ )_0$ Magnitude refereed at the bed surface $(h = 0)$

$(\ )_\infty$ Magnitude refereed at an height over the TDH

Bibliography

Almendros-Ibáñez J.A., Sobrino C., de Vega M. and Santana D., 2006. A new model for ejected particle velocity from erupting bubbles in 2-D fluidized beds, *Chemical Engineering Science*, vol. 61, pp. 5981-5990

Almendros-Ibáñez J.A., Sobrino C., Sánchez-Delgado S., Santana D., de Vega M. and Ruiz-Rivas U., 2007. Throughflow velocity crossing the dome of erupting bubbles, in X. Bi, F. Berruti, T. Pugsley, (Eds.), *Fluidization XII: New Horizons in Fluidization Engineering*, Engineering Conference International, New York, pp. 169-176

Böhrnsen J.U., Antes H., Ostendorf M. and Schwedes J., 2004. Silo discharge: measurement and simulation of dynamic behavior in bulk solids, *Chemical Engineering & Technology*, vol. 27, pp. 71-76

Briens C.L., Bergougnou M.A. and Baron T., 1988. Prediction of entrainment from gas-solid fluidized beds, *Powder Technology*, vol. 54, pp. 183-196

Chen T.P. and Saxena S.C., 1978. A theory of solids projection from a fluidized bed surface as a first step in the analysis of entrainment processes, in J.F. Davidson and D.L. Keairns (eds.), *Fluidization: Proceedings of the Second Engineering Foundation Conference*, Cambridge University Press, London, pp. 151-156

Choi J.H., Son J.E. and Kim S.D., 1989. Solid entrainment in fluidized bed combustors, *Journal of Chemical Engineering of Japan*, vol. 22, pp. 597-606

Devi L., Ptasinski K.J. and Janssen F.J.J.G., 2003 A review of the primary measures for tar elimination in biomass gasification processes. *Biomass and Bioenergy*, vol. 24, pp. 125-140

Do H.T., Grace J.R. and Clift R., 1972. Particle ejection and entrainment from fluidised beds, *Powder Technology*, vol. 6, pp. 195-200

Geldart D., 1973. Types of gas fluidization, *Powder Technology*, vol. 7, pp. 285-292

George S.E. and Grace J.R., 1978. Entrainment of particles from agregative fluidized beds, *AIChE Symposium Series*, vol. 74, pp. 67-74

Glicksman L.R. and Yule T., 1986. Gas throughflow in a bubbling fluidized beds, in K. Ostergaard, A. Sorensen (Eds.) *Fluidization V: Proceedings of the Engineering Foundation Conference*, Amer. Inst. of Chemical Engineers, Elsinore (Denmark), pp. 103-110

Hatano H. and Ishida M., 1981. The entrainment of solid particles from a gas-solid fluidized bed, *Journal of Chemical Engineering of Japan*, vol. 14, pp. 306-311

Kunii D. and Levenspiel O., 1990. Entrainment of solids from fluidized beds. I. Hold-up of solids in the freeboard. II. Operation of fast fluidized beds, *Powder Technology*, vol. 61, pp. 193-206

Levy E.K., Dille J.C. and Caram H.S., 1982. Single bubble eruptions in gas fluidized beds, *Powder Technology*, vol. 32, pp. 173-178

Levy E.K., Caram H.S., Dille J.C. and Edelstein S., 1983. Mechanims for solid ejection from gas-fluidized beds, *AIChE Journal*, vol. 29, pp. 383-388

Lueptow R.M., Akonur A. and Shinbrot T., 2000. PIV for granular flows, *Experiments in Fluids*, vol. 28, pp. 183-186

Müller C.R., Davidson J.F., Dennis J.S. and Hayhurst A.L., 2007. A study of the motion and eruption of a bubble at the surface of a two-dimensional fluidized bed using particle image velocimetry (PIV), *Industrial & Engineering Chemistry Research*, vol. 46, pp. 1642-1652

Ostendorf M. and Schewedes J., 2005. Application of particles image velocimetry for velocity measurements during silo discharge, *Powder Technology*, vol. 158, pp. 69-75

Otsu N., 1979. A threshold selection method from gray-level histograms, *IEEE Transactions on Systems Man and Cybernetics*, vol. 9, pp. 62-66

Pemberton S.T. and Davidson J.F., 1986. Elutriation from fluidized beds-I. Particle ejection from the dense phase into the freeboard, *Chemical Engineering Science*, vol. 41, pp. 243-251

Ross D., Noda R., Horio M., Kosminski A., Ashman P. and Mullinger P., 2007. Axial gas profiles in a bubbling fluidised bed biomass gasifier, *Fuel*, vol. 86, pp. 1417-1429

Rowe P.N. and Partridge B.A., 1965. An x-ray study of bubbles in fluidised beds, *Transactions of the Institution of Chemical Engineers*, vol. 43, pp. 157-175

Santana D., Rodríguez J.M. and Macías-Machín A., 1999. Modelling fluidized bed elutriation of fine particles, *Powder Technology*, vol. 106, pp. 110-118

Santana D., Nauri S., Acosta A., García N. and Macías-Machín A., 2005. Initial particle velocity spatial distribution from 2-D erupting bubbles in fluidized beds. *Powder Technology*, vol. 150, pp. 1-8

Saxena S.C. and Mathur A., 1984. On the origin of solids projected from the surface of a gas-fluidized bed, *Chemical Engineering Science*, vol. 39, pp. 917-918

Slominski C., Niedostatkiewicz M. and Tejchman J., 2007. Application of particle image velocimetry (PIV) for deformation measurement during granular flow, , *Powder Technology*, vol. 173, pp. 1-18

Smolders K. and Baeyens J., 1997. Elutriation of fines from gas fluidized beds: mechanims of elutriation and effect of freeboard geometry, *Powder Technology*, vol. 92, pp. 35-46

Sveen J.P., http://www.math.uio.no/∼jks/matpiv (Last modified in August, 2004. Accesed in 2008)

van Dyke M., 1982. *An album of Fluid Motion*, The Parabolic Press, 8th edn., p. 43

Wen C.Y. and Chen L.H., 1982. Fluidized bed freeboard phenomena: entrainment and elutriation, *AIChE Journal*, vol. 28, pp. 117-128

Werther J. and Hartge E.U., 2003. Elutriation and Entrainment, in W.C. Yang (ed.), *Handbook of fluidization and fluid-particle systems*, Marcel Dekker Inc., New York, pp. 113-128

Yates J.G. and Rowe P.N., 1977. A model for chemical reaction in the freeboard region above a fluidised bed, *Transactions of the Institution of Chemical Engineers*, vol. 55, pp. 137-142

Zenz F.A. and Weil N.A., 1958. A theoretical-empirical approach to the mechanism of particle entrainment from fluidized beds, *AIChE Journal*, vol. 4, pp. 472-479

Chapter 6

A new model for ejected particle velocity from erupting bubbles in 2-D fluidized beds

Contents

6.1 Abstract

A new model is proposed for obtaining the velocity profile of the particles ejected from the bubble dome in a freely bubbling 2-D fluidized bed. Its basis is the supposition that the initial velocity of the ejected particles (with a direction perpendicular to the dome contour) depends on bubble velocity and bubble growth velocity. This model differs from those previously appearing in the literature in that it is valid not only for vertical-ascent circular bubbles.

Experiments were carried out in a 2-D freely bubbling fluidized bed using a high speed video-camera to measure the velocity profile. Upon comparing these results

with the proposed model, it was established that, excepting some isolated cases, the model properly predicts the magnitude and direction of the maximum particle ejection velocity and the velocity profile.

Using the work of Shen et al. (2004), two general equations for the bubble velocity and the bubble growth velocity in a 2-D fluidized bed have been obtained. These expressions, together with the proposed model, can be used to calculate the initial velocity of the ejected particles.

6.2 Introduction

Fluidized beds are widely used in the industry as, among others, dryers, chemical reactors, biomass and coal combustors/gasifiers. They possess a high *reaction/volume* ratio due to high mixing and turbulence levels, thus creating a uniform temperature throughout the whole dense bed. For most of the industrial applications, the fluidized inert particles are group B, according to Geldart's classification (Geldart, 1973). With this type of particles, when the superficial gas velocity exceeds the minimum velocity for fluidization conditions, most of the excess gas traverses the dense bed in the form of bubbles.

Along their ascent, the bubbles undergo coalescence and ingest the surrounding air from the emulsion phase, thus causing them to grow. When a bubble erupts at the bed surface, it projects particles into the freeboard, although the particles' point of origin is unclear. Pemberton and Davidson (1986) proposed two ejection mechanisms: ejection from the bubble dome or ejection from the bubble wake. The former is predominant in the case of isolated erupting bubbles, while for high superficial gas velocities the wake mechanism becomes more important due to coalescence. In addition, the effect of the vessel walls is important because they mitigate wake ejection (Pemberton and Davidson, 1986), the result being a greater predominance of the dome mechanism in 2-D fluidized beds.

The projection of particles by the erupting bubbles into the freeboard is the main cause of their elutriation and/or entrainment (entrainment is defined as the total flux of solids leaving the bed, while elutriation refers to the separation of fines from a wide mix of particles). The mass of particles in the freeboard decreases exponentially from the bed surface up to the TDH (Transport Disengaging Height), which is one of the most important parameters in fluidized bed design. Beyond the TDH, entrainment is nearly constant. Some empirical correlations can be found in the literature for estimating this height, but they are largely uncertain (Werther and Hartge, 2003). To properly calculate the TDH, it is necessary to understand the process being undergone below it,

namely, the formation and disintegration of coherent structures like clusters, vortex or ghost bubbles, as well as the interaction between the particles and the gas turbulence (Pemberton and Davidson, 1984; Duursma et al., 2001; Solimene et al., 2004). These processes are influenced by bubble eruption, the projection and velocity of the ejected particles and the maximum height they reach.

In order to calculate the maximum height attained by the projected particles, some theories are proposed in the literature, based in the integration of the momentum equation for isolated or grouped particles (Do et al., 1972; Peters and Prybylowski, 1983; Demmich, 1984; Fung and Hamdullahpur, 1993) and based in the momentum transferred to the particles by the gas bubble (Pemberton and Davidson, 1986). Each of these theories requires the initial velocity of the ejected particles. For example, Peters and Prybylowski (1983) assumed a constant radial velocity normal to the dome contour, Demmich (1984) suggested that the initial particle velocity profile follows an exponential relationship and Fung and Hamdullahpur (1993) supposed a symmetric distribution, in which the magnitude of the velocity vectors decays linearly with the angle measured from the vertical direction. These three models proposed for the particle ejection velocity profile are only valid for vertical-ascent spherical bubbles (circular bubbles in 2-D fluidized beds) erupting isolated at the bed surface. They are obtained for single injected bubbles, and are difficult to extrapolate to erupting bubbles in a freely bubbling fluidized bed.

Therefore, a new model is presented for the velocity profile of the particles ejected from the bubble dome in these circumstances. This model, since it is proposed for a freely bubbling 2-D fluidized bed, is valid not only for vertical-ascent circular bubbles, but rather for all ascending directions including different bubble sizes and dome contours. Therefore, without disregarding its use for simple cases with vertical-ascent and/or circular bubbles, the model calculates the initial velocity of the particle ejected into the freeboard of a fluidized bed in conditions similar to real ones.

A cold 2-D fluidized bed, similar to the one described by Santana et al. (2005), is used in the experiments. The initial velocity of the particles projected from the dome was measured taking photographs with a high speed video-camera. The model was contrasted with the experimental results, and showed substantial agreement. Then, using the results of Shen et al. (2004), two equations were obtained for bubble velocity and bubble growth velocity in a 2-D freely bubbling fluidized bed. These equations, together with the proposed model, allow for the calculation of the velocity profile of the ejected particles.

6.3 Theoretical model

Different models appear in the literature for obtaining the velocity profile of the particles ejected from bubble eruption, though all of them are limited to vertical-ascent spherical bubbles. The first model was proposed by Peters and Prybylowski (1983), who assumed a constant radial velocity for all the particles. However, Santana et al. (2005) showed in their experiments that the velocity of the particles projected from the centre of the dome are higher than that of the particles located near the stagnation points; from this they established Fung's model (Fung and Hamdullahpur, 1993) as the most appropriated for their experimental conditions. Fung's model assumes that the magnitude of the radial particle ejection velocity decreases linearly with the angle θ, according to equation (6.1)

$$U_p = \begin{cases} U_{p,max}\left(\dfrac{\theta}{\frac{\pi}{2}}\right) & \text{if} \quad 0 \leq \theta \leq \frac{\pi}{2} \\ U_{p,max}\left(\dfrac{\pi-\theta}{\frac{\pi}{2}}\right) & \text{if} \quad \frac{\pi}{2} \leq \theta \leq \pi \end{cases} \tag{6.1}$$

where $U_{p,max}$ is the maximum particle ejection velocity and θ is the angle formed by the velocity vectors and the bed surface. For 3-D fluidized beds, this velocity is approximately two times the bubble velocity U_b (Pemberton and Davidson, 1986; Fung and Hamdullahpur, 1993). However, this simple model does not take into account two facts: (a) the bubble may not rise vertically, thus the maximum particle velocity vector ($\overrightarrow{U}_{p_{max}}$) can form an angle $\theta \neq \frac{\pi}{2}$ and (b) the stagnation points undergoing separation because of the bubble's growth as it bursts at the bed surface, thus making for a non-zero velocity.

The stagnation points are the separation points between the arc formed by the dome of the erupting bubble and the bed surface. These points can be defined as the inflection points of the curve formed by them.

Our model (valid for non-spherical bubbles and non-vertical-ascent directions) posits that the particle ejection velocity is the sum of two terms. The first term, $\overrightarrow{U}_{p,b}$, is related to the bubble velocity of the erupting bubble (measured as the displacement of the bubble's center of mass) and the second term, $\overrightarrow{U}_{p,g}$, concerns the bubble growth velocity, defined as

$$U_g = \frac{\partial R_{eq}}{\partial t} = \frac{1}{2}\frac{\partial D_{eq}}{\partial t} \tag{6.2}$$

where D_{eq} is the equivalent diameter, defined as the diameter of one circle with the same bubble area.

The maximum particle velocity vector related to the bubble velocity is assumed

equal to the bubble velocity vector ($\overrightarrow{U}_b$) and perpendicular to the dome contour. The magnitude of $\overrightarrow{U}_{p,b}$ decreases linearly with the angle θ toward the stagnation points, as put forth in Fung and Hamdullahpur (1993). Therefore, the first term of the model can be written as

$$U_{p,b} = \begin{cases} U_b \left(\dfrac{\theta - \theta_{min}}{\theta_b - \theta_{min}} \right) & \text{if} \quad \theta_{min} \leq \theta \leq \theta_b \\ U_b \left(\dfrac{\theta - \theta_{max}}{\theta_b - \theta_{max}} \right) & \text{if} \quad \theta_b \leq \theta \leq \theta_{max} \end{cases} \tag{6.3}$$

where θ_b is the angle formed by the bubble velocity vector and the bed surface and θ_{min} and θ_{max} are the minimum and maximum angles formed by the velocity vectors of the ejected particles, respectively (see figure 6.1). The direction of $\overrightarrow{U}_{p,b}$ is defined by θ.

In bubbling fluidized beds, the bubbles grow as they ascend, until they reach a maximum bubble height (Shen et al., 2004). When the bubble nose reaches the bed surface, a cavity of depth equal to the bubble diameter is formed and the gas through-flow accelerates the particles in the bubble nose while the bubble breaks the bed surface (Glicksman and Yule, 1995). As the bubble rises, the depth of the cavity decreases and the gas flow through the bottom of the bubble is reduced. Then, the velocity of the gas crossing the dome also diminishes. Therefore, particles at the top of the bulge layer (Levy et al., 1982) decelerate due to the gravitational force becomes more important than the drag force, whereas, in the stagnation points the gravitational force direction is practically perpendicular to the movement of such points. In consequence, the erupting bubble expands preferentially in the horizontal direction, i.e. the growth velocity is maximum at the stagnation points.

Levy et al. (1982) obtained implicity similar results about the maximum growth velocity at the stagnation points. They showed that, as the bubble approaches to the bed surface, the distance between the top of the bulge layer and the top of the wake was coming close progressively. Therefore, as bubble's mass center approximates to the bed surface the bubble form became more oblate.

Then, the bubble expands equally in all directions, but in its approach to the bed surface, the expansion is greater in the direction of the bed surface. When $\overrightarrow{U}_b$ has a horizontal component the erupting bubble tends to expand in the same direction. Hence, we assume that the maximum expansion velocities are reached at the stagnation points and U_{pg} decreases linearly until the point of maximum velocity $\overrightarrow{U}_{p,b}$. The direction of the particle ejection velocity due to the bubble growth is perpendicular to

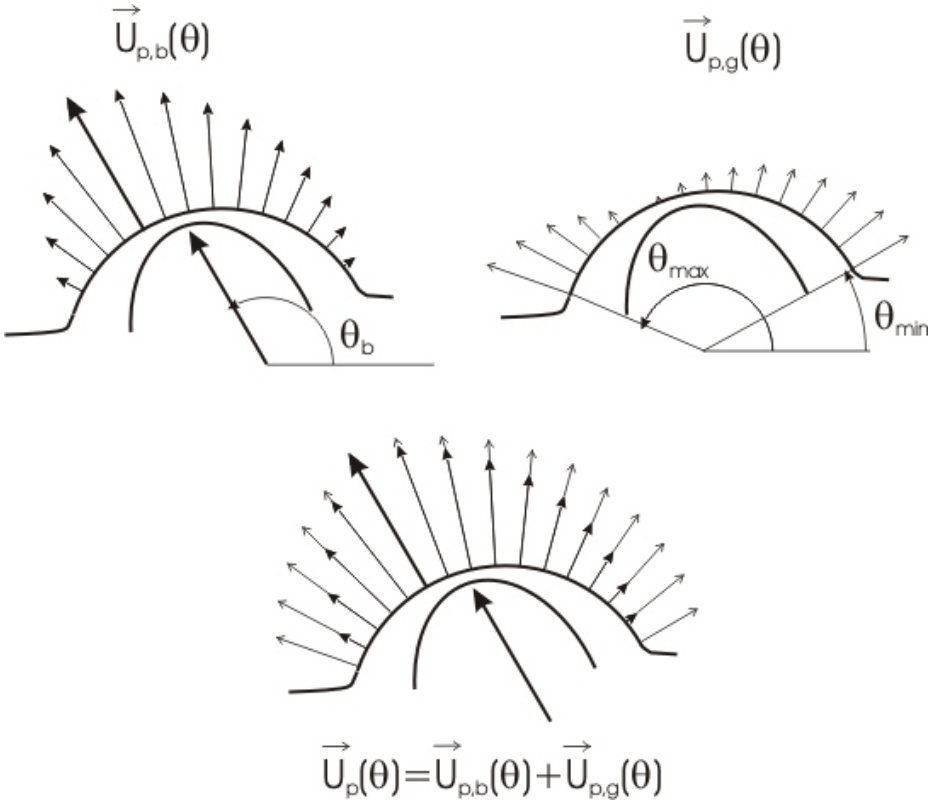

Figure 6.1: Velocity profiles for $U_{p,\,b}\,(\theta)$ and $U_{p,\,g}\,(\theta)$. The sum of both is the particle ejection velocity $U_p\,(\theta)$.

the dome contour, so it is defined by θ; and its magnitude is

$$U_{p,g} = \begin{cases} U_g\ (2 \pm \cos^2\theta_b)\left(1 - \dfrac{\theta - \theta_{min}}{\theta_b - \theta_{min}}\right) & \text{if} \quad \theta_{min} \leq \theta \leq \theta_b \\ U_g\ (2 \mp \cos^2\theta_b)\left(1 - \dfrac{\theta - \theta_{max}}{\theta_b - \theta_{max}}\right) & \text{if} \quad \theta_b \leq \theta \leq \theta_{max} \end{cases} \tag{6.4}$$

where the term $\cos^2(\theta_b)$ is added to the right side of the distribution ($\theta_{min} \leq \theta \leq \theta_b$) when $\theta_b < \frac{\pi}{2}$ and vice versa. The term $2\,U_g$ takes into account that the growth velocity is maximum in the bed surface direction when the bubble erupts, and the term $U_g\ \cos^2\,(\theta_b)$ the effect of the non-vertical ascent of the bubble, that is, $\theta_b \neq \frac{\pi}{2}$. In this case, the bubble expands preferentially in the horizontal component of $\overrightarrow{U}_b$, as can be show in figure 6.6(b), where $\theta_b > \frac{\pi}{2}$ and the velocity on the left stagnation point is higher than the velocity on the right one.

Figure 6.1 shows a sketch of both distributions.

In summary, the particle ejection velocity is the sum of both profiles (equations (6.3) and (6.4)):

$$\overrightarrow{U}_p(\theta) = \overrightarrow{U}_{p,b}(\theta) + \overrightarrow{U}_{p,g}(\theta) \tag{6.5}$$

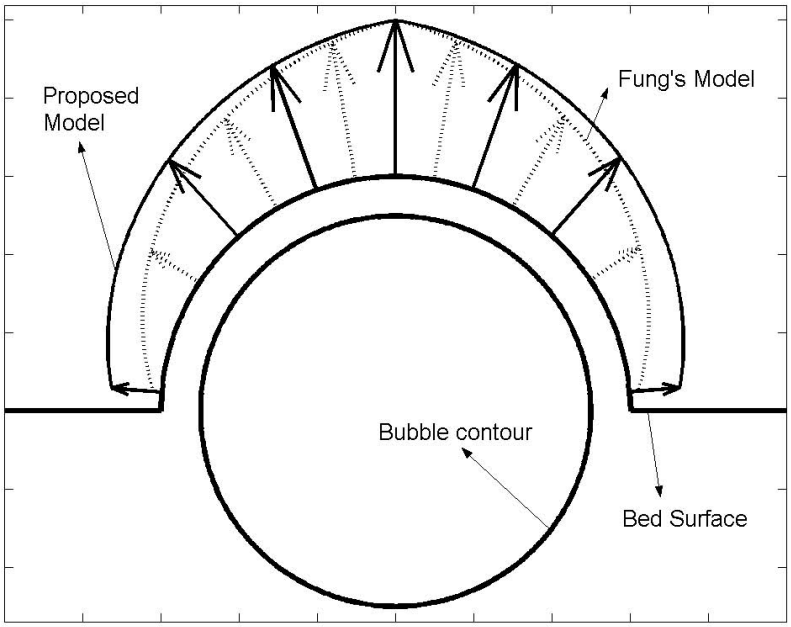

Figure 6.2: Nondimensional velocity profiles for a vertical-ascent circular bubble. Solid lines: Proposed model, dotted lines: Fung's model. $D_b = 5\,cm$, $U_b = 57.5\,cm/s$ and $U_g = 8\,cm/s$.

where the direction of the vector $\overrightarrow{U}_p$ is defined by θ.

It is important to note that the distribution of the particle ejection velocity is not symmetric unless the bubble ascends vertically, that is $\theta_b = \frac{\pi}{2}$ and θ_{min} and θ_{max} are supplementary ($\theta_{min} = \pi - \theta_{max}$). The velocity vectors are always normal to the dome, so the values of θ_{min} and θ_{max} are fixed by the dome's geometry, which depends on bubble shape and its interaction with surrounding bubbles.

In order to compare the proposed model with Fung's model, we can plot both profiles within one particular case of a vertical-ascent circular bubble bursting at the bed surface. The profiles of the nondimensional velocity $U_p^* = U_p/U_{p,max}$ are plotted in figure 6.2, and they show how Fung's model underestimates the horizontal component of the particle ejection velocity (Santana et al., 2005), while the differences in the vertical component are negligible, despite the fact that this only occurs for vertical-ascent circular bubbles. As shown in the experiments carried out by Santana et al. (2005), these differences are more pronounced in non-circular and non-vertical-ascent bubbles. This work corroborates their results.

The bubble velocity and the bubble growth velocity in 2-D fluidized beds have been obtained from the work of Shen et al. (2004), who using an approach similar to the one used by Darton et al. (1977), obtained two expressions: one for bubble diameter

and one for bubble velocity, both of which as a function of the height of the bed

$$D_b = \left(\frac{8\left(2^{\frac{3}{4}}-1\right)}{\lambda}\right)^{\frac{2}{3}} \left[(U-U_{mf})\left(h+\frac{\lambda}{\pi\left(2^{\frac{3}{4}}-1\right)}\frac{A_0}{b}\right)\right]^{\frac{2}{3}} g^{-\frac{1}{3}} \quad (6.6)$$

$$U_b = \phi\sqrt{g\,D_b} \quad (6.7)$$

where A_0 is the area of the distributor divided by the number of orifices, b the bed thickness, h the height measured from the distributor, U_{mf} the minimum fluidization velocity, U the superficial gas velocity and λ and ϕ being constants to be determined experimentally. In their experiments they obtained $\lambda \sim 6.5$ and $\phi = [0.8 - 1.0]$.

On the other hand, the bubble growth velocity, can be obtained as

$$U_g = \frac{1}{2}\frac{\partial D_b}{\partial t} = \frac{1}{2}\frac{\partial h}{\partial t}\frac{\partial D_b}{\partial h} = \frac{1}{2}U_b\frac{\partial D_b}{\partial h} \quad (6.8)$$

and introducing equations (6.6) and (6.7) into equation (6.8), we obtain an expression for the bubble growth velocity as

$$U_g = \frac{1}{3}\left(\frac{8\left(2^{\frac{3}{4}}-1\right)}{\lambda}\right)\phi\,(U-U_{mf}) \quad (6.9)$$

Then, using equations (6.3), (6.4) and (6.5) together with the bubble velocity (equation (6.7)) and the bubble growth velocity (equation (6.9)), the particle velocity profiles along the bubble dome contour of an erupting bubble at the bed surface can be obtained.

6.4 Experiments

The experimental facility is shown in figure 6.3. A cold two-dimensional fluidized bed ($110 \times 60 \times 0.5\ cm$) was constructed. The compressed air was introduced into the plenum, 30 cm high, through two orifices situated on opposite sides of each other, thus ensuring the correct distribution of the flow. The distributor was a perforated plate with 110 holes 1mm in diameter with a 1cm gap between each. Both walls were made of glass, making it possible to see the bed interior and take photographs during the experiments.

The fluidized white-glass spherical particles had diameters ranging from 300 to 400 μm and a density $\rho_p = 2500\frac{kg}{m^3}$. The minimum fluidization velocity was $0.6\,\frac{m}{s}$ in all the experiments and the static bed height was approximately 25 cm. Experiments

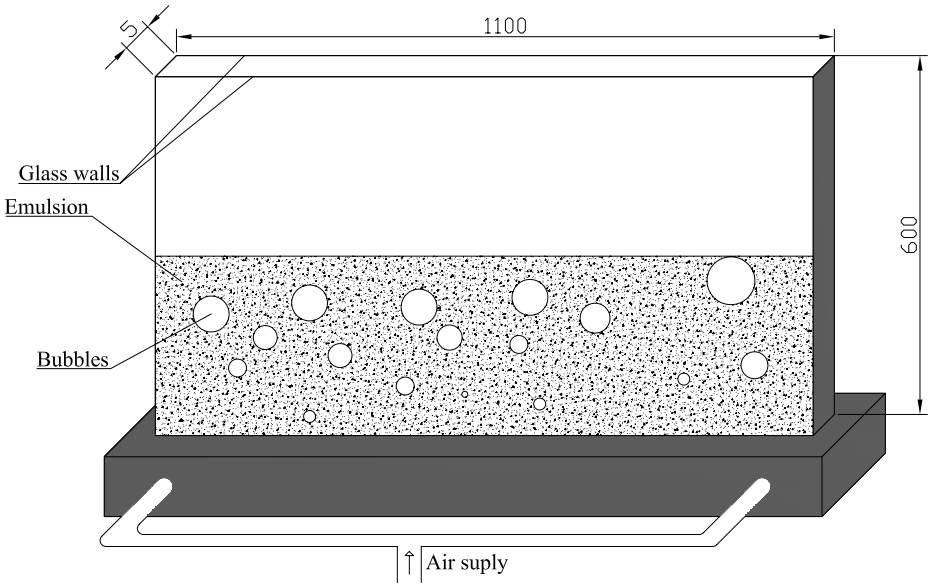

Figure 6.3: Experimental layout. Dimensions in millimeters.

at different superficial gas velocities ($\frac{U}{U_{mf}} = 2, 3$ and 4) were carried out. For all the experimental conditions, the superficial gas velocity was lower than the terminal velocity of the smallest particles, making entrainment negligible.

The 2-D fluidized bed was illuminated with two 600-watts spotlights situated at its front. A black card was placed at the rear, in order to create the maximum contrast between the emulsion phase (since the particles were white) and the bubble phase. The high-speed video camera shot 250 photographs per second with a resolution of 480×512 pixels. The images were analysed following the process developed by Shen et al. (2004). The grey scale image was converted into a binary one using a threshold value, hence the bubble phase and the freeboard were transformed into white color and the emulsion phase into black. Then, the nearest bubble to the freeboard was selected and followed until its eruption at the bed surface. The eruption instant was fixed (see figure 6.4) for the moment in which the interior of the bubble entered into contact with the freeboard and there were no particles (black-colored objects in the photographs) between the freeboard and the bubble (Santana et al., 2005). Figure 6.4 shows how in case (b) the bubble roof does not break the surface of the bed, while in the next photograph (0.004 seconds later) the bubble and the freeboard are joined.

For the last two frames before bubble eruption, the bubble velocity, the bubble area and the bubble area equivalent diameter were measured. With these last two frames, we

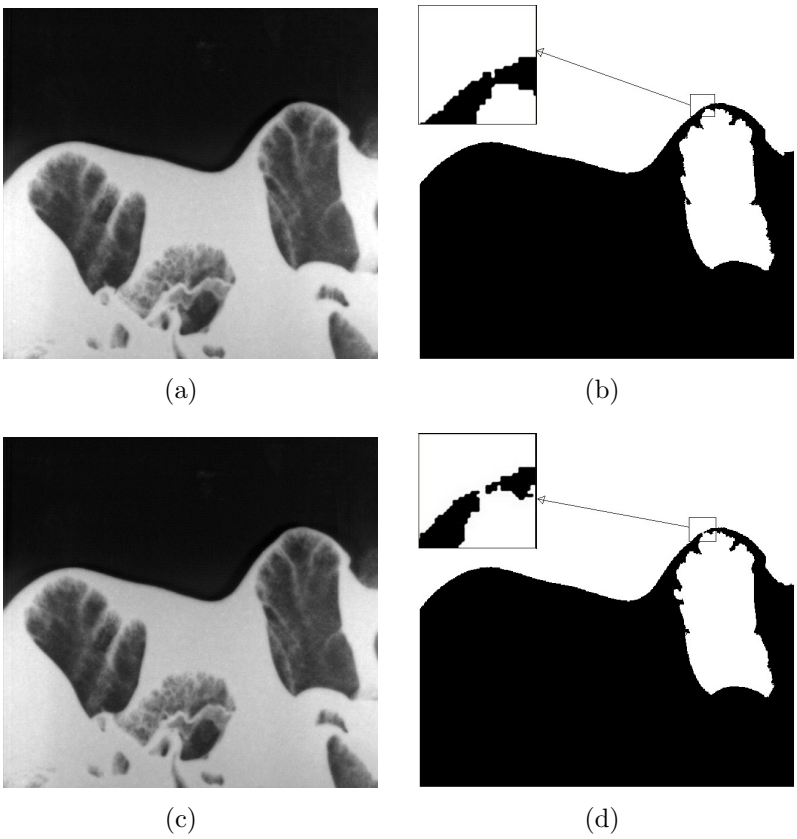

(a) (b)

(c) (d)

Figure 6.4: Determination of the eruption instant: (a) and (c) original photographs (elapsed time: 4 ms), (b) and (d) treated photographs with a zoom in the breaking region.

were able to calculate the velocity profile of the ejected particles, which is perpendicular to the dome contour as Santana et al. (2005) showed in their experiments using a PIV technique. Figure 6.5 explains the process for measuring particle ejection velocity by way of the example of the bursting bubble which appears in figure 6.4. First, we fit an ellipse to the contour of the dome in both photographs using a minimum squared technique. Then, we traced the perpendicular line to the ellipse of the first photograph at each point. These lines intersect the dome contour of the second photograph. The length of the lines between the contours of both domes defines the displacement of the particles ejected into the freeboard. With the time delay between frames (4 ms) the velocity profile of the dome at the instant of eruption is calculated.

6.5 Results and discussion

Different experiments have been carried out varying the superficial gas velocity ($\frac{U}{U_{mf}} = 2\,,3$ and 4). Since a freely bubbling fluidized bed was used, the results obtained show a wide range of erupting bubbles, with different directions of ascent as well as bubble sizes, shapes and velocities. The bubbles followed the path opened by the leading

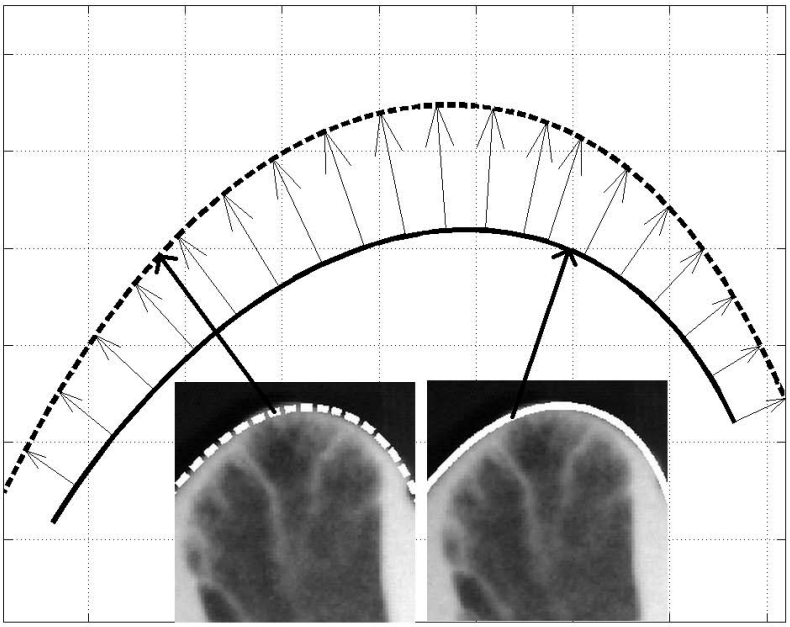

Figure 6.5: Ellipses fitted to the dome contour of the two consecutive frames shown in figure 6.4(a), with a continuos line and figure 6.4(c), with a dotted line. The separation between both ellipses determines the dome velocity profile.

bubbles due to a more favorable pressure gradient. At the same instant, the neighboring bubbles disturb the bed surface when they burst. In all the experiments the height of the bed was below the maximum bubble height (Shen et al., 2004), thus the bubbles were in a state of growth when they erupted.

Figure 6.6 shows the measured dome velocity profiles and bubble velocity vectors for six different cases and table 6.1 charts the results obtained in each experiments. In the first four figures the superficial gas velocity is the same, but the topology of the erupting bubbles is totally different in order to test the validity of the proposed model. For example, the bubble showed in figure 6.6(b) is erupting while another one

CASE	θ_b (deg)	U_b (cm/s)	U_g (cm/s)	D_{eq} (cm)	U/U_{mf}
(a)	101.3	93.7	25.3	11.4	4
(b)	153.4	41.1	6.2	14.7	4
(c)	99.5	111.8	14.4	14.4	4
(d)	90.0	36.8	10.9	16.6	4
(e)	81.9	93.0	15.8	8.8	3
(f)	76.0	47.7	12.7	11.1	2

Table 6.1: Experimental data of the erupting bubbles showed in figure 6.6.

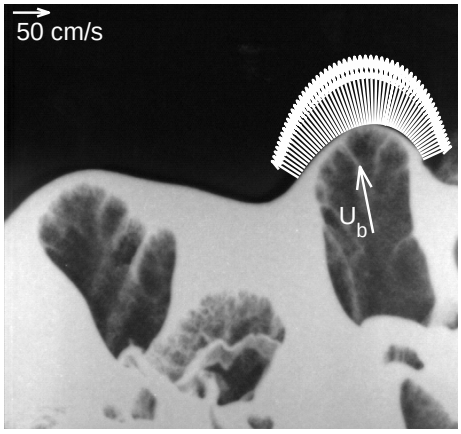

(a) $U/U_{mf} = 4$

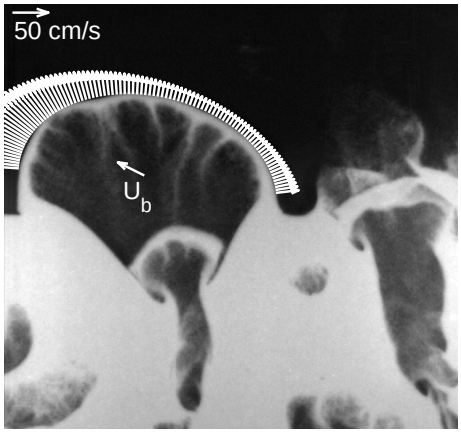

(b) $U/U_{mf} = 4$

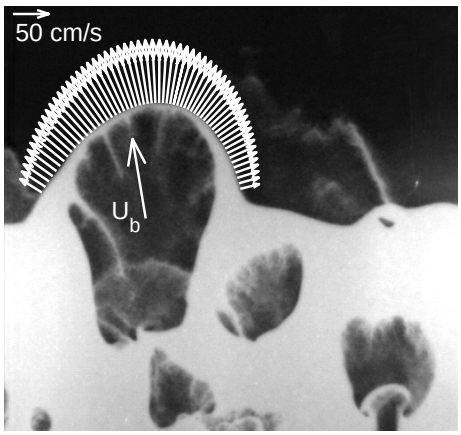

(c) $U/U_{mf} = 4$

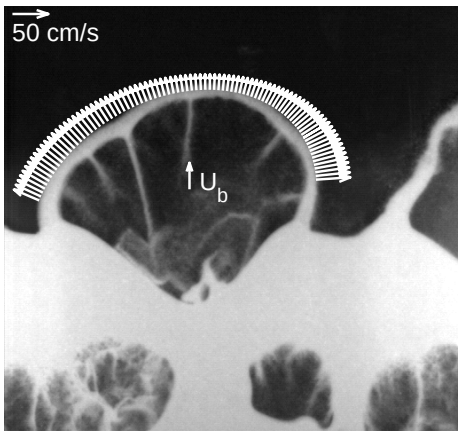

(d) $U/U_{mf} = 4$

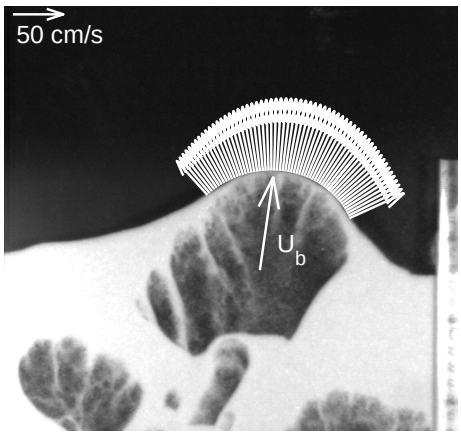

(e) $U/U_{mf} = 3$

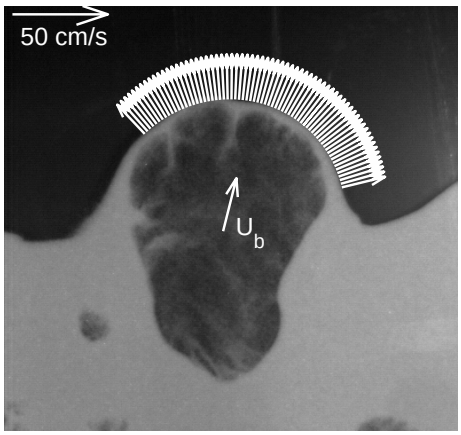

(f) $U/U_{mf} = 2$

Figure 6.6: Some examples of bubble eruption at different superficial gas velocities. Note that the scale of pictures (e) and (f) are different from the others. Figure (d) shows a bubble with a collapsed dome.

is coalescing below. At the same time, a different bubble erupts at the surface close to the right side of the first one. From this fact, we can conclude that the particle velocity is higher in the left direction due to the bubble's inability to expand to the right.

The pictures showed in figures 6.6(a), 6.6(c), 6.6(e) and 6.6(f) are examples of the most typical case, in which the velocity profile has a bell shape with the maximum velocity close to the vertical direction at different superficial gas velocities.

The last case, figure 6.6(d), has an atypical velocity profile because the horizontal component is higher than the vertical one, or they have the same order of magnitude. This fact is representative of bubbles demonstrating the *collapsed dome phenomenon*, which usually appears when the center of gravity of the bubble is above the bed surface at the moment of eruption and almost the entire bubble is outside the bed. The bubble is not ingesting the surrounding air, so its velocity is very low in comparison to a bubble of equal size situated at the same height above the distributor, only under the bed surface. In these circumstances, the bubble erupts, but the particles fall from the dome because the vertical component of the ejection velocity is very small. This type of erupting bubbles is similar to those observed by Solimene et al. (2004) and Levy et al. (1982) for isolated erupting bubbles injected into a 3-D fluidized bed.

In almost all the experiments carried out, always the bubble velocity is higher than the growth velocity. Consequently, the maximum particle ejection velocity is equal to the bubble velocity: $\overrightarrow{U}_{p,max} = \overrightarrow{U}_b$, which is in agreement with the results obtained by Levy et al. (1982) for isolated erupting bubbles.

This maximum particle velocity can be explain by Davidson's model (Davidson, 1961; Davidson and Harrison, 1963). When the bubble nose reaches the bed surface the gas goes through the bubble because the pressure gradient is more favourable. This flow of gas accelerates the particles situated in the nose of the bubble. The gas streamlines in this situation could be similar to the stream lines in the slow bubble case.

For the experiments of figure 6.6, the relative error of the particle ejection velocity, defined as

$$\epsilon(\theta) = \frac{U_{p,\,measured}(\theta) - U_{p,\,model}(\theta)}{U_{p,\,measured}(\theta)} \tag{6.10}$$

was plotted versus θ. The results are shown in figures 6.7(a) and 6.7(b). The first figure compares ϵ for the four experiments with the same superficial gas velocity. The relative error for cases (a) and (c) are under 20 % in almost all the angles. In case (b) the greater error appears at both ends of the profile ($\theta \leq 25\,\text{deg}$ and $\theta \geq 150\,\text{deg}$), though in spite of its unusual nature, the error in most of the velocity vectors is under 40 %. In the *dome collapsed bubble* (case (d)), the error is maximum in $\theta = 90\,\text{deg}$

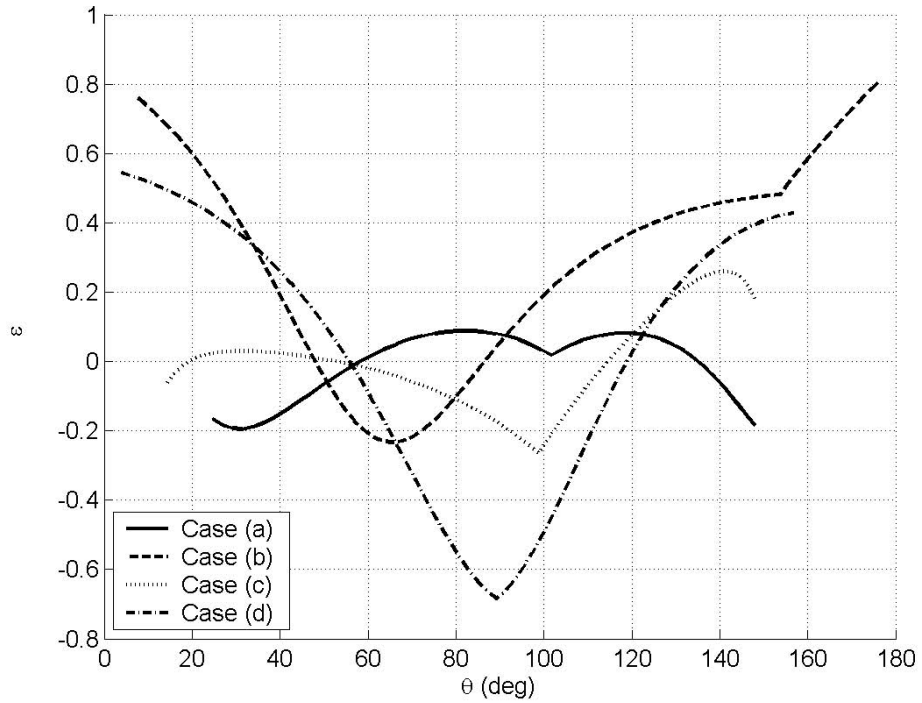

(a)

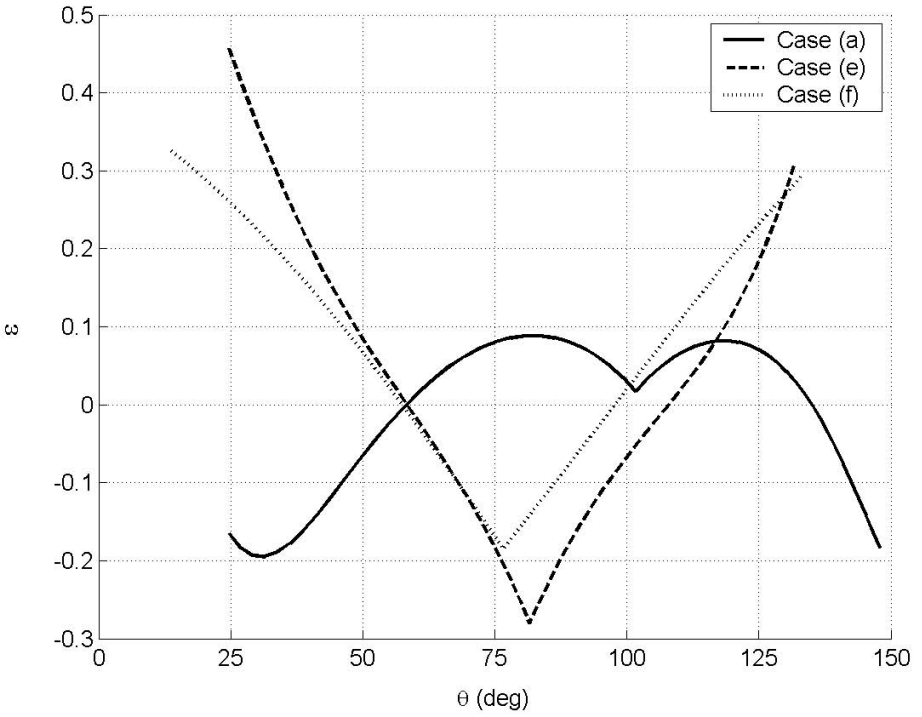

(b)

Figure 6.7: Relative error versus θ for experiments of figure 6.6. (a) comparison of 4 cases with the same superficial gas velocity, and (b) comparison of 3 cases with different superficial gas velocities.

because this is the direction of the bubble velocity, which does not correspond with the maximum particle velocity direction, as the model supposes. In this case, the horizontal component of the particle velocity is higher than the vertical component and the model does not correctly estimate the velocity profile. Figure 6.7(b) proves the validity of the model with different superficial gas velocities within an accuracy of 30 %.

The maximum particle ejection velocity is an important parameter in the determination of solids entrainment from beds. The presented model, supposes that this maximum particle velocity corresponds in magnitude and direction with the bubble velocity.

Figure 6.8(a) compares the direction of the erupting bubble (θ_b) with the angle of the maximum particle velocity vector ($\theta_{p,\,max}$) and figure 6.8(b) compares both velocity magnitudes. The results obtained demonstrate that the model effectively predicts the maximum particle velocity in magnitude and direction, except in isolated cases, like the experiment marked with a square, which corresponds with the picture shown in figure 6.6(d). As noted in the previous paragraph, this *collapsed dome*-type eruption is not properly predicted because almost the entire bubble is outside the bed. It is not ingesting surrounding air and the bubble decelerates. Therefore, in this experiment, the maximum particle velocity appears at the stagnation points and not in the direction of the bubble velocity. When the bubble erupts, the particles rain from the dome because the ejection velocity is very low.

Some other researches (Pemberton and Davidson, 1986; Fung and Hamdullahpur, 1993) have estimated the maximum particle velocity for 3-D fluidized beds as $U_{p\,,max} \sim 2\,U_b$. The experiments shown here demonstrate that this supposition overestimates the particle velocity in 2-D fluidized beds. The images in figure 6.6 show that the thickness of the bubble dome layer when the bubble is erupting at the bed surface is $\delta \gg d_p$. This is typical in 2-D beds (Pemberton and Davidson, 1986), while for 3-D beds $\delta \sim d_p$, since the particle flow from the bubble dome is restricted by wall friction.

To obtain an estimation of the bubble and bubble growth velocities, we use a minimum squared technique (a better fit for the results) to calculate the values of ϕ and λ, in equations (6.7) and (6.9). A value of $\phi = 0.80$ was obtained, which concurs with Shen et al. (2004) and $\lambda = 9.86$, higher that the one obtained by Shen et al. (2004). This may be because equation (6.6) was obtained for bubbles growing inside the bed, far removed from the influence of the bed surface. The experiments show that the bubbles grow more slowly when they approach the bed surface, because they ingest less surrounding air. This supposition allows for a higher value of λ.

The results obtained fitting the variables in equations (6.6) and (6.7) (λ and ϕ) to

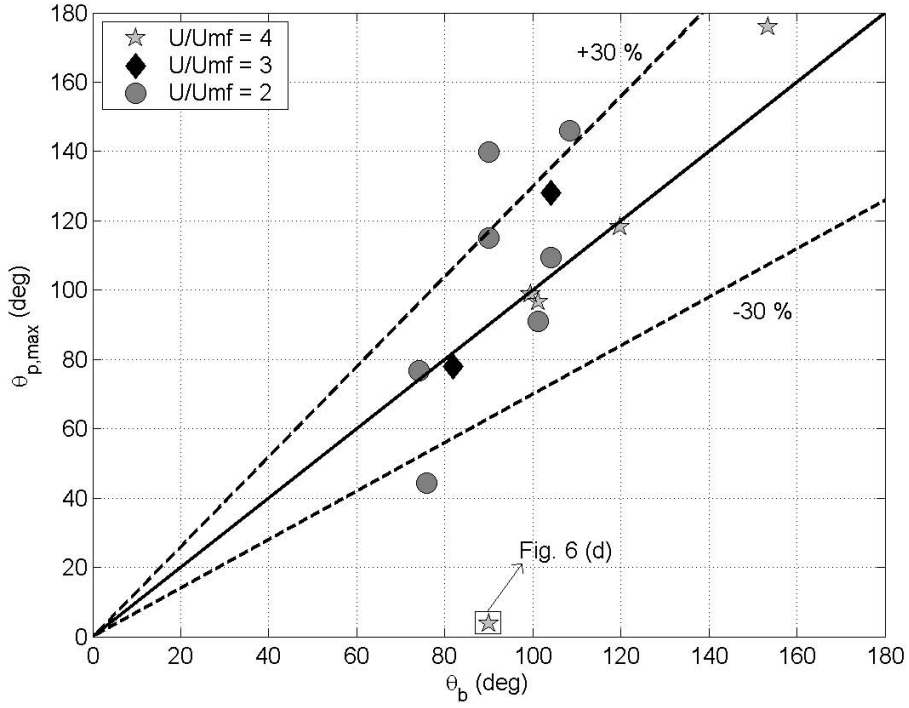

(a)

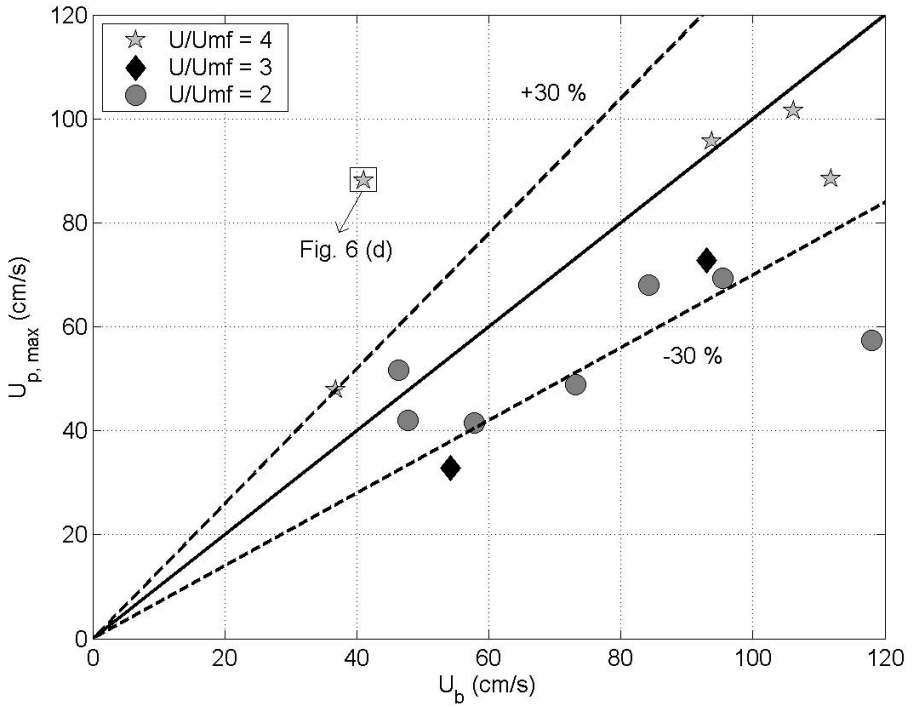

(b)

Figure 6.8: Comparison of bubble direction (a) and bubble velocity (b) with the direction and velocity of the maximum particle ejection velocity vector measured at different superficial gas velocities. Dashed lines indicate ±30 % of error.

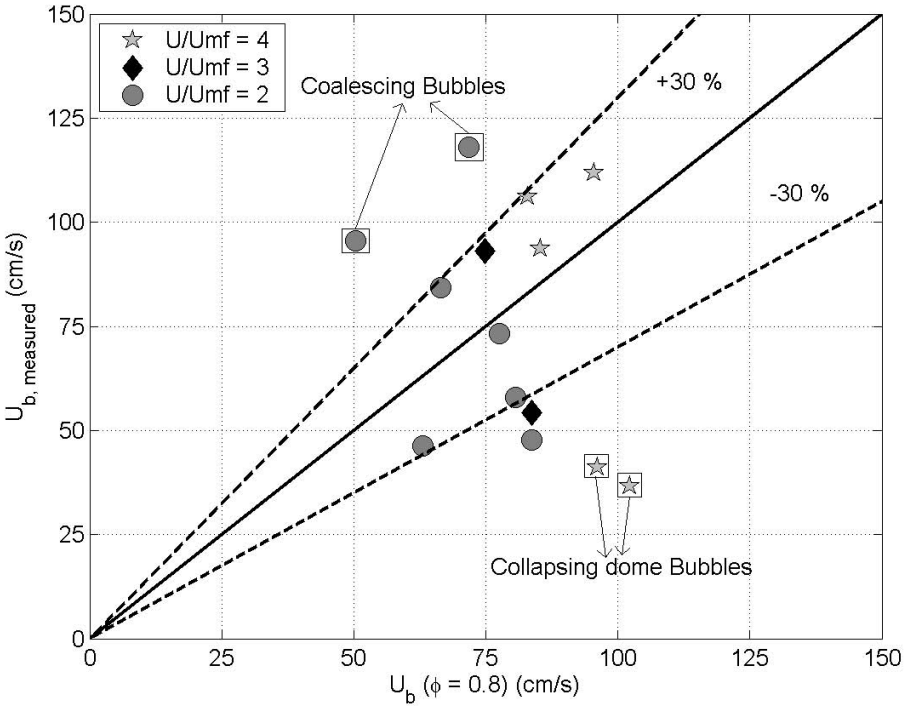

(a)

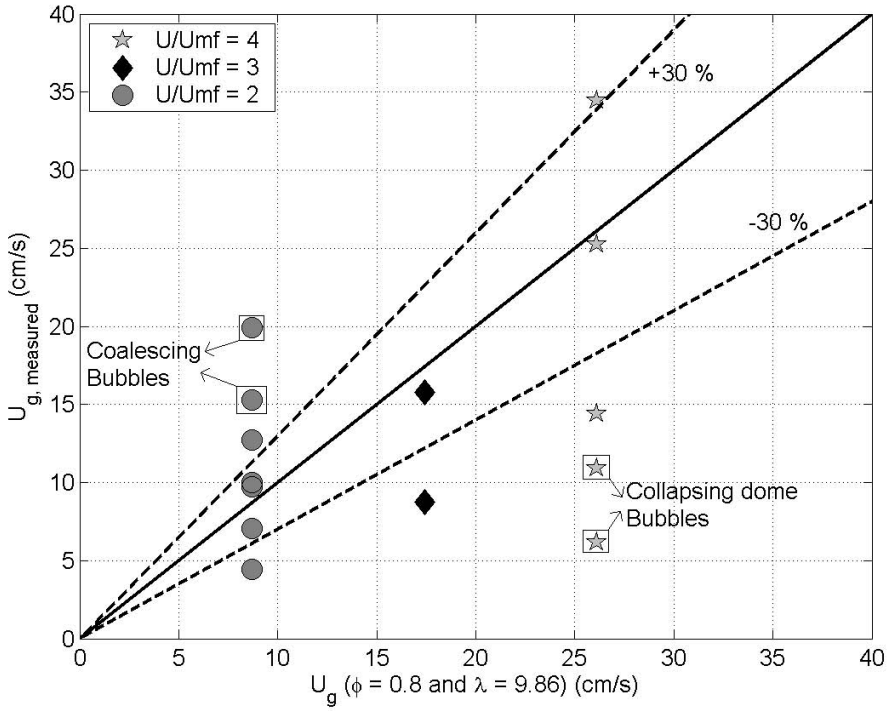

(b)

Figure 6.9: Comparison of the bubble and growth velocities calculated from equations (6.7) and (6.9) with the experimental results ($\phi = 0.80$ and $\lambda = 9.86$). Dashed lines indicate ± 30 % of error.

the experimental data by a minimum square technique are shown in figure 6.9, with two dashed lines indicating a relative error of $\pm 30\,\%$. Four cases that depart from the global tendency of the bubbles (solid line) are marked with a square. Two of these cases ($\frac{U}{U_{mf}} = 2$) differ from the normal behavior because one bubble is coalescing under the leading one as it erupts at the bed surface. Therefore, its velocity is higher than the velocity of the same bubble without coalesce due to the moment transferred by the coalescing bubble. In the other marked experiments, with $\frac{U}{U_{mf}} = 4$, the *collapsed dome phenomenon* causes the bubble velocity and growth velocity to be lower than we expected.

6.6 Conclusions

A new model for particle ejection velocity in 2-D fluidized beds is presented, proposing that the particle velocity is the sum of two terms. One of them is related to the bubble velocity and the other to the growth velocity of the bubble. The main conclusions from the present study can be summarized as follows:

(a) A new model for the velocity profile of the particles ejected from the bubble eruptions in 2-D fluidized beds has been presented. This model, unlike those before it, is valid for all bubble shapes and directions, and not only for vertical-ascent circular bubbles.

(b) The model predicts well the velocity profile and takes into account that the velocity of the stagnation points is non-zero. In bubbles that are influenced by the neighboring bubbles (figure 6.6(b)) the result obtained by the model is also acceptable.

(c) The supposition that the maximum particle velocity is equal to $\overrightarrow{U}_b$ produces a favorable result even if θ_b has a value different from the typical $\theta_b \sim 90\,\text{deg}$ due to the effect of the other bubbles and the effect of coalescence.

(d) The model does not account as well for *collapsed dome* bubbles, because in these cases the bubble is almost entirely outside of the bed and does not ingest air from the surrounding emulsion phase; hence its velocity is lower than the one proposed by the model. As a result, the horizontal component of the particle velocity is higher than the vertical component, and the maximum particle velocity appears at the stagnation points. When this type of bubble bursts at the surface, the particles are not projected to the freeboard; rather, they rain from the dome and return to the bed.

(e) The values of $\overrightarrow{U}_b$ and $\overrightarrow{U}_g$ for bubbles with no coalescence and no collapsed dome can be estimated using equations (6.7) and (6.9) with $\phi = 0.8$ and $\lambda = 9.86$.

6.7 Notation

A_b Area of the erupting bubble (m^2)

A_0 Area of distributor per orifice (m^2)

b Thickness of the bed (m)

D_{eq} Equivalent diameter (m)

d_p Particle diameter (μm)

g Gravity constant (m/s^2)

h Height of bed measured from the distributor (m)

R_{eq} Equivalent radius (m)

t Time (s)

U Superficial gas velocity (m/s)

$\overrightarrow{U}_b$ Bubble velocity vector (m/s)

U_b Magnitude of the bubble velocity vector (m/s)

$\overrightarrow{U}_g$ Bubble growth velocity vector (m/s)

U_g Magnitude of the bubble growth velocity vector (m/s)

U_{mf} Minimum fluidization velocity (m/s)

$\overrightarrow{U}_p$ Particle ejection velocity vector (m/s)

U_p Magnitude of the particle ejection velocity vector (m/s)

U_p^* Nondimensional particle ejection velocity $(-)$

$U_{p,b}$ Particle ejection velocity magnitude related to the bubble velocity (m/s)

$U_{p,g}$ Particle ejection velocity magnitude related to the bubble growth (m/s)

$\overrightarrow{U}_{p,max}$ Maximum particle ejection velocity vector (m/s)

$U_{p,max}$ Magnitude of the maximum particle ejection velocity vector (m/s)

δ Thickness of the bubble dome layer during bubble eruption (m)

ϕ Experimental constant in equations (6.7) and (6.9) $(-)$

ρ_p Particle density (kg/m^3)

λ Experimental constant in equation (6.9) $(-)$

θ Angle formed by the velocity vectors and the bed surface (deg)

θ_b Angle formed by the bubble velocity vector and the bed surface (deg)

θ_{min} Angle formed by the velocity vector at the right stagnation point and the bed surface (deg)

θ_{max} Angle formed by the velocity vector at the left stagnation point and the bed surface (deg)

$\theta_{p,max}$ Angle formed by the maximum particle velocity vector and the bed surface (deg)

ϵ Relative error $(-)$

Bibliography

Darton R.C., LaNauze R.D., Davidson J.F. and Harrison D., 1977. Bubble growth due to coalescence in fluidised beds. *Transactions of the Institute Chemical Engineering*, vol. 55, pp. 274-280

Davidson J.F., 1961. Symposium on fluidisation-Discussion. *Transactions of the Institution of Chemical Engineers*, vol. 39, pp. 230-232

Davidson J.F. and Harrison D., 1963. *Fluidised particles*, Cambridge University Press

Demmich J., 1984. Mechanism of solid entrainment from fluidized beds. *German Chemical Engineering*, vol. 7, pp. 386-394

Do H.T., Grace J.R. and Clift R., 1972. Particle ejection and entrainment from fluidised beds. *Powder Technology*, vol. 6, pp. 195-200

Duursma G.R., Glass D.H. Rix S.J.L. and Yorquez-Ramírez M.I., 2001. PIV investigations of flow structures in the fluidised bed freeboard region. *Powder Technology*, vol. 120, pp. 2-11

Fung A.S. and Hamdullahpur F., 1993. A gas and particle flow model in the freeboard of a fluidized bed based on bubble coalescence. *Powder Technology*, vol. 74, pp. 121-133

Geldart D., 1973. Types of gas fluidization. *Powder Technology*, vol. 7, pp. 285-292

Glicksman L.R. and Yule T., 1995. Prediction of the particle flow conditions in the freeboard of a freely bubbling fluidized bed. *Chemical Engineering Science*, vol. 50, pp. 69-79

Levy E.K., Dille J.C. and Caram H.S., 1982. Single bubble eruptions in gas fluidized beds. *Powder Technology*, vol. 32, pp. 173-178

Pemberton S.T. and Davidson J.F., 1984. Turbulence in the freeboard of a gas-fluidised beds. The significance of ghost bubbles. *Chemical Engineering Science*, vol. 39, pp. 829-840

Pemberton S.T. and Davidson J.F., 1986. Elutriation from fluidized beds - I. Particle ejection from the dense phase into the freeboard. *Chemical Engineering Science*, vol. 41, pp. 243-251

Peters M.H. and Prybylowski D.L., 1983. Particle above the surface of a fluidized bed: Multiparticle Effects. *AIChE Symposium Series*, vol. 79, pp. 83-86.

Santana D., Nauri S., Acosta A., García N. and Macías-Machín A., 2005. Initial particle velocity spatial distribution from 2-D erupting bubbles in fluidized beds. *Powder Technology*, vol. 150, pp. 1-8

Shen L., Johnsson F. and Leckner B., 2004. Digital image analysis of hydrodynamics two-dimensional bubbling fluidized beds. *Chemical Engineering Science*, vol. 59, pp. 2607-2617

Solimene R., Marzocchella A., Ragucci R. and Salatino P., 2004. Flow structures and gas-mixing induced by bubble bursting at the surface of an incipiently gas-fluidized bed. *Industrial & Engineering Chemistry Research*, vol. 43, pp. 5738-5753

Werther J. and Hartge E.U., 2003. Elutriation and Entrainment, in W.C. Yang (ed.), *Handbook of fluidization and fluid-particle systems*, Marcel Dekker Inc., New York, pp. 113-128

Chapter 7

Conclusions

This PhD thesis presents different studies about particle-fluid dynamics, voidage distribution around bubbles and solid ejection in gas-fluidized beds through experimental techniques (PIV and digital image analysis) and numerical analysis (FEM). This chapter tries to present a general overview of the main conclusions. Please, refer to the conclusions given at the end of each chapter for a more detailed description of the achievements.

The combination of both PIV and FEM is a powerfull tool to characterize fluidized bed dynamics. One of the main advantages of this combination is the low computational cost in comparison with traditional CFD approaches. The main difficulty in CFD methods is to obtain the particle velocity field. In contrast, this fact is avoided in this work, as the particle velocity field is measured experimentally using PIV. Then, only the gas momentum and continuity equations need to be solved, reducing notably the computational cost.

The main restriction in the use of PIV is the resolution of the high speed videocamera. In this thesis, a camera of 1.3 Megapixels has been used (except in the results showed in chapter 6, where a camera of 0.25 Megapixels was used), which permits to obtain properly, in a $20 \times 25\,cm$ frame size, the particle velocity with the particle sizes used in this work. The speed of the camera is not a restriction, because a frequency of $250\,fps$ is enough, although higher frequencies could be used (until $1000\,fps$) with the same number of pixels. With the development of higher resolution cameras, a PIV map of the whole bed might be obtained and used to corroborate the particle velocity fields obtained by CFD.

The results of the experimental-numerical approach using the equations proposed by Davidson's model show qualitative agreement with the simplest case of an isolated circular bubble, for the different kinds of bubbles analysed: slow, fast, erupting and interacting bubbles. When non-Darcy effects are included in the computations,

the gas streamlines do not change appreciably for the experimental conditions of this work. Only local differences are observed in the magnitude of the gas velocity for high Reynolds numbers.

Regarding the voidage distribution around bubbles, the experimental results show a narrow region around the bubbles where ϵ decreases rapidly. A correlation is proposed for the voidage distribution in this region. In addition, an increase of 20 % in the throughflow crossing the bubble has been observed due to the increase of the medium permeability with the voidage.

On the other hand, experimental results concerning the solid ejection velocity show that the highest velocities appear when bubble coalescence is involved. In particular, the highest velocities are observed in the wake spike mechanism. In contrast, in the isolated bubble eruption mechanism, the ejection velocity is notably reduced by the rain of particles in the form of stalactites within the bubble.

Finally, a model for the velocity profile of the particles ejected from the bubble dome in isolated erupting bubbles is proposed. The results obtained with this model have been compared with experimental results, showing that it can properly predict the magnitude and direction of the maximum particle ejection velocity and the global velocity profile.

Bibliography

Almendros-Ibáñez J.A., Sobrino C., de Vega M. and Santana D., 2006. A new model for ejected particle velocity from erupting bubbles in 2-D fluidized beds. *Chemical Engineering Science*, vol. 61, pp. 5981-5990

Almendros-Ibáñez J.A., Sobrino C., Sánchez-Delgado S., Santana D., de Vega M. and Ruiz-Rivas U., 2007. Throughflow velocity crossing the dome of erupting bubbles, in X. Bi, F. Berruti, T. Pugsley, (Eds.), *Fluidization XII: New Horizons in Fluidization Engineering*, Engineering Conference International, New York, pp. 169-176

Basu P., 2006. *Combustion and Gasification in Fluidized Beds*. CRC Press

Bear J., 1972. *Dynamics of Fluids in Porous Media*. American Elsevier

Benveniste D.E., Kinrys S. and Qassim R.Y., 1983. Flow past the fluidization bubble: effect of voidage variation, in: D. Kunii D., R. Toei (Eds.), *Fluidization 4*, Engineering Foundation, New York, pp. 9-14

Bird R.B., Stewart W.E. and Lightfoot E.N., 2002. *Transport Phenomena (2nd edition)*. John Wiley & Sons, Inc.

Boerefijn R., Ghadiri M., 1998. High speed video image analysis of flow of fine particles in fluidized bed jets. *Advanced Powder Technology*, vol. 9, pp. 229-243

Böhrnsen J.U., Antes H., Ostendorf M. and Schwedes J., 2004. Silo discharge: measurement and simulation of dynamic behavior in bulk solids, *Chemical Engineering & Technology*, vol. 27, pp. 71-76

Briens C.L., Bergougnou M.A. and Baron T., 1988. Prediction of entrainment from gas-solid fluidized beds, *Powder Technology*, vol. 54, pp. 183-196

Buyevich Y.A., Yates J.G., Cheesman D.J. and Wu K.T., 1995. A model for the distribution of voidage around bubbles in a fluidized bed. *Chemical Engineering Science*, vol. 50, pp. 3155-3162

Chen T.P. and Saxena S.C., 1978. A theory of solids projection from a fluidized bed surface as a first step in the analysis of entrainment processes, in J.F. Davidson and D.L. Keairns (eds.), *Fluidization: Proceedings of the Second Engineering Foundation Conference*, Cambridge University Press, London, pp. 151-156

Choi J.H., Son J.E. and Kim S.D., 1989. Solid entrainment in fluidized bed combustors, *Journal of Chemical Engineering of Japan*, vol. 22, pp. 597-606

Clift R., Grace J.R., Cheung L. and Do T.H., 1972. Gas and solids motion around deformed and interacting bubbles in fluidized beds. *Journal of Fluid Mechanics*, vol. 51, pp. 187-205

Collins R., 1965. An extension of Davidson's theory of bubbles in fluidized beds. *Chemical Engineering Science*, vol. 20, pp. 747-755

Collins R., 1989. A model for the effects of the voidage distribution around a fluidization bubble. *Chemical Engineering Science*, vol. 44, pp. 1481-1487

Croxford A.J., 2006. Investigation of dynamics and control of fluidised beds using pressure measurements. PhD thesis, University of Bristol

Darton R.C., LaNauze R.D., Davidson J.F. and Harrison D., 1977. Bubble growth due to coalescence in fluidised beds. *Transactions of the Institute Chemical Engineering*, vol. 55, pp. 274-280

Davidson J.F., 1961. Symposium on fluidisation-Discussion. *Transactions of the Institution of Chemical Engineers*, vol. 39, pp. 230-232

Davidson J.F. and Harrison D., 1963. *Fluidised particles*. Cambridge University Press

Davidson J.F., Harrison D. and Guedes de Carvalho J.R.F., 1977. On the liquidlike behavior of fluidized beds. *Annual Review of Fluid Mechanics*, vol. 9, pp. 55-86

Demmich J., 1984. Mechanism of solid entrainment from fluidized beds. *German Chemical Engineering*, vol. 7, pp. 386-394

Devi L., Ptasinski K.J. and Janssen F.J.J.G., 2003 A review of the primary measures for tar elimination in biomass gasification processes. *Biomass and Bioenergy*, vol. 24, pp. 125-140

Do H.T., Grace J.R. and Clift R., 1972. Particle ejection and entrainment from fluidised beds, *Powder Technology*, vol. 6, pp. 195-200

Duru P., Guazzelli E., 2002. Experimental investigation on the secondary instability of liquid-fluidized beds and the formation of bubbles. *Journal of Fluid Mechanics*, vol. 470, pp. 359-382

Duursma G.R., Glass D.H. Rix S.J.L. and Yorquez-Ramírez M.I., 2001. PIV investigations of flow structures in the fluidised bed freeboard region. *Powder Technology*, vol. 120, pp. 2-11

Dybbs A. and Edwards R.V., 1984. A new look at porous media fluid mechanics - Darcy to turbulence, in: J. Bear, M.Y. Corapcioglu, *Fundamentals of Transport Phenomena in Porous Media*, Dordrecht: Martinus Nijhoff Publishers, pp. 199-254

Ergun S., 1952. Fluid flow through packed columns. *Chemical Engineering Progress*, vol. 48, pp. 89-94

Foscolo P.U., Gibilaro L.G. and Waldram S.P., 1983. A unified model for particulate expansion of fluidised beds and flow in fixed porous media. *Chemical Engineering Science*, vol. 38, pp. 1251-1260

Foscolo P.U. and Gibilaro L.G., 1984. A fully predictive criterion for the transition between particulate and aggregative fluidization. *Chemical Engineering Science*, vol. 39, pp. 1667-1675

Foscolo P.U., Gibilaro L.G., Di Felice R. and Waldram S.P., 1985. The effect of interparticle forces on the stability of fluidized beds. *Chemical Engineering Science*, vol. 40, pp. 2379-2381

Foscolo P.U. and Gibilaro L.G., 1987. Fluid dynamic stability of fluidized suspensions. The particle bed model. *Chemical Engineering Science*, vol. 42, pp. 1489-1500

Fung A.S. and Hamdullahpur F., 1993. A gas and particle flow model in the freeboard of a fluidized bed based on bubble coalescence. *Powder Technology*, vol. 74, pp. 121-133

Geldart D., 1967. The fluidised bed as a chemical reactor: A critical review of the first 25 years. *Chemistry and Industry*, vol. 35, pp. 1474-1481

Geldart D., 1968. Gas-solid reactions in industrial fluidised beds. *Chemistry and Industry*, vol. 2, pp. 41-47

Geldart D., 1969. Physical processing in gas fluidised beds. *Chemistry and Industry*, vol. 11, pp. 311-316

Geldart D., 1973. Types of gas fluidization, *Powder Technology*, vol. 7, pp. 285-292

Geldart D., 1986. Single particles, fixed and quiescent beds, in: D. Geldart (Ed.), *Gas Fluidization Technology*, John Wiley & Sons, pp. 11-32

George S.E. and Grace J.R., 1978. Entrainment of particles from agregative fluidized beds, *AIChE Symposium Series*, vol. 74, pp. 67-74

Gera D. and Gautam M., 1994. Variation of throughflow velocity in a 2-D rising bubble. *Powder Technology*, vol. 79, pp. 257-263

Gera D. and Gautam M., 1994. Effect of voidage variation and bubble aspect ratio on throughflow in 2-D elliptical bubbles. *Powder Technology*, vol. 79, pp. 159-165

Gibilaro L.G., Di Felice R., Waldran S.P. and Foscolo P.U., 1985. Generalized friction factor and drag coefficient correlations for fluid-particle interactions. *Chemical Engineering Science*, vol. 40, pp. 1817-1823.

Gibilaro L.G., 2001. *Fluidization-dynamics*. Butterworth-Heinemann

Gidaspow D., 1994. *Multiphase Flow and Fluidization*. Academic Pres Inc.

Glicksman L.R. and Yule T., 1986. Gas throughflow in a bubbling fluidized beds, in K. Ostergaard, A. Sorensen (Eds.) *Fluidization V: Proceedings of the Engineering Foundation Conference*, Amer. Inst. of Chemical Engineers, Elsinore (Denmark), pp. 103-110

Glicksman L.R. and Yule T., 1995. Prediction of the particle flow conditions in the freeboard of a freely bubbling fluidized bed. *Chemical Engineering Science*, vol. 50, pp. 69-79

Goldschmidt M.J.V., Link J.M., Mellena S. and Kuipers J.A.M., 2003. Digital image analysis measurements of bed expansion and segregation dynamics in dense gas-fluidised beds. *Powder Technology*, vol. 138, pp. 135-159

Gonzales-Barron U., Butler f., 2006. A comparison of seven thresholding techniques with the k-means clustering algorithm for measurement of bread-crumb features by digital image analysis. *Journal of Food Engineering*, vol. 74, pp. 268-278

Grace J.R., 1986. Contacting modes and behaviour classification of gas-solid and other two-phase suspensions. *The Canadian Journal of Chemical Engineering*, vol. 64, pp. 353-363

Grace J.R. and Clift R., 1974. On the two-phase theory of fluidization. *Chemical Engineering Science*, vol. 29, pp. 327-334

Grace J.R. and Harrison D., 1969. The behaviour of freely bubbling fluidised beds. *Chemical Engineering Science*, vol. 24, pp. 497-508

Halow J.S. and Nicoletti P., 1992. Observations of fluidized-bed coalescence using capacitance imaging. *Powder Technology*, vol. 69, pp. 255-277

Hatano H. and Ishida M., 1981. The entrainment of solid particles from a gas-solid fluidized bed, *Journal of Chemical Engineering of Japan*, vol. 14, pp. 306-311

Hatano H. and Ishida M., 1982. Study on the cloud radius and interphase mass transfer coefficient for a gas-solid fluidized bed. *Kagaku Kogaku Ronbunshu*, vol. 10, pp. 184-191

Jackson J.R., 1963a. The mechanics of fluidised beds: Part I: The stability of the state of uniform fluidisation. *Transactions of the Institution of Chemical Engineers*, vol. 41, pp. 13-21

Jackson J.R., 1963b. The mechanics of fluidised beds: Part II: The motion of fully developed bubbles. *Transactions of the Institution of Chemical Engineers*, vol. 41, pp. 22-28

Jackson J.R., 2000. *The dynamic of fluidized particles*. Cambridge University Press

Johnsson F., Andersson S. and Leckner B., 1991. Expansion of a freely bubbling fluidized bed. *Powder Technology*, vol. 68, pp. 117-123

Johnsson F., Zijerveld R.C., Schouten J.C., van den Bleek C.M. and Leckner B., 2000. Characterization of fuidization regimes by time-series analysis of pressure fluctuations. *International Journal of Multiphase Flow*, vol. 26, pp. 663-715

Koornneef J., Junginger M. and Faaij A., 2007. Developement of fluidized bed combustion - An overview of trends, performance and cost. *Progress in Energy and Combustion Science*, vol. 33, pp. 19-55

Kunii D. and Levenspiel O., 1969. *Fluidization Engineering*. John Wiley & Sons

Kunii D. and Levenspiel O., 1990. Entrainment of solids from fluidized beds. I. Hold-up of solids in the freeboard. II. Operation of fast fluidized beds, *Powder Technology*, vol. 61, pp. 193-206

Kunii D. and Levenspiel O., 1991. *Fluidization Engineering (2nd edition)*. Butterworth-Heinemann

Leckner B., 2005. Book review. *Energy*, vol. 30, pp. 97-99

Levenspiel O., 2002. Modeling in chemical engineering, *Chemical Engineering Science*, vol. 57, pp. 4691-4696

Levenspiel O., 2008. Difficulties in trying to model and scale-up the bubbling fluidized bed (BFB) reactor, *Industrial & Engineering Chemistry Research*, vol. 47, pp. 273-277

Levy E.K., Dille J.C. and Caram H.S., 1982. Single bubble eruptions in gas fluidized beds, *Powder Technology*, vol. 32, pp. 173-178

Levy E.K., Caram H.S., Dille J.C. and Edelstein S., 1983. Mechanims for solid ejection from gas-fluidized beds, *AIChE Journal*, vol. 29, pp. 383-388

Levy E.K., Chen H.K., Radcliff R. and Caram H.S., 1988. Analysis of gas flow through erupting bubbles in a gas-fluidized bed. *Powder Technology*, vol. 54, pp. 45-57

Lignola P.G., Donsi G. and Massimilla L., 1983. Mass spectrometric measurements of gas composition profiles associated with bubbles in a two dimensional bed. *AIChE Symposium Series*, vol. 79, pp. 19-25

Littman H. and Homolka G.A.J., 1973. The pressure field around a two-dimensinal gas bubble in a fluidized bed. *Chemical Engineering Science*, vol. 28, pp. 2231-2243

Liu S. and Masliyah J.B., 1996. Single fluid flow in porous media. *Chemical Engineering Communications*, vol. 150, pp. 653-732

Lockett M.J. and Harrison D., 1967. The distribution of voidage fraction near bubbles rising in gas-fluidized beds, in: A.A.H. Drinkenburg (Ed.), *Int. Symp. on Fluidization*, Netherlands University Press, Amsterdam, pp. 257-267

Lueptow R.M., Akonur A. and Shinbrot T.,2000. PIV for granular flows, *Experiments in Fluids*, vol. 28, pp. 183-186

Massimilla L. and Westwater J.W., 1960. Photographic study of solid-gas fluidization. *AIChE Journal*, vol. 6, pp. 134-138

Molerus O., 1982. Interpretation of Geldart's type A, B, C and D powders by taking into account interparticle cohesion forces. *Powder Technology*, vol. 33, pp. 81-87

Müller C.R., Davidson J.F., Dennis J.S., Fennell P.S., Gladden L.F., Hayhurst A.N., Mantle M.D., Rees A.C. and Sederman A.J., 2006. Real-time measurement of bubbling phenomena in a three-dimensional gas-fluidized bed using ultrafast magnetic resonance imaging. *Physical Review Letters*, vol. 96, article number 154504

Müller C.R., Davidson J.F., Dennis J.S., Fennell P.S., Gladden L.F., Hayhurst A.N., Mantle M.D., Rees A.C. and Sederman A.J., 2007a. Rise velocities of bubbles and slugs in gas-fluidised beds: Ultra-fast magnetic resonance imaging. *Chemical Engineering Science*, vol. 62, pp. 82-93

Müller C.R., Davidson J.F., Dennis J.S. and Hayhurst A.L., 2007b. A study of the motion and eruption of a bubble at the surface of a two-dimensional fluidized bed using particle image velocimetry (PIV), *Industrial & Engineering Chemistry Research*, vol. 46, pp. 1642-1652

Murray J.D., 1965a. On the mathematics of fluidization. Part 1. Fundamental equations and wave propagation. *Journal of Fluid Mechanics*, vol. 21, pp. 465-493

Murray J.D., 1965b. On the mathematics of fluidization. Part 2. Steady motion of fully developed bubbles. *Journal of Fluid Mechanics*, vol. 22, pp. 57-80

Nguyen X.T., Leung L.S. and Weiland R.H., 1973. On void fractions around a bubble in a two dimensional fluidized bed, in: H. Angelino, J.P. Couderc, H. Gilbert, C. Lagarie (Eds.), *Proc. Int. Cong. Fluidization and its Applications*, Toulouse, pp. 230-239

Oka S.N., 2004. *Fluidized Bed Combustion*. Marcel Dekker Inc.

Ostendorf M. and Schewedes J., 2005. Application of particles image velocimetry for velocity measurements during silo discharge, *Powder Technology*, vol. 158, pp. 69-75

Otsu N., 1979. A threshold selection method from gray-level histograms, *IEEE Transactions on Systems Man and Cybernetics*, vol. 9, pp. 62-66

Pallarès D. and Johnsson F., 2006. A novel technique for particle tracking in cold 2-dimensional fluidized beds-simulating fuel dispersion. *Chemical Engineering Science*, vol. 61, pp. 2710-2720

Pemberton S.T. and Davidson J.F., 1984. Turbulence in the freeboard of a gas-fluidised beds. The significance of ghost bubbles. *Chemical Engineering Science*, vol. 39, pp. 829-840

Pemberton S.T. and Davidson J.F., 1986. Elutriation from fluidized beds-I. Particle ejection from the dense phase into the freeboard, *Chemical Engineering Science*, vol. 41, pp. 243-251

Peters M.H. and Prybylowski D.L., 1983. Particle above the surface of a fluidized bed: Multiparticle Effects. *AIChE Symposium Series*, vol. 79, pp. 83-86.

Poletto M., Bai R., Joseph D.D., 1995. Propagation of voidage waves in a two-dimensional liquid-fluidized bed. *International Journal of Multiphase Flow*, vol. 21, pp. 223-239

Qassim R.Y., Kinrys S. and Benveniste D.E., 1989. Effect of voidage variation on flow past a fluidisation bubble. *Chemical Engineering Science*, vol. 44, pp. 1307-1313

Ramón y Cajal S., 1902. *Reglas y Consejos Sobre la Investigación Científica*. Reprinted by CSIC in 2005

Ramos Caicedo G., García Ruiz M., Prieto Marqués J.J. and Guadiola Soler J., 2002. Minimum fluidization velocities for gas-solid 2d beds. *Chemical Engineering and Processing*, vol. 41, pp. 761-764

Raso G.G., Volpicelli G. and Maitz C., 1965. Sul movimento do bolle di gas in letti di particelle fluidizzati in colonne rettangolari. *Quaderni dell'ingegnere chimico italiano*, vol. 1, pp. 157-167

Rees A.C., Davidson J.F., Dennis J.S., Fennell P. S., Gladden L.F., Hayhurst A.N., MantleM.D., Muller C.R. and Sederman A.J., 2006. The nature of the flow just above the perforated plate distributor of a gas-fluidised bed, as imaged using magnetic resonance. *Chemical Engineering Science*, vol. 61, pp. 6002-6015

Ross D., Noda R., Horio M., Kosminski A., Ashman P. and Mullinger P., 2007. Axial gas profiles in a bubbling fluidised bed biomass gasifier, *Fuel*, vol. 86, pp. 1417-1429

Rowe P.N., Partridge B.A. and Lyall E., 1964. Cloud formation around bubbles in gas fluidized beds. *Chemical Engineering Science*, vol. 19, pp. 973-985

Rowe P.N. and Partridge B.A., 1965. An x-ray study of bubbles in fluidised beds. *Transactions of the Institution of Chemical Engineers*, vol. 43, pp. 157-175

Russ J.C., 1994. *The Image Procesing Handbook*, 2nd edition. CRC Press

Santana D., Rodríguez J.M. and Macías-Machín A., 1999. Modelling fluidized bed elutriation of fine particles, *Powder Technology*, vol. 106, pp. 110-118

Santana D., Nauri S., Acosta A., García N. and Macías-Machín A., 2005. Initial particle velocity spatial distribution from 2-D erupting bubbles in fluidized beds. *Powder Technology*, vol. 150, pp. 1-8

Santana D., Rodríguez-Rodríguez J., Almendros-Ibáñez J.A. and Martínez-Bazán C., 2006. Characteristic lengths and maximum entropy estimation from probe signals in the ellipsoidal bubble regime. *International Journal of Multiphase Flow*, vol. 32, pp. 1123-1139

Saxena S.C. and Mathur A., 1984. On the origin of solids projected from the surface of a gas-fluidized bed, *Chemical Engineering Science*, vol. 39, pp. 917-918

Shen L., Johnsson F. and Leckner B., 2004. Digital image analysis of hydrodynamics two-dimensional bubbling fluidized beds. *Chemical Engineering Science*, vol. 59, pp. 2607-2617

Shichi R., Mori S. and Muchi I., 1968. Interaction between two bubbles in gaseous fluidization. *Kagaku Kogaku*, vol. 32, pp. 343-348

Slominski C., Niedostatkiewicz M. and Tejchman J., 2007. Application of particle image velocimetry (PIV) for deformation measurement during granular flow, , *Powder Technology*, vol. 173, pp. 1-18

Smolders K. and Baeyens J., 1997. Elutriation of fines from gas fluidized beds: mechanims of elutriation and effect of freeboard geometry, *Powder Technology*, vol. 92, pp. 35-46

Solimene R., Marzocchella A., Ragucci R. and Salatino P., 2004. Flow structures and gas-mixing induced by bubble bursting at the surface of an incipiently gas-fluidized bed. *Industrial & Engineering Chemistry Research*, vol. 43, pp. 5738-5753

Stewart P.S.B., 1968a. Isolated bubbles in fluidized beds - theory and experiment. *Transactions of the Institution of Chemical Engineers*, vol. 46, pp. 60-66

Stewart P.S.B., 1968b. Prediction of voidage fraction near bubbles in fluidised beds. *Chemical Engineering Science*, vol. 23, pp. 396-397

Sveen J.P., http://www.math.uio.no/∼jks/matpiv (Last modified in August, 2004. Accesed in 2008)

Toomey R.D. and Johnstone H.F., 1952. Gaseous fluidization of solid particles. *Chemical Engineering Progress*, vol. 48, pp. 220-226

Trisakti B., Oshitani J. and Tanaka Z., 2001. Circulating particle flow and air bubble behavior at various superficial gas velocities in two-dimensional gas-solid fluidized beds. *Advanced Powder Technology*, vol. 12, pp. 507-519

Valenzuela J.A. and Glicksman L.R., 1985. Gas flow distribution in a bubbling fluidized bed. *Powder Technology*, vol. 44, pp. 103-113

van Dyke M., 1982. *An Album of Fluid Motion (8th edition)*. The Parabolic Press, p. 43

van Wachem B.G.M. and Almstedt A.E., 2003. Methods for multiphase computational fluid dynamics. *Chemical Engineering Journal*, vol. 96, pp. 81-98

Villa Briongos J. and Guardiola J., 2005. New methodology for scaling hydodynamic data from a 2D-fluidized bed. *Chemical Engineering Science*, vol. 60, pp. 5151-5163

Wen C.Y. and Chen L.H., 1982. Fluidized bed freeboard phenomena: entrainment and elutriation, *AIChE Journal*, vol. 28, pp. 117-128

Werther J. and Hartge E.U., 2003. Elutriation and Entrainment, in W.C. Yang (ed.), *Handbook of fluidization and fluid-particle systems*, Marcel Dekker Inc., New York, pp. 113-128

Yates J.G. and Rowe P.N., 1977. A model for chemical reaction in the freeboard region above a fluidised bed, *Transactions of the Institution of Chemical Engineers*, vol. 55, pp. 137-142

Yates J.G., Cheesman D.J. and Sergeev Y.A., 1994. Experimental observations of voidage distribution around bubbles in a fluidized bed. *Chemical Engineering Science*, vol. 49, pp. 1885-1895

Zenz F.A. and Weil N.A., 1958. A theoretical-empirical approach to the mechanism of particle entrainment from fluidized beds, *AIChE Journal*, vol. 4, pp. 472-479

Zenz Z. and Grigg G., 2006. A Criterion for Non-Darcy Flow in Porous Media. *Transport in Porous Media*, vol. 63, pp. 57-69